

Micro Shock Wave

— A Study of Supersonic Compressible Flow with Low Reynolds Number by Application of Ultra Short Laser Pulse and Interferometry

Von der Fakultät für Mathematik und Naturwissenschaften
der Carl von Ossietzky Universität Oldenburg zur Erlangung
des Grades und Titels eines

Dr. rer. nat.

angenommene Dissertation

von Herrn Yun Kai

geboren am 04. Juli 1986 in Guangxi

Gutachter: Prof. Dr. Ulrich Teubner

Weiterer Gutachter: Prof. Dr. Joachim Peinke

Tag der Disputation: 17. April 2018

Abstract

This thesis is written in the scope of the DFG-project: micro shock waves. This is a study of supersonic compressible flow with low Reynolds numbers by application of ultra short laser pulse and interferometry. The micro shock waves have demonstrated different fluid mechanical characteristics as macroscopic shock waves, micro shock waves thus have emerge as a new area in the physics of fluid since the beginning of the 21st century. However, there is very limited amount of works in this field of study due to technical limitations. Furthermore, the propagation mechanism of the micro shock flow system (including shock wave, boundary layer, contact surface and expansion fan) wasn't clear at all till now. Therefore, the present work is a report on substantial progress in shock wave physics.

Actually the shock wave experiments in truly sub-mm scale have only been performed by two groups world wide: the Brouillette group in Sherbrooke, Canada and our group in Emden, Germany. The group of Brouillette uses completely different technique to generate and detect the micro shock waves than our technique. The detailed difference will be discussed in this thesis. Moreover, downsizing of macroscopic objects to micro/nano scales is a trend in physics nowadays, and this thesis contributes to this trend.

The works that have been done in the frame of this project are listed as follows:

1. Investigations of shock-cavitation interaction in miniature glass tubes in water.
2. Modifications/improvements of the laser differential interferometer LDI (the main diagnostic).
3. Development of a novel shock generation method using a laser plasma as driver.
4. Development of a novel shock generation method involving a high-speed magnetic valve.
5. Correction of the Rankine-Hugoniot relation for micro shock waves.
6. Confrontation of the existing theories on shock flow i.e. 'leaky piston' model with experimental results.

The experimental investigations applying the two novel methods to generate micro shock waves form the major parts of the thesis:

(A) LIMS - Laser-plasma Induced Micro Shocks: A femtosecond laser pulse is focused onto an aluminum film as a target to generate optical breakdown. Due to the sudden appearance of this extreme non-equilibrium on the target, a shock wave is emitted from the breakdown spot. The shock wave is initially driven by the expanding high pressure

plasma (up to 10 Mbar) which serves as a quasi piston, until the plasma recombines and the hot mixture of Al and air gets cold.

The work presents experimental investigations on direct micro shocks generation in a micro capillary/tube for the first time (the cookie-cutter like shock tubes in previous reports are not ‘direct’ shock generation). The experiments are performed under different conditions and in different capillaries with 50 μm to 300 μm hydraulic diameter. Different from previous shock wave investigations involving pressure transducers or Schlieren optics, the present work applies the LDI for density and velocity measurements. The 1D laser-plasma simulation MULTIfs is applied to numerically investigate the shock wave onset process. Far-field propagation of the micro shock in the capillary is analyzed by the computation of 2D compressible Navier-Stokes equations. The MULTIfs simulation and Navier-Stokes computation agree with the experimental results. Furthermore, the experimental values are compared with the theoretical values calculated by using the classical Rankine-Hugoniot relation (density jump as a function of Mach number, under ideal conditions) as well as its corrected version. The corrected Rankine-Hugoniot relation proposed in this thesis takes the diffusive transport phenomena (due to wall friction and wall heat conduction) into consideration.

(B) Shock tube with high-speed magnetic valve: Due to the lack of a well understanding of the propagation mechanism of the micro shock flow system, the current work concentrates on measuring micro shock flows with special attention paid to the contact surface. A novel setup involving a glass capillary (with 200 μm or 700 μm hydraulic diameter D) and a high-speed magnetic valve is applied to generate a shock wave with a maximum initial Mach number of 1.6. The laser differential interferometer is applied to perform measurements of the micro shock flow’s trajectory, velocity and density. Schlieren optics is also applied for control experiments. The current work presents the first micro scale measurements of the shock-contact distance L that solves the outstanding problem of calculating the scaling factor $Sc = Re \cdot D/(4L)$ (introduced by Brouillette), which is an important parameter characterizing the scaling effects of shock waves. The results show that in contrast to macroscopic shock waves, shock waves at micro scale have different propagation mechanism (key issue) which cannot be described by the conventional ‘leaky piston’ model. The main attenuation mechanism of micro shock flow may be the ever slower moving contact surface which drives the shock wave. Different from other measurements using pressure transducers, the current setup for density measurements resolve the whole micro shock flow system for the first time! Furthermore, the shock formation process involving trailing compression waves is experimentally well resolved for the first time, to the best of our knowledge. The rare phenomena of turbulent-laminar transition in a high-speed flow is confirmed by the experiments.

Zusammenfassung auf Deutsch

Diese Arbeit wurde im Rahmen des DFG-Projektes Mikrostoßwellen geschrieben. Dies ist eine Studie über kompressible Überschallströmung mit niedrigen Reynoldszahlen durch Anwendung von ultrakurzem Laserpuls und Interferometrie. Die Mikrostoßwellen haben als makroskopische Stoßwellen unterschiedliche fluidmechanische Eigenschaften aufgezeigt, so dass Mikrostoßwellen seit Beginn des 21. Jahrhunderts als neues Gebiet in der Physik der Flüssigkeit auftauchen. Aufgrund technischer Einschränkungen gibt es jedoch nur sehr wenige Arbeiten auf diesem Gebiet. Darüber hinaus war der Ausbreitungsmechanismus des Mikrostoßströmungssystems (einschließlich Mikrostoßwelle, Grenzschicht, Kontaktfläche und Expansionswellen) bis jetzt unklar. Daher ist die vorliegende Arbeit ein Bericht über Fortschritte in der Stoßwellenphysik.

Tatsächlich wurden die Stoßwellenexperimente im Sub-mm-Bereich bisher nur von zwei Gruppen weltweit durchgeführt (to the best of my knowledge): der Brouillette-Gruppe in Sherbrooke, Kanada, und unserer Gruppe in Emden, Deutschland. Die Gruppe von Brouillette verwendet eine völlig andere Technik, um die Mikrostoßwellen zu erzeugen und zu messen als unsere Technik. Der detaillierte Unterschied wird in dieser Doktorarbeit diskutiert. Darüber hinaus ist das Verkleinern von makroskopischen Objekten auf Mikro-/Nanoskalen heutzutage ein Trend in der Physik, und diese Doktorarbeit trägt zu diesem Trend bei.

Die Arbeiten, die im Rahmen dieses Projekts durchgeführt wurden, sind wie folgt aufgelistet: 1. Untersuchungen der Stoß-Kavitation-Wechselwirkung in Miniaturglasröhren in Wasser. 2. Modifikationen/Verbesserungen des Laser-Differential-Interferometers LDI (die Hauptdiagnose). 3. Entwicklung eines neuartigen Schockerzeugungsverfahrens unter Verwendung eines Laserplasmas als Treiber. 4. Entwicklung eines neuen Schockerzeugungsverfahrens mit einem Hochgeschwindigkeits-Magnetventil. 5. Korrektur der Rankine-Hugoniot-Beziehung für Mikrostoßwellen. 6. Konfrontation der existierenden Theorien über Stoßströmung, d. H. "leaky piston" Modell mit experimentellen Ergebnissen.

Die experimentellen Untersuchungen, die die zwei neuen Methoden zur Erzeugung von Mikrostoßwellen anwenden, bilden den Hauptteil meiner Doktorarbeit:

(A) LIMS - Laserplasma-induzierte Mikroschocks: Ein Femtosekunden-Laserpuls wird auf einen Aluminiumfilm als Ziel fokussiert, um einen optischen Durchbruch zu erzeugen. Aufgrund des plötzlichen Auftretens dieses extremen Ungleichgewichts auf dem Ziel wird eine Stoßwelle von dem Durchbruchpunkt emittiert. Die Stoßwelle wird zunächst durch das expandierende Hochdruckplasma (bis 10 Mbar) angetrieben, das quasi als Kolben dient, bis das Plasma rekombiniert und das heiße Gemisch aus Al und Luft kalt wird.

Die Doktorarbeit präsentiert erstmals experimentelle Untersuchungen zur direkten Erzeugung von Mikroschocks in einer Mikrokapillare/Röhre. In früheren Berichten gab

es keine "direkte" Mikrostoß-Erzeugung, weil eine Stoßwelle zuerst in einem grösseren Rohr erzeugt und dann in einem kleineren Rohr geleitet wurde.

Die Experimente werden unter verschiedenen Bedingungen und in verschiedenen Kapillaren mit 50 μm bis 300 μm hydraulischem Durchmesser durchgeführt. Im Unterschied zu früheren Stoßwellenuntersuchungen mit Druckwandlern oder Schlierenoptiken wird in der vorliegenden Doktorarbeit der LDI für Dichte- und Geschwindigkeitsmessungen eingesetzt. Die 1D-Laserplasmasimulation MULTIfs wird zur numerischen Untersuchung des Stoßwellenbeginnprozesses eingesetzt. Die Fernfeldausbreitung des Mikroschocks in der Kapillare wird durch die Berechnung von 2D-komprimierbaren Navier-Stokes-Gleichungen analysiert. Die MULTIfs-Simulation und die Navier-Stokes-Berechnung stimmen mit den experimentellen Ergebnissen überein. Weiterhin werden die experimentellen Werte mit den theoretischen Werten verglichen, die unter Verwendung der klassischen Rankine-Hugoniot-Beziehung (Dichtesprung als Funktion der Machzahl unter idealen Bedingungen) sowie ihrer korrigierten Version berechnet wurden. Die korrigierte Rankine-Hugoniot-Relation, die in dieser Doktorarbeit vorgeschlagen wurde, berücksichtigt die diffusiven Transportphänomene (aufgrund von Wandreibung und Wandwärmeleitung).

(B) Stoßrohr mit schnellem Magnetventil: Aufgrund des Fehlens eines guten Verständnisses des Ausbreitungsmechanismus des Mikrostoßströmungssystems konzentriert sich die derzeitige Arbeit auf die Messung von Mikrostoßströmungen unter besonderer Berücksichtigung der Kontaktfläche. Ein neuartiger Aufbau mit einer Glaskapillare (mit 200 μm oder 700 μm hydraulischem Durchmesser D) und einem Magnetventil wird angewendet, um eine Stoßwelle mit einer maximalen anfänglichen Machzahl von 1,6 zu erzeugen. Das Laser-Differential-Interferometer wird verwendet, um Messungen der Trajektorien, Geschwindigkeit und Dichte des Mikrostoßflusses durchzuführen. Schlieren-Optik wird auch für Kontrollversuche eingesetzt. Die vorliegende Doktorarbeit stellt die ersten Mikroskalenmessungen der Stoßkontaktdistanz L vor, die das ausstehende Problem der Berechnung des Skalierungsfaktors $Sc = Re \cdot D / (4L)$ (eingeführt von Brouillette) lösen, der ein wichtiger Parameter zur Charakterisierung der Skalierungseffekte von Stoßwellen ist. Die Ergebnisse zeigen, dass Stoßwellen im Mikrobereich im Gegensatz zu makroskopischen Stoßwellen unterschiedliche Ausbreitungsmechanismen haben (Kernfrage), die mit dem konventionellen "leaky piston" Modell nicht beschrieben werden können. Der Hauptdämpfungsmechanismus der Mikrostoßströmung kann die sich immer langsamer bewegende Kontaktfläche sein, die die Stoßwelle antreibt. Anders als bei anderen Messungen mit Druckmessumformern löst, das aktuelle Setup für Dichtemessungen löst das gesamte Mikrostoßsystem zum ersten Mal auf! Darüber hinaus ist der Stoßformationsprozess mit nachlaufenden Kompressionsswellen nach unserem besten Wissen zum ersten Mal experimentell gut aufgelöst. Die seltenen Phänomene des turbulent-laminaren Übergangs in einem Hochgeschwindigkeits-

fluss werden durch die Experimente gezeigt.

Acknowledgement

First and foremost I would like to thank my supervisors Prof. Ulrich Teubner and Prof. Walter Garen. They have given me this unique opportunity to explore both the world of shock waves and the world of laser optics. I am thankful to them for many discussions on various topics. Besides, Walter gave me from time to time ‘micro’ lectures, which ‘largely’ enriched my knowledge in ‘micro’ shock wave. In the labs, Walter taught me a lot of skills to play with diverse optical and fluid mechanical setups. There are many occasions that we improvised new ideas together in the labs. Honestly, there is limited possibility to attend research seminars or colloquiums in Emden, but I am given the chance to participate in multiple domestic and international conferences, which significantly contributed to my study and thus balanced the disadvantage of Emden. I am grateful towards Ulrich for giving me critical comments on my work. He has also given me the chances to participate in the beam times in DESY and FERMI, as well as a short term scientific mission in the Hungarian academy of sciences in Budapest. The big-project experience opened up my horizons and gave me the precious chance to work with teams of scientists from diverse fields. The thereby obtained experience benefits the DFG-project e.g. 1. the idea of shock generation using a special high-speed magnetic valve, which is originally applied in a setup for second harmonic generation. 2. some advanced Matlab programming skills, which are practiced by evaluating the big data from DESY and FERMI.

Theodor Schlegel (Helmholtz Institute, Jena) and David E. Zeitoun (Aix-Marseille University) have piled my work higher and deeper. I am particularly indebted to them for the computer simulations. All these critics and comments make this thesis ‘great again’. It has also been a pleasure to work with all my helpful colleagues, to whom I am very grateful. I also thank DFG for the okayish money.

Last but not least, I would love to thank my parents for supporting me during my whole study.

Statements according to exam regulations

This is a statement that I completed the work independently and used only the cited reference. Parts of the thesis are published as scientific papers, which are to be found in the publication list attached with this thesis. I am here to certify that the guidelines of good scientific practice at the University of Oldenburg have been obeyed. In connection with the Ph.D. project, no commercial placement or consulting services (doctoral consultation) have been used.

Nomenclature

H	enthalpy (extensive)
h	enthalpy (intensive) per unit mass
\mathcal{U}_i	internal energy (extensive)
\mathbb{U}_i	internal energy (intensive) per unit mass
V	volume
V_s	specific volume $V_s = 1/\rho$
S	entropy (extensive)
s	entropy (intensive) per unit mass
U	voltage
u	velocity
λ	wave length
τ	pulse duration
I	intensity
ϕ	optical path difference
ρ	density
γ	heat capacity ratio
Re	Reynolds number
δ	boundary layer thickness
F_f	friction force
Q	total heat flow rate
\mathbb{Q}_f	wall heat conduction per mass flow rate
q	heat transfer per unit mass flow rate
P	pressure
μ	dynamic viscosity
ν	kinematic viscosity
Kn	Knudsen number
Z	acoustic impedance
t	time instant
x	flow propagation distance
D	hydraulic diameter of the capillary
u_s	shock wave velocity
u_p	gas particle velocity behind the shock wave
u_a	local sound velocity
δr	thickness of the mass layer behind the shock
κ	dimensionless Gladstone-Dale constant
G	Gladstone-Dale constant
R	universal gas constant
R_s	specific gas constant
m	mass
w	laser beam $1/e^2$ -radius
subscript 1	region upstream of the shock wave
subscript 2	region downstream of the shock wave, ahead of the contact surface
subscript 3	region behind the contact surface, ahead of the driver gas
subscript 4	region of the driver gas

List of publications

Peer-reviewed journal articles, as the first or corresponding author (one of the main authors):

Ulrich Teubner, **Yun Kai**, Theodor Schlegel, David E. Zeitoun, and Walter Garen. Laser-plasma induced shock waves in micro shock tubes. *New Journal of Physics*, 19(10):103016, 2017.

Yun Kai, Walter Garen, Theodor Schlegel and Ulrich Teubner. A Novel Shock Tube with A Laser Plasma Driver. *Laser and Particle Beams*, 35(4):610-618, 2017.

Yun Kai, Walter Garen and Ulrich Teubner. Experimental Investigations on Microshock waves and contact surfaces. *Physical Review Letters*, 120(6):064501, 2018.

Yun Kai, Walter Garen, David E. Zeitoun and Ulrich Teubner. Formation and hot flow duration of micro shock flows. *Physics of Fluids*, accepted, 2018.

Peer-reviewed journal articles, as co-author (participation in experiments and analysis):

Walter Garen, Ferenc Hegedus, **Yun Kai**, Sandra Koch, Bernd Meyerer, Walter Neu and Ulrich Teubner. Shock wave emission during the collapse of cavitation bubbles. *Shock Wave*, 26(4), pp.385-394, 2016.

Franz Tavella, Hauke Hoepfner, Victor Tkachenko, Nikita Medvedev, Flavio Capotondi, Torsten Golz, **Yun Kai**, Michele Manfreda, Emanuele Pedersoli, Mark Prandolini, Nikola Stojanovic, Takanori Tanikawa, Ulrich Teubner, Sven Toleikis, Beata Ziaja. Soft x-ray induced femtosecond solid-to-solid phase transition. *High Energy Density Physics* 24:22-27, 2017.

Paola Finetti, Hauke Höppner, Enrico Allaria, Carlo Callegari, Flavio Capotondi, Paolo Cinquegrana, Marcello Coreno, Riccardo Cucini, Miltcho B. Danailov, Alexander Demidovich, Giovanni De Ninno, Michele Di Fraia, Raimund Feifel, Eugenio Ferrari, Lars Fröhlich, David Gauthier, Torsten Golz, Cesare Grazioli, **Yun Kai**, Gabor Kurdi,

Nicola Mahne, Michele Manfreda, Nikita Medvedev, Ivaylo P. Nikolov, Emanuele Pedersoli, Giuseppe Penco, Oksana Plekan, Mark J. Prandolini, Kevin C. Prince, Lorenzo Raimondi, Primoz Rebernik, Robert Riedel, Eleonore Roussel, Paolo Sigalotti, Richard Squibb, Nikola Stojanovic, Stefano Stranges, Cristian Svetina, Takanori Tanikawa, Ulrich Teubner, Victor Tkachenko, Sven Toileikis, Marco Zangrando, Beata Ziaja, Franz Tavella and Luca Giannessi. Pulse Duration of Seeded Free-Electron Lasers. *Physical Review X* 7(2):021043, 2017.

Conference papers (full):

Yun Kai, Bernd Meyerer, Walter Garen and Ulrich Teubner. Experimental investigation of laser generated shock waves and the onset of evaporation in a mini-shock glass tube filled with water. Proc. 21st International Shock Interaction Symposium , p168-170, Riga, 2014.

Yun Kai, Walter Garen and Ulrich Teubner. Generation and propagation of shock waves in sub-millimeter capillaries. Proc. 30th International Symposium on Shock Waves, Tel Aviv, 2015.

Walter Garen, Bernd Meyerer, **Yun Kai** and Ulrich Teubner. Experimental Investigation of Shock-Bubble Properties at the Liquid-Air Phase Boundary. Proc. 30th International Symposium on Shock Waves, Tel Aviv, 2015.

Yun Kai, Walter Garen and Ulrich Teubner. The influence of a pulsed driver on the micro shock propagation. Proc. 31th International Symposium on Shock Waves, Nagoya, 2017.

Ulrich Teubner, **Yun Kai**, Theodor Schlegel and Walter Garen. Laser-induced shock waves in micro tubes. Proc. 31th International Symposium on Shock Waves, Nagoya, 2017.

Conference abstracts (without a full paper):

Yun Kai, Walter Garen, Johannes Diekhoff and Ulrich Teubner. Laser-induced breakdown in an aluminum thin film and subsequent shock wave propagation in mini capillary. DPG-Frühjahrstagung, Bochum, 2015.

Yun Kai, Walter Garen and Ulrich Teubner. fs-laser induced micro shock waves in a 50 μm capillary. Proc. 22nd International Shock Interaction Symposium, Glasgow, 2016.

Yun Kai, Walter Garen, Theodor Schlegel and Ulrich Teubner. Unsteady micro shock waves induced by time-dependent driver. DPG-Frühjahrstagung, Bremen, 2017.

Scientific CV

2007 - 2010, University of Oldenburg, Engineering Physics B.Sc.

2010 - 2013, University of Göttingen, Physics M.Sc.

2012 - 2013, Max-Planck-Institute for Biophysical Chemistry (MPIbpc) in Göttingen,
research assistant

2013 - 2018, Institute for Laser and Optics, Emden/Leer University of Applied Sciences,
research associate

2015 - 2018, University of Oldenburg, Ph.D. student in physics

Contents

1	Introduction	27
1.1	General overview and motivation	27
1.2	Brief review of the shock wave research	29
2	Shock related fundamentals	35
2.1	Background fluid mechanics	37
2.1.1	Equation of state, Mach number and enthalpy	37
2.1.2	Isentropic and stagnation relations	40
2.1.3	Mass, momentum and energy conservation	43
2.1.4	Flow with wall friction and heat conduction	45
2.1.5	Navier-Stokes equation	49
2.2	Shock wave theory	50
2.2.1	Rankine-Hugoniot relations	50
2.2.2	Physical properties in a shock tube	55
2.2.3	Entropy growth associated with shock waves	58
2.2.4	Knudsen number	62
2.3	Gaussian optics	64
3	Experimental methods	69
3.1	Laser differential interferometry (LDI)	69
3.2	Schlieren optics using a double-cavity laser	80
3.3	Plasma induced shock waves	82
3.4	Magnetic valve induced shock waves	88
3.5	Measurement error	90
4	Results of micro plasma shock waves	95
4.1	LIMS onset	95
4.2	MULTIfs simulation	97
4.3	Geometric influence on shock wave attenuation	102
4.4	Shock wave propagation in different capillaries	105
4.5	Shock induced mass motion and Reynolds number	111

4.6	Boundary layer development after shock	114
4.7	CFD investigations	116
4.8	Correction of Rankine-Hugoniot relations	122
4.9	Verification of the corrected Rankine-Hugoniot	127
5	Results of micro shock flow	131
5.1	Micro shock wave formation mechanism	133
5.2	Initial pressure and dimensional effects	136
5.3	Driver pressure variation	139
5.4	Oscillograph traces (density histories)	141
5.5	Micro shock flow propagation	147
5.6	Turbulent/Laminar transition of micro shock	151
5.7	‘Leaky piston’ model and correction suggestion	154
5.8	Schlieren photos	163
6	Summary and outlook	167
A	Additional results on mini shock-cavitation interaction	169

List of Figures

1.1	Developments in the shock wave research with selected scientists (not a complete list). Portrait photos are taken from wikipedia with free license for educational use. The arrows without a corresponding box indicate other fields of study.	33
2.1	Control volume analysis of a fluid flow in a tube. ρ density, P pressure, T temperature, u velocity.	40
2.2	A control volume in a tube for studying wall friction and heat conduction. A shock wave is not in this control volume.	46
2.3	Illustration of gas propagating through a shock wave (shock-fixed reference frame).	50
2.4	Change of gas properties across the shock wave.	53
2.5	Theoretical flow Mach number behind the shock wave.	53
2.6	A conventional shock tube. The high pressure chamber is noted as region 4, while the low pressure chamber is noted as region 1.	55
2.7	Snapshot of the distribution of density, pressure, temperature and velocity inside an ideal shock tube (lab frame reference). The sketch is based on shock tube theories in textbooks e.g. [33] and [32].	56
2.8	Illustration for shock wave induced entropy growth (shock-fixed reference frame).	58
2.9	Shock wave induced theoretical entropy change as a function of the Mach number.	60
2.10	Knudsen number ranges of a fluid flow. Kn ranges are defined in [47].	63
2.11	Illustration (A) geometrical optics (B) Gaussian beam. If there isn't a specific note, the radius and diameter are the $1/e^2$ -radius and $1/e^2$ -diameter, respectively.	65
2.12	3D illustration of a gaussian pulse using Matlab.	66
3.1	Basic setup of a laser differential interferometer LDI.	70
3.2	Polarization in the first (from left) Wollaston prism. The different sketch colors correlate with the polarizations indicated in Fig. 3.1.	70

3.3	Photo voltage U as a function of optical phase difference $\Delta\varphi$. For illustration purpose, not a measured curve.	71
3.4	Illustration of the optical path difference OPD between the probe beam and the reference beam. The index of refraction of glass $n_{glass} \approx 1.5$. . .	72
3.5	Laser propagation paths in the 2nd Wollaston prism from the left. . . .	73
3.6	Sketch of the two different arrangements of the LDI. Left: one beam out. Right: two beams in.	76
3.7	A typical oscillograph trace of a shock wave measured by the ‘two beams in’ arrangement of the LDI. The values on the axes are exemplar and trivial for the illustration.	77
3.8	A typical oscillograph trace of a shock flow measured by the ‘one beam out’ arrangement of the LDI. The values on the axes are exemplar and trivial for the illustration.	77
3.9	Measurement of the density behind the shock wave ρ_2 . Red straight line: the probe beam of the LDI is positioned behind the shock wave but before boundary layer development. Dash-dot line: the probe beam travels through the boundary layer. Dot line: the probe beam travels through the curved shock wave.	78
3.10	Beam profiles of the LDI at the plane of the photodiodes. They are displayed on a white screen for adjustment. Left: bad adjustment. Middle: good adjustment. Right: working position	79
3.11	Schlieren setup for imaging the micro shock wave.	80
3.12	Illustration of the LIMS (Laser-plasma Induced Micro Shocks). The gradual color change illustrates the density distribution of the target after exposure. The original idea is developed by my advisers Teubner and Garen.	82
3.13	SEM (Scanning Electron Microscope) image of a target with a 50 nm Al layer after shock wave generation via plasma in front of a 50 μm tube (front view). $I = 2 \times 10^{13} \text{ W/cm}^2$, $E_L = 20\mu\text{J}$	83
3.14	The setup for the LIMS experiments. The upper figure is a zoom-in view of the area indicated by the white circle.	83
3.15	Transmission and reflection measurements of the fs-laser beam.	85
3.16	Experimental setup. Diagnostics by the LDI. Shock wave generation by the high-speed magnetic valve. Blue: shock wave and related variables, purple: capillary.	88
3.17	Illustration of the measurements. Top: measurements using the LDI with the ‘two beams in’ arrangement. Bottom: measurements using the LDI with the ‘one beam out’ arrangement. (refer to section 3.1) ‘pos.’ is short for position.	90

3.18	Illustration for data reading using a Matlab-script. Top: an oscillograph trace and a smoothed oscillograph trace of the shock wave measured by the ‘two beams in’ arrangement of the LDI. Bottom: derivative of the smoothed oscillograph trace.	91
3.19	Density histories of a shock wave measured five times (repeated under the same conditions) by the ‘one beam out’ LDI arrangement.	92
4.1	fs-laser beam profiles intended for the 50 μm capillary. Left: beam for quasi point-like shocks generation with the focus diameter of 6 μm (FWHM). Right: beam for quasi planar driver with the focus diameter of 21 μm (FWHM).	95
4.2	MULTIfs simulation of the density (spatial) profiles of the LIMS at initial stage (t from 0 to 1 ns). Different time instant corresponds to different color.	98
4.3	MULTIfs simulation of the density (spatial) profiles of the LIMS at initial stage.	99
4.4	Wave diagram of the LIMS at initial stage, retrieved from the simulated data in Fig. 4.2 and 4.3. ‘den. pro.’ is short for density profile and ‘pres. pro.’ for pressure profile.	100
4.5	Shock wave velocity development of the LIMS at initial stage. Retrieved from the MULTI-fs simulation data of the flow velocity.	100
4.6	Shock wave attenuation affected by geometrical confinement from the capillary. The diagram shows the shock wave velocity u_s as a function of propagation distance x . 1. quasi planar plasma driver in a 50 μm capillary; 2. quasi point-like driver in a 50 μm capillary; 3. in free air, without a capillary. The experimental points are obtained from the time-of-flight method. Same laser energy E is applied for all geometries. Solid fit curves: modified Sedov-Taylor relations.	102
4.7	Illustration of the quasi planar and quasi point-like initial shocks.	103
4.8	Shock wave ‘t-x’ diagram determined by LDI. Red dash lines indicates wave propagation at sound speed. The laser intensity is the same for all experiments. Extrapolation of the 200 μm capillary is made till sound wave propagation.	105
4.9	Shock velocity u_s attenuation in capillaries of different diameters. u_s is determined experimentally by the time-of-flight method.	106
4.10	Shock Mach number $M_1 = u_s/u_a$ attenuation in capillaries of different diameters. Recalculated from Fig. 4.9.	107
4.11	Relative trajectory derived from Fig. 4.8. Solid lines are allometric fits.	107

4.12	The development of the density jump across the shock in the 50 μm capillary. The error bars here correspond to the standard deviation resulted from the shot-to-shot errors.	108
4.13	Form of the shock wave in Top: near-field (close to the onset position); Bottom: far field (fully developed, away from the onset).	109
4.14	Illustration of the detection of a shock wave using the LDI. The oscillograph trace is taken at $x = 1000 \mu\text{m}$ in the 50 μm capillary. The sharp rising and falling edges are caused by the shock wave. The dotted circles highlight the expansion wave signal.	109
4.15	The oscillograph traces (normalized by the maximum voltage of the working range U_0) corresponding to the shock detections in the 50 μm capillary. ‘two beams in’ arrangement of the LDI	110
4.16	Illustration of gas propagating through a stagnate shock wave in a capillary. The shock-fixed reference system is applied.	111
4.17	Velocity of the shock induced mass motion plotted against the propagation distance. Derived from the trajectory fit.	112
4.18	The Reynolds number Re_2 closely behind the shock front as a function of the normalized propagation time (t_{sw} is the time, when the shock wave has slowed down to sound wave velocity; see last section).	113
4.19	Boundary layer development in the capillary. The dash lines indicate the boundary layer thickness, while the block circle indicates an exemplar gas particle.	114
4.20	Relative maximum boundary layer thickness $2\delta/D_{max}$ in the capillary as a function of normalized shock propagation time t_1/t_{sw}	115
4.21	Calculated centerline pressure distribution at different times t in a 200 μm diameter capillary.	118
4.22	Velocity contours (m/s) at three different times in the 200 μm diameter capillary.	119
4.23	Shock wave velocity along the 200 μm capillary. Comparison of experiments (labeled exp.) and numerical simulations (labeled num.).	119
4.24	Influence of initial pressure ratio on shock wave velocity along the 100 μm capillary.	120
4.25	The shock wave velocity along capillaries for the three cases: 200, 100 and 50 μm diameters.	120
4.26	Comparison of the experimental (exp) and numerical shock wave velocity behaviour in a 100 μm capillary for different computations (correlation, Navier-Stokes, boundary layer and Euler). Published in [17].	121
4.27	Snap-shot sketch of a shock flow in a shock-fixed reference frame. The shock front is treated as infinitely thin.	123

4.28	Matlab simulation of the density jump for LIMS in the 200 μm capillary.	127
4.29	Matlab simulation of the density jump for LIMS in the 100 μm capillary.	128
4.30	Matlab simulation of the density jump for LIMS in the 50 μm capillary.	128
4.31	Density jump across the plasma shock wave as a function of the shock Mach number in the 50 μm capillary.	129
5.1	A snap-shot like illustration of a micro shock flow in a capillary. Region (1) is in front of the shock, region (2) is between shock and contact surface, region (3) is between contact surface and expansion waves, region (4) is the high pressure driver. Default setting is $P_4 = 8$ bar He, $P_1 = 1$ bar air at normal conditions, otherwise special comments are given. . .	131
5.2	Shock wave measurements in the 200 μm capillary at different propagation distances x . ‘two beams in’ arrangement of the LDI. $P_4 = 8$ bar He, $P_1 = 1$ bar air.	133
5.3	Compression waves (partial shock waves) in the 200 μm capillary at $x = 45$ mm. ‘two beams in’. $P_4 = 8$ bar He, $P_1 = 1$ bar air.	134
5.4	Micro shock waves in the 200 μm capillary at $x = 45$ mm and $x = 50$ mm. ‘two beams in’. $P_4 = 8$ bar He, $P_1 = 1$ bar air.	134
5.5	Micro shock propagation in the 200 μm capillary. The shock velocity u_s is plotted against the distance x between the valve and the detection spot. Normalized values are displayed in red for special positions. $P_4 = 8$ bar He, $P_1 = 1000$ mbar air. Measured by the ‘two beams in’ arrangement.	136
5.6	Micro shock propagation in the 200 μm capillary. ‘two beams in’. $P_4 = 8$ bar He, $P_1 = 500$ mbar air.	137
5.7	Micro shock propagation in the 200 μm capillary. ‘two beams in’. $P_4 = 8$ bar He, $P_1 = 200$ mbar air.	137
5.8	Micro shock propagation in the 200 μm and 300 μm capillaries. The range $x > 140$ mm is chosen for comparison, because both shock waves have linear attenuation here (‘far field’) . ‘two beams in’. $P_4 = 8$ bar He, $P_1 = 1$ bar air.	138
5.9	Shock wave Mach number as a function of the driver/driven pressure ratio. Measured in the 500 μm capillary at the position $x = 340$ mm (not too close to the formation phase but also not too far away). Driver gas is nitrogen with variable P_4 from 8 bar to 20 bar. Driven gas is air with $P_1 = 1$ bar.	140

5.10	Oscillograph traces (with normalized voltage) of the shock flows in the 200 μm capillary at different propagation distance x . The dash-dot line indicates the decreasing shock-induced density jump ρ_2/ρ_1 . The normalized photo voltage $U(t)/U_0$ scales with the flow density $\rho(t)$ through Eq. 3.16. ‘One beam out’ arrangement of the LDI. $P_4 = 8$ bar He, $P_1 = 1$ bar air.	141
5.11	Oscillograph traces (with normalized voltage) of the shock flows in the 200 μm capillary at different propagation distance x . ‘One beam out’ arrangement of the LDI. $P_4 = 8$ bar He, $P_1 = 1$ bar air.	143
5.12	Temporally shifted shock flow oscillograph traces in the 200 μm capillary; turbulent boundary layer at $x < 140$ mm. $P_4 = 8$ bar He, $P_1 = 1$ bar air.	144
5.13	Temporally shifted shock flow oscillograph traces in the 200 μm capillary; laminar boundary layer at $x \geq 140$ mm. $P_4 = 8$ bar He, $P_1 = 1$ bar air.	145
5.14	Shock flow oscillograph traces in the 200 μm capillary; Reproducibility check by five times repeated measurements; Left: measurements at $x = 110$ mm; Right: measurements at $x = 170$ mm. $P_4 = 8$ bar He, $P_1 = 1$ bar air.	146
5.15	The flow trajectories in the 200 μm and 300 μm diameter capillaries. Error bars derived from standard deviation are smaller than the symbols here. Theoretical prediction from Roshko. $P_4 = 8$ bar He, $P_1 = 1$ bar air. The fit function is double exponential, i.e. $x_{c,fit}(t) = A_1 \exp(-t/B_1) + A_2 \exp(-t/B_2) + y_0$	147
5.16	Shock-contact distance L as a function of shock location x_s . Derived from shock wave and contact surface trajectories in Fig. 5.15 via the relation $L(x_s) = x_s(t) - x_{c,fit}(t)$. $P_4 = 8$ bar He, $P_1 = 1$ bar air.	149
5.17	Shock wave velocity u_s (direct measurement, ‘two beams in’), contact surface velocity u_c (derived from fit) and post-shock particles velocity u_p (indirect measurement) as functions of propagation distance x . $P_4 = 8$ bar He, $P_1 = 1$ bar air.	150
5.18	Density jump ρ_2/ρ_1 across the micro shock as a function of propagation distance x in the 200 μm capillary. $\rho_1 = 1.205 \text{ kg/m}^3$ is atmospheric air density. $P_4 = 8$ bar He, $P_1 = 1$ bar air.	151
5.19	The development of the Reynolds number behind shock Re_2 in the 200 μm capillary. $P_4 = 8$ bar He, $P_1 = 1$ bar air.	152
5.20	The development of the Darcy friction factor λ of the post-shock flow in the 200 μm capillary. $P_4 = 8$ bar He, $P_1 = 1$ bar air.	153

5.21	Sketch of a shock flow in a tube in a contact-fixed reference system. Top: a shock flow with boundary layer development. Bottom: a shock flow with thin boundary layer assumption.	154
5.22	Shock-contact distance as a function of shock position. The experimental data are derived from the wave diagram in Fig. 5.15.	158
5.23	Hot flow duration τ_{hot} as a function of position x . $P_4 = 8$ bar He, $P_1 = 1$ bar air.	159
5.24	The dimensionless hot flow duration T_{hot} plotted against the dimensionless distance of the shock wave from the valve X . The build-in figure is conventional macroscopic shock tubes results taken from [35] (T_{hot} is notated as T here; tube 7.62 cm diameter) as a comparison.	160
5.25	Relative maximum boundary layer thickness $2\delta/D_{max}$ in the capillary as a function of the hot flow duration τ_{hot} . $P_4 = 8$ bar He, $P_1 = 1$ bar air.	161
5.26	Schlieren image of a shock wave in a 300 μm capillary near the exit; $P_4 = 20$ bar N_2 , $P_1 = 1$ bar air. Valve is at the left side (not shown in the photograph)	163
5.27	Schlieren image of a shock wave shortly after exiting a 300 μm capillary; $P_4 = 20$ bar N_2 , $P_1 = 1$ bar air.	163
5.28	Schlieren image of a shock wave at the exit of a 300 μm capillary; double exposures with time difference of 500 ns; $P_4 = 20$ bar N_2 , $P_1 = 1$ bar air.	164
5.29	Illustration of the shine ‘thickness’ due to shock front curvature.	164
A.1	Experimental setup to generate and investigate shock waves in a mini-shock tube.	170
A.2	Laser-induced breakdown with subsequent shock wave and cavitation bubble formation in a water-filled glass tube with $d_{in} = 6$ mm. The scale indicated in (d) applies for all photos.	171
A.3	Evolution of the shock wave, vapor bubbles and shock-bubble interactions in a glass tube with $d_{in} = 6$ mm.	172
A.4	Bubble collapse and emission of collapse shock waves in a glass tube with $d_{in} = 6$ mm; inter frames time is about 100 ns	173
A.5	Shock and rarefaction wave development and the onset of vapor bubbles, respectively, in a water-filled glass tube with $d_{in} = 1.7$ mm.	174
A.6	Shock wave induced evaporation in the time line of the cavitation bubble development. Bubble measured by Laser Shadow Method (LSM) [90].	175

List of Tables

3.1	Gas properties of two typical gases used in shock wave research. Data originate in [57] and [58]. Properties correlate with normal conditions (20 °C, 1 atm) and the vacuum wave length $\lambda = 632.8$ nm (HeNe laser line).	74
4.1	Parameters (max. 5% error) for shock wave generation. ‘quasi planar’ and ‘quasi point-like’ correspond to the geometry of the plasma as shock driver.	96
5.1	Slopes of the shock attenuation in the 200 μm and 300 μm capillaries. Data retrieved from Fig. 5.5, 5.6, 5.7 and 5.8. $P_4 = 8$ bar He, variable P_1 of air.	137
5.2	Initial shock Mach number $M_{1,i}$. Data retrieved from Fig. 5.5, 5.6, 5.7 and 5.8. $P_4 = 8$ bar He, variable P_1 of air.	138
5.3	Shock wave arrival time t determined using the Schlieren optics and the LDI for the same positions. Each measurement is reproduced 10 times. $P_4 = 20$ bar N_2 , $P_1 = 1$ bar air.	164

Chapter 1

Introduction

1.1 General overview and motivation

At the SFO airport in San Francisco in 2015, officer Reno from the U.S. Customs and Border Protection has given me the three most essential questions in philosophy: Who are you? Where do you come from? And where are you going? At the very beginning of this thesis, I would like to forward these three questions to shock wave.

1. Who or what is shock wave?

Shock wave is a pressure wave with supersonic velocity. Shock wave is a representative [1] natural phenomenon in the supersonic compressible fluid mechanics. It is ‘representative’, because a supersonic flow is always accompanied by a shock wave.

2. Where does shock wave come from?

Shock wave comes from both the nature and man-made objects. In the nature, shock wave occurs in supernova explosion and solar wind (when it encounters the magnetic field of the earth). A typical example of shock wave from every day’s life is the sonic boom generated by an airplane (e.g. Concorde) breaking the sound barrier. Shock wave is a fringe science related with many different fields of research. In the field of supersonic aerodynamics, especially in most recent developments in scramjet, shock waves help to compress the gas flow inside it’s combustion engine, where movable components such as the turbine are no more needed. The blast shock waves mitigation is also an important topic since decades. Most recently in the electrohydrodynamics, shock waves are induced by the plasma actuator, and applied for flow control on airplanes [2].

3. Where is shock wave going?

In the labs, shock wave is going to two places: huge shock tunnels and tiny micro tubes (quite recently). Firstly, this is to say, shock waves continue to be investigated in the scope of ‘big science’ such as astrophysics [3, 4], aerospace technology [2, 5], high energy density physics [6] (including inertial confinement fusion [7]) etc.

Secondly, in the scope of ‘small science’, shock waves are down scaled to miniature and microscopic dimensions in the recent decades. Besides the fundamental researches such as [8–17] (will be discussed in details in section 1.2), shock waves at smaller scale have found application in the fields of artificial insemination [18], drug/vaccine delivery [19], rare metal recycling from integrated circuits [20], micro gas turbine [21] etc. The application makes use of shock wave’s nature that the shock front drags gas particles from behind into motion (a sound wave can’t do this). Thus shock wave can be applied to assist mass transport. However, knowing is not understanding. What the scientific community does know is that, the pioneer experiments of Duff [22] have shown that the down scaled shock waves can’t be simply described by the classical fluid mechanical theories. But what laws governs the regime of the micro shocks? What’s the formation and attenuation mechanism of micro shocks? Although there are numerous reports on the big scale shock waves, the small scale shock waves are new to the scientific community. Many aspects of the micro shock waves are still not fully understood. Thus there is a strong need of experiments on micro shocks, and this work provides the experimental results.

It shall be remarked that micro and macro shock flows can have even more fundamental differences, due to different governing regimes of atom/molecule physics and continuum mechanics. The validity of continuum mechanics can be indicated by the well-known Knudsen number $Kn = \Lambda/D$ with Λ as collisional mean free path and D as the hydraulic diameter. The Knudsen number for our experimental conditions is in the range $0.001 < Kn < 0.01$ for our smallest tube with $D = 50 \mu\text{m}$, because $\Lambda \approx 68 \text{ nm}$ for atmospheric conditions [23]. The Kn here is also comparable with the one in the theoretical work [24]. Therefore, as we will see, although the micro shock waves in the current work is different than macro shock waves due to non-negligible diffusive transport phenomena, continuum mechanics still applies here. If the hydraulic diameter of the shock flow is further downscaled from μm to sub- μm scale, Kn could be close to 1, thus molecular physics and statistical mechanics should be considered.

This work studies one of the smallest shock waves in the world, to the best of my knowledge. Different from all the aforementioned publications, this work presents not just new results, but also new perspectives (as described in the abstracts) for mini and micro shock waves. This thesis begins with the theory chapters that cover the world of fluid mechanics and the world of optics. Followed by a chapter describing several different experimental setups that mainly built by myself (otherwise, special comments). The chapters covering the results are the next to come. In the end, there is general conclusion chapter with outlooks. The detailed outlooks shall help the newcomers in this field for the kick-start.

1.2 Brief review of the shock wave research

An illustration for the brief review is displayed in Fig. 1.1. Shock wave research is part of the family of fluid mechanics. In this section, we focus on the shock wave, not the overall fluid mechanics. But simply out of interest, I want to shortly mention that the historical major contributors to fluid mechanics include Zhang Heng, Newton, Euler, Bernoulli etc. It is well known that Newton dedicated his second book of the *Principia* to fluid mechanics. In my literature research, I also read about Zhang Heng who may be less known in the western. He is actually the inventor of the world's first water-powered armillary sphere to assist astronomical observation. Furthermore, Zhang Heng improved the inflow water clock and invented the world's first seismoscope [25].

Now we review the shock wave research, which dates back to the time of Stokes [26] in 1848 (the same Stokes known from the famous Navier-Stokes equations). He has possibly made the first [26] speculation that pressure jumps can propagate in a compressible medium with a velocity higher than the speed of sound. These pressure jumps are nowadays named as shock waves. First attempts for a mathematical description were made by Airy in 1849 and Eamshaw in 1859 [26]. The mathematician Bernhard Riemann [27] (well known for his number theory) was also involved in the shock wave research. He described the transformation of a compression wave to a shock wave for the first time in 1860. Riemann's doctoral thesis adviser was the great mathematician Carl Friedrich Gauss in Göttingen university. However, the direct involvement of Gauss in shock wave research is unclear due to lack of documentation.

WJ Macquorn Rankine [28] made the theoretical calculations concerning the change of the gas state in a shock wave in 1870. In 1887, Pierre Henry Hugoniot [29] discovered the increase of the entropy in a shock wave. Nowadays, their names stand for the famous set of equations describing the change of the gas state across a shock front, namely the Rankine-Hugoniot relations. The validity of these relations will also be discussed in this thesis. Because shock waves are transparent and move rapidly, special techniques are needed to make them visible and measurable. Also in 1887, the ingenious scientist Ernst Mach [30] made one of the first (maybe even the first) Schlieren photograph of a shock wave, which is generated by a flying bullet from a firearm.

The first shock tube in the modern sense (diaphragm/membrane technique) is invented in 1889 by Paul Vieille [31]. That's why in the ISSW (International Symposium on Shock Waves) conference there is always a so-called Paul Vieille lecture. After that invention, a shock tube is usually applied as the instrument to study shock waves in the labs. A typical conventional shock tube using diaphragm technique has the hydraulic diameter of centimeters, where the friction and heat conduction play a minor role in the shock propagation, because the volume to area ratio is big enough. The classical

theories (such as Rankine-Hugoniot relation) on shock waves thus ignored the friction term in the momentum conservation equation and the heat conduction term in the energy conservation equation. The classical shock wave research is well described by the textbooks such as [32] and [33].

Down-scaling:

In the last few decades the shock flow is down-scaled, in order to study high-altitude aerodynamics, microfluidic, shock-assisted combustion in micro engines made by MEMS etc. In these cases, diffusive transport phenomena or called dissipative processes (caused by the wall friction and heat conduction) become non-negligible. Therefore the so-called scaling effects came into the spotlight ever since. The downscaling means lowering the Reynolds number of the flow. In the experiments, this can normally be achieved via making either the initial pressure P_1 lower (thus lower initial density ρ_1 , by constant temperature) or the hydraulic diameter D smaller. These two different down-scaling approaches shall be theoretically equivalent [8], if the same Reynolds number occurs. Of course, it shall be further tested whether the two procedures are truly equivalent at micro scale.

Down-scaling through lower initial pressure:

The scaling effects are firstly investigated in a conventional shock tube at low P_1 . In late 1950s, the pioneer experiments on scaling effects are done by Duff [22], who has experimented with an electron-canon as a densitometer. He concluded that the testing time for a given tube diameter is a function of initial pressure and not of expansion chamber length. The shock flows with low P_1 are further studied by Roshko [34], who measured the flow duration and proposed the ‘leaky piston’ model. Roshko verified Duff’s assumption that the loss of flow duration at low pressure shock tubes is mainly due to the loss of shocked gas by leakage of the boundary layer past the contact surface. The tube wall can alternatively be regarded as a mass sink. He also concluded with Duff that the deceleration of the shock wave toward the contact surface plays an important role in its over-all deceleration. In the ‘leaky piston’ model, the contact surface eventually propagates at the same velocity as the shock wave (so called limiting regime). In the 1960s, the boundary layer development is systematically measured by Mirels, who also modified Roshko’s model [35] and later proposed the correlation formulas for laminar shock tube boundary layer [36]. Later in the 1970s, Garen et al. [37] have experimented with shock tubes that use a rubbery ball valve instead of a diaphragm, where the modified ‘leaky piston’ from Mirels agree well with the experiments. At the end of the 1970s, Zeitoun [38] numerically verified the aforementioned diverse experiments in low pressure tubes. In his simulation, the evolution of the hot flow quantities due to the interaction between the boundary layer and inviscid hot flow are taken into account. A better knowledge of the unsteady evolution of hot flow is ob-

tained including the distribution of all parameters at the limiting regime, particularly the maximum shock-contact distance and the hot flow duration (test time).

Later in the experimental part of this thesis, we will compare our results with this ‘leaky piston’ model, where surprising difference is observed and explained.

Down-scaling through lower hydraulic diameter (may combine with lower pressure):

The down-scaling approach through P_1 has technical limitations e.g. the flow visualization or detection becomes less sensitive by lower pressure. Logically, the other approach by lowering the hydraulic diameter D is then needed. Entering the 21st century, the work on smaller D is started in Tohoku University, Japan mainly by Takayama and his student Sun [8]. Miniature and micro scales experiments are done by Brouillette [9] and then Mirshekari et al. [10–12], who have investigated micro shocks by experiments and simulations (1D model). Specially Brouillette introduced a dimensionless scaling factor, which is nowadays established as an important parameter for characterizing the scaling effects of shock flows. In the first decade of the 21st century, Garen et al. [39, 40] have experimented with smaller shock tubes using the ball valve. The smallest one from this type of shock tubes has the diameter of 1 mm. An electron gun or a laser differential interferometer was applied to detect the shock flow. It is found that the shock Mach number is not only a function of the driver/test gas pressure ratio but also of the Reynolds number. The contact surface (the front of the driver gas) was also investigated in Garen’s works. The theoretical work on micro shocks is then carried on by Zeitoun et al. [13], who have simulated the flows in micro shock tubes using compressible 2D Navier-Stokes equations combined with slip conditions. In 2010, Ngomo et al [41] have also done a numerical study for MEMS related research using an 1D model, which is based on Rayleigh-Fanno flow (i.e. considering viscosity and heat loss). In their conclusions, they stated that viscosity is the primary cause for the attenuation of the propagating shock in narrow tubes. In 2011, Austin et al. [15] used a cookie-cutter like (a bigger tube connected with a smaller tube) shock tubes system to perform measurements in the smaller tube with 1.65 mm diameter over the length of 2000 times diameters. They have observed the significant viscosity and the late time pressure rise in their pressure histories measurements, which agree with Brouillette’s observations. Austin further performed simulations (well consistent with their experiments) by including the boundary layers and channel entrance effects (due to the diameter mismatch). As a comment, a small entrance diameter mismatch also happens in this project (in the valve experiments).

Most lately in 2016 and 2017, Deshpande and Puranik [16, 24] have first applied a house code and then the code ANSYS Fluent (both based on Navier-Stokes equations i.e. assuming continuum mechanics) to numerically investigate the shock propagation in 3D microducts, where the scaling factor is again applied in the simulation. Their

work was able to interpret the micro shock attenuation through the diffusive transport phenomena due to the wall friction and heat conduction in the post-shock flow field, in addition to the behavior of the boundary layer. They have concluded that the isothermal boundary condition at the shock tube wall is sufficient for the modeling. Furthermore, it is concluded that the conductivity and thickness of the wall material have negligible effect on the shock attenuation. Importantly, their numerical results agree well with the aforementioned experimental works of Brouillette and Mirshekari. Consequently in this thesis, the analysis of the shock propagation/attenuation will base on the flow characteristics in the post-shock field as well.

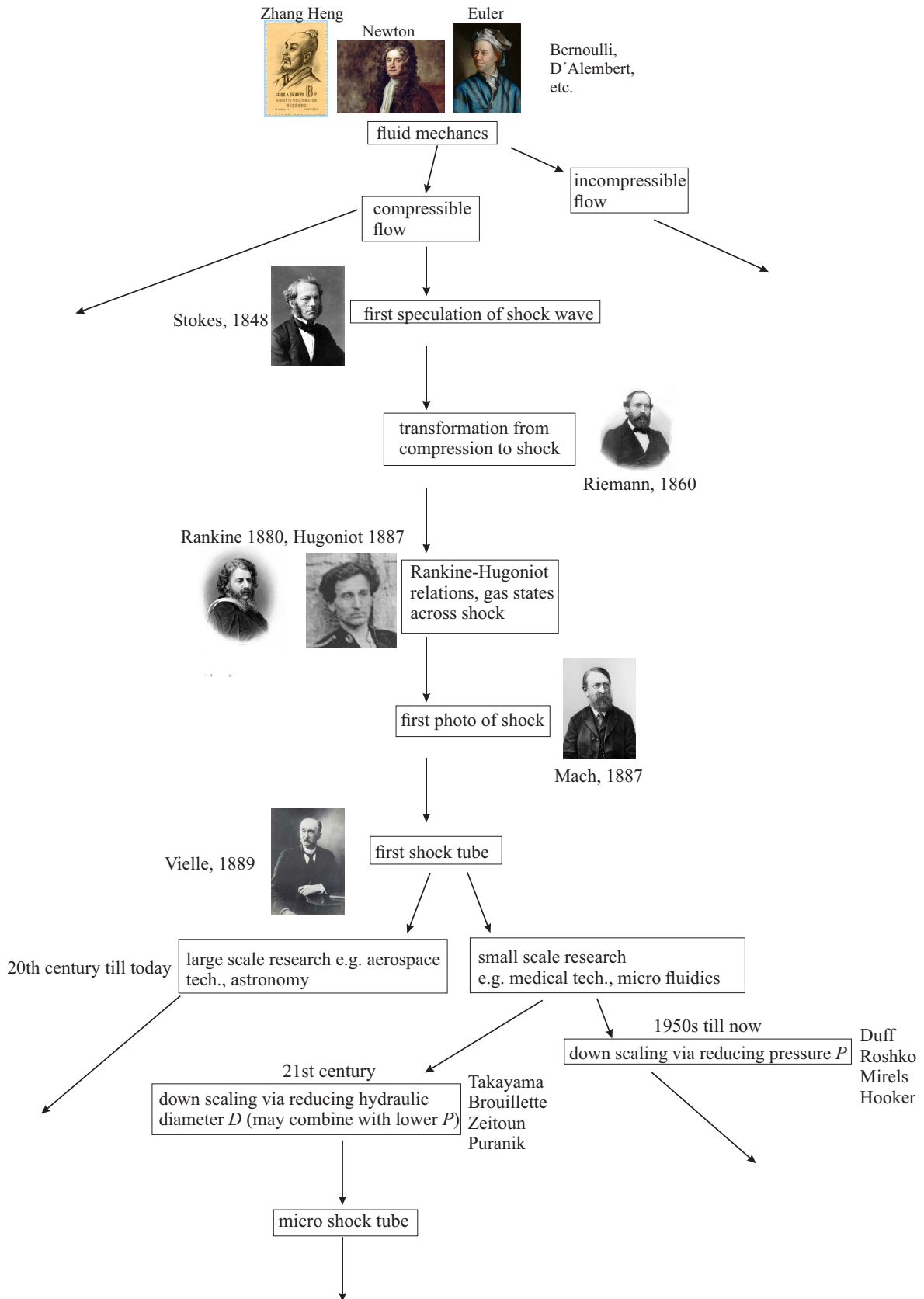


Figure 1.1: Developments in the shock wave research with selected scientists (not a complete list). Portrait photos are taken from wikipedia with free license for educational use. The arrows without a corresponding box indicate other fields of study.

Chapter 2

Shock related fundamentals

What fundamental theories do we need, in order to study the micro shock wave? This chapter shall answer this question.

The relevant back ground theories of fluid mechanics are firstly explained. Theoretical curves are plotted using the same range of parameters as the experiments, so that this theory chapter has direct connection to the project. Theories from diverse textbooks and online courses (will be cited at corresponding locations) are highly summarized and rearranged to a form that can be directly used for this project. Therefore, this chapter is not just a simple display of the related back ground theories, but also a certain way of interpretation from me. Since this thesis mainly covers an experimental project, the theoretical part is kept brief.

Before going into details, some basic concepts relating to this project need to be clarified.

1. Adiabatic process: no external heat transfer.
2. Reversible process: after this process has taken place, it can be reversed. When the process is reversed, the system and its surroundings return to their initial states. Reversibility also means that the reaction operates continuously at equilibrium. The energy from work performed by or on the system would be maximized, and that from heat would be zero.
3. Isentropic process: both adiabatic and reversible. The stagnation process (an imaginary process) of a shock wave is conventionally treated as isentropic in textbooks, in order to calculate the total enthalpy.

At this point, one may ask: because the conventional shock related theories treat the shock propagation as adiabatic, is the shock propagation reversible? The answer is no. The shock propagation isn't reversible, thus certainly not isentropic. Because inside the shock wave structure, the velocity and temperature gradients are large, thus the viscosity and thermal conduction **inside** the shock wave structure does contribute to the growth of entropy. Since the entropy growth indicates the direction in which a natural process occurs, the shock wave propagation is directional, i.e. irreversible. The

stagnation process of a shock wave is an another story, because it is an imaginary process which serves the mathematical calculations only.

One step further, the shock waves at micro scale (i.e. micron hydraulic diameter) has non-negligible external dissipative phenomena. Because friction scales with $1/D$ and the heat conduction scales with $1/D^2$, shock waves in smaller tubes experience stronger dissipative phenomena. Therefore, shock waves in micro tubes lead to even higher growth of entropy than in conventional macro tubes.

The structure of this chapter: it begins with sections covering basic fluid dynamics. And then, the chapter further contains the sections on a specific phenomenon in compressible fluid mechanics: the shock waves. Later on, the related basic optics will be covered, since this project applies optical methods for the diagnostics and shock onset.

2.1 Background fluid mechanics

In this section, relevant background knowledge of fluid mechanics is explained for later use.

2.1.1 Equation of state, Mach number and enthalpy

This section deals with the equation of states for ideal gas. The equation of states relates the various thermodynamic properties:

$$P = \rho R_s T \quad (2.1)$$

R_s is specific gas constant, which is the universal gas constant divided by molecular mass.

Now, we want to know how the variables in the equation of states are related to other thermodynamic variables. To do this, we take a look at the specific heat of the gas.

It is well known that, the specific heat capacity (or simply called specific heat) for constant volume c_V is defined as:

$$c_V = \left. \frac{\partial \mathbb{U}_i}{\partial T} \right|_V \quad (2.2)$$

\mathbb{U}_i is internal energy.

The specific heat for constant pressure is defined as:

$$c_P = \left. \frac{\partial h}{\partial T} \right|_P \quad (2.3)$$

where h is enthalpy.

The ratio of specific heats is:

$$\gamma = \frac{c_P}{c_V} \quad (2.4)$$

This is an important parameter governing the compressible flow behavior [32, 42]. Later in the thesis one will see that quantities such as the density ratio across shock waves or the factor by which temperature increases when a flow is brought to rest can be expressed in terms of Mach number M and γ alone.

As usual, Mach number is defined as:

$$M = \frac{u}{u_a} \quad (2.5)$$

with the local sound velocity u_a . As a rule of thumb, when $M > 0.3$, the gas flow is conventionally treated as compressible. This is, of course, the case for shock wave which has $M > 1$.

The specific gas constant is related to c_P and c_V by the relation:

$$R_s = c_P - c_V \quad (2.6)$$

As a result of Eq. 2.4 and 2.6, the specific heats can be expressed by using only γ and R_s :

$$c_P = \frac{\gamma R_s}{\gamma - 1} \quad (2.7)$$

$$c_V = \frac{c_P}{\gamma} = \frac{R_s}{\gamma - 1} \quad (2.8)$$

For temperature below 1000 K, the specific heats are approximately constant, and the gas can be modeled as calorically perfect (e.g. in [32, 42]). This means that the change in internal energy between two states is c_V times the change in temperature. Derived from Eq. 2.2:

$$\Delta U_i = \int_{T_1}^{T_2} c_V dT = c_V \Delta T \quad (2.9)$$

This equation above can be integrated, which leads to the relation between internal energy and temperature (for ideal and calorically perfect gas):

$$U_i = c_V T \quad (2.10)$$

Similarly, derived from Eq. 2.3 for enthalpy:

$$\Delta h = \int_{T_1}^{T_2} c_P dT = c_P \Delta T \quad (2.11)$$

The integration of the equation above leads to the relation between enthalpy and temperature (for ideal and calorically perfect gas):

$$h = c_P T \quad (2.12)$$

The definition of the (intensive) enthalpy is:

$$h = U_i + \frac{P}{\rho} = U_i + P V_s \quad (2.13)$$

with specific volume V_s . Enthalpy includes the internal energy, which is the energy required to create a system, and the amount of energy required to make room for it by displacing its environment and establishing its volume and pressure.

At low temperatures, the molecules in a gas undergo random translational (3 degrees of freedom) and rotational (2 degrees of freedom for di-atomic molecules) motions. Temperature is a measure of the energy of the random motions. Collisions with other

molecules are generally not strong enough to excite the molecules to vibrate at low temperatures. Once the temperature is high enough though, vibrational excitation starts to occur. Above 1000 K, the specific heats increase because the individual molecules that make up the gas begin to vibrate. This means that in order to raise the temperature of the gas, more energy is required because it will be soaked up by these vibrations in addition to random translational motions and rotation. If more energy is required for a given change in temperature, this means that specific heats have been increased. (well known in text books or lecture notes e.g. [42, 43])

For the experiments in this work, the temperature behind shock front in the far field (where the shock wave is fully developed) is considerably lower than 1000 K, which is shown in the simulations. Therefore, the ideal gas law applies and the gas is calorically perfect in the far field. Near the optical breakdown position, the temperature can be as high as 10^5 K (around 10 eV) under the current experiment and simulation conditions (shown by the MULTI-fs simulation, published in [17]). Thus in the near field of the plasma shock wave, the ideal gas law doesn't apply, but equation of states for real gas does (as tables from data bank, which will be discussed later in the results section). For the magnetic valve induced shock waves, the ideal gas law applies for both the near field and the far field.

2.1.2 Isentropic and stagnation relations

An isentropic flow is a flow with constant entropy. It has no irreversible losses and no heat addition. Isentropic flows are simple in mathematics, but by studying them one can begin to discover some interesting counter-intuitive phenomena that occur in high Mach number flows. For example, when a flow needs accelerating, intuitively we're used to a converging nozzle. However, it needs a diverging nozzle to accelerate supersonic flow exiting the magnetic valve. The reason for this lies in the energy conversion.

A shock wave is not an isentropic flow, which has been explained in the beginning of this chapter. But the theories of isentropic flows can be applied to study the stagnation pressure ahead and behind the shock wave. Via the change of the stagnation pressure, one can calculate the entropy change across a shock wave (e.g. in [32, 42]).

In this section, we assume an isentropic flow going through the control volume in Fig. 2.1.

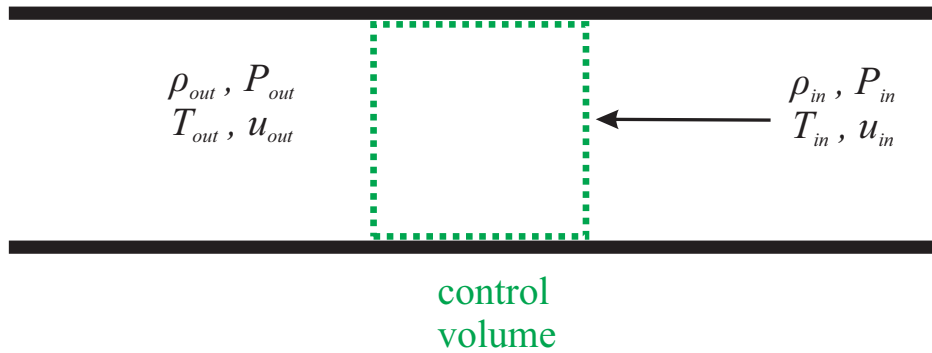


Figure 2.1: Control volume analysis of a fluid flow in a tube. ρ density, P pressure, T temperature, u velocity.

The first law of thermodynamics is the starting point of our explanation for the isentropic relations:

$$d\mathcal{U}_i = \delta Q - \delta W \quad (2.14)$$

with \mathcal{U}_i as extensive internal energy. The different notations in d and δ are due to the reason that internal energy is a function of state, while heat and work are not. A function of state is a function defined for a system relating several state variables. It depends only on the current equilibrium state of the system, but doesn't depend on the path by which the system arrived at its present state.

The 2nd law of thermodynamics is:

$$dS \geq \frac{\delta Q}{T} \quad (2.15)$$

For a reversible process, the equal sign in the 2nd law of thermodynamics is valid.

The infinitesimal amount of work done to the control volume is:

$$\delta W = PdV \quad (2.16)$$

As the next steps, we combine Eq. 2.14, 2.15 and 2.16, and then use the the definition of enthalpy Eq. 2.13. After the application of the ideal gas law and the definition of the heat capacity c_P , we have

$$\frac{c_P}{RT}dT = \frac{1}{P}dP \quad (2.17)$$

Now we integrate the equation above from gas state ‘in flow’ to state ‘out flow’ and take the relation $c_P/R_s = \gamma/(\gamma - 1)$ into account, the isentropic relation for pressure and temperature is then:

$$\boxed{\frac{P_{out}}{P_{in}} = \left(\frac{T_{out}}{T_{in}}\right)^{\frac{\gamma}{\gamma-1}}} \quad (2.18)$$

Apply the ideal gas law to the equation above, so that the isentropic relation for pressure and density is:

$$\boxed{\frac{P_{out}}{P_{in}} = \left(\frac{\rho_{out}}{\rho_{in}}\right)^{\gamma}} \quad (2.19)$$

For the special case that a flow has zero velocity at the outlet of the control volume in Fig. 2.1, there is the definition of stagnation enthalpy h_0 (intensive):

$$h_0 = h + \frac{1}{2}u^2 \quad (2.20)$$

For calorically perfect gas, Eq. 2.11 can be applied to the equation above, which can be further rearranged using Eq. 2.6 and Eq. 2.4. As a result, one can obtain a very practical equation for the calculation of the stagnation temperature by only using the specific heat ratio and Mach number, if the initial temperature is given:

$$\frac{T_0}{T} = 1 + \frac{\gamma - 1}{2}M^2 \quad (2.21)$$

Eq. 2.18 gives the relation between pressure ratio and temperature ratio for isentropic flow. Insert it into Eq. 2.21:

$$\frac{P_0}{P} = \left(\frac{T_0}{T}\right)^{\gamma/(\gamma-1)} = \left(1 + \frac{\gamma - 1}{2}M^2\right)^{\gamma/(\gamma-1)} \quad (2.22)$$

To derive the stagnation density, one can combine the ideal gas law with the expression for stagnation temperature and stagnation pressure. Thus, the stagnation density has

the expression:

$$\frac{\rho_0}{\rho} = \left(1 + \frac{\gamma - 1}{2} M^2\right)^{1/(\gamma-1)} \quad (2.23)$$

The isentropic and stagnation flow relations stated in this section are very useful. If how one thermodynamic quantity varies across an isentropic process is known, one can immediately tell how a second thermodynamic quantity varies. For example, a flow being stagnated against a test object, there is a little pressure tapping on front of that object and one measures what the pressure becomes when it's stagnated against the front of the object. Because the ambient temperature and pressure are known, one can immediately be able to figure out what the temperature of the flow is as well.

2.1.3 Mass, momentum and energy conservation

The most basic tools in fluid mechanics are the equations of mass, momentum and energy conservation. They are applied to do control volume analysis for shock flows. Standard textbooks in fluid mechanics have provided the conservation equations in differential or integral forms. The idea of mass and momentum conservation in fluid mechanics evolved mainly through the work of Newton (the second book of his *Principia*), d'Alembert, Bernoulli and Euler. The modern forms of these two equations are developed by Euler during the mid-18th century in St. Petersburg and Berlin [32]. The energy conservation equation is reported later and has the roots in the development of thermodynamics. But who developed the modern form of the energy conservation equation is obscure due to the rapid development of physical science in the nineteenth century [32].

This section considers a control volume, which is placed in an one-dimensional flow from right to left in Fig. 2.1.

The equation for the conservation of mass is also named as continuity equation. In plain text for the simplest case such as Fig. 2.1 (without mass accumulation on the wall), the continuity equation is: mass flow rate input = mass flow rate output. It shall be remarked that mass flow rate has the unit of kg/s, which is not mass flux with the unit of kg/(m²s).

This corresponding equation in mathematical language is [42]:

$$\dot{m}_{in} = \dot{m}_{out} \quad (2.24)$$

with mass flow rate \dot{m} .

The continuity equation for this simple 1D steady flow is thus:

$$\Rightarrow \boxed{\rho_{in} u_{in} A_{in} = \rho_{out} u_{out} A_{out}} \quad (2.25)$$

with density ρ and area A .

The differential form (also for general cases) of the continuity equation is [32]:

$$\frac{\partial \rho}{\partial t} + \nabla(\rho \vec{u}) = 0 \quad (2.26)$$

The momentum conservation in plain text is: total forces = rate of momentum change = rate of momentum output - rate of momentum input.

For the small control volume, there is:

$$F = \frac{d(mu)}{dt} = \frac{\Delta(mu)}{\Delta t} = \frac{m_{out}u_{out} - m_{in}u_{in}}{\Delta t} = \frac{\rho_{out}u_{out}A\Delta t \cdot u_{out} - \rho_{in}u_{in}A\Delta t \cdot u_{in}}{\Delta t} \quad (2.27)$$

The total force on the control volume is $F = P_{in}A_{in} - P_{out}A_{out}$ for inviscid flow. The momentum conservation equation for inviscid flow can thus be derived from the equation above (such as in [42]):

$$\boxed{P_{in}A_{in} - P_{out}A_{out} = \rho_{out}A_{out}u_{out}^2 - \rho_{in}A_{in}u_{in}^2} \quad (2.28)$$

One shall pay attention to the sign of the force. In general, the flow direction indicates the positive sign. The force from outside on the inlet area A_{in} has the same direction as the flow, therefore $P_{in}A_{in}$ has the positive sign. Same logic, $P_{out}A_{out}$ has thus the negative sign. One can notice that, the equation of momentum conservation is actually the Newton's second law applied for a control volume instead of an object.

The differential form of the momentum conservation equation for inviscid flow is [32]:

$$\frac{\partial(\rho u)}{\partial t} + \nabla(\rho u_x \vec{u}) = -\frac{\partial P}{\partial x} + \rho f_x \quad (2.29)$$

with body force per mass flow rate f . The gravitational force term is neglected. The differential form of the momentum conservation equation for viscous flow has to be individually discussed for different types of flows. For micro shock flows, [10] provides the details.

The energy conservation in plain text is: heat transfer + work = energy output - energy input

The energy conservation equation is [44]:

$$Q + W = \dot{m}(u_{i,out} + \frac{P_{out}}{\rho_{out}} + \frac{u_{out}^2}{2} + gz_{out}) - \dot{m}(u_{i,in} + \frac{P_{in}}{\rho_{in}} + \frac{u_{in}^2}{2} + gz_{in}) \quad (2.30)$$

with total heat flow rate Q (with the unit J/s, not heat flux with J/(m²s)), total work rate W (with the unit Nm/s), internal energy \mathbb{U}_i per unit mass (the energy of the random molecular motion), height z and gravitational constant g .

In case that this is an adiabatic and inviscid flow, and gravitation doesn't change between the inlet and outlet, the energy equation can be written by using the definition of the enthalpy:

$$\boxed{\dot{m}(h_{out} + \frac{u_{out}^2}{2}) = \dot{m}(h_{in} + \frac{u_{in}^2}{2})} \quad (2.31)$$

The term $u^2/2$ is the energy per unit mass flow rate of the ordered molecular motion, which is normally called the kinetic energy.

The energy conservation equation for an adiabatic flow can also be written in the differential form [32]:

$$-\nabla(P\vec{u}) + \rho(\vec{f}\vec{u}) = \frac{\partial}{\partial t} \left[\rho \left(\mathbb{U}_i + \frac{u^2}{2} \right) \right] + \nabla \left[\rho \left(\mathbb{U}_i + \frac{u^2}{2} \right) \vec{u} \right] \quad (2.32)$$

2.1.4 Flow with wall friction and heat conduction

The objective of this sections is to consider a tube flow with diffusive transport phenomena due to wall friction and heat conduction. It is already stated at the beginning of the thesis that by micro flows, wall friction and heat conduction become non-negligible. This leads to fundamental difference between a micro and a macro shock wave, since the propagation of a macro shock wave is conventionally treated as inviscid and adiabatic. Logically, for the micro shock wave a wall friction term shall be now introduced into the momentum conservation equation. A wall heat conduction term shall also be considered in the energy conservation equation. This brings us the key question of this section: **How can we calculate the wall friction and heat conduction terms of a tube flow?** These questions shall be answered as follows.

First of all, we start with considering a control volume ‘CV’ in the tube shown in Fig. 2.2. The frictional effect is modeled as shear stress at the wall acting on the control volume. A shock wave is not included in the control volume at this stage of the thesis, so that the flow property changes induced by wall friction and heat conduction can be separately considered. Furthermore, we assume that the flow propagates only in the axial direction (not in the vertical direction), so that a quasi 1D flow occurs. It is called ‘quasi’ due to the area where the friction force works on, shall be two dimensionally calculated.

The hydraulic diameter D in Fig. 2.2 is a commonly used term when handling flow in non-circular tubes and channels. Using this term, one can calculate for different tubes in the same way as for a round tube. Specially for a rectangular tube, D is well known as:

$$D = \frac{2ab}{a + b} \quad (2.33)$$

with a and b as the width and height, respectively.

The hydraulic cross-sectional area of a tube is thus:

$$A_h = \frac{\pi D^2}{4} \quad (2.34)$$

The friction force between the wall and the flow in the control volume equals to the shear stress τ multiplied by the control volume’s wall surface A_f (f for friction), which is not A_h .

In general case, the shear stress is [32]:

$$\tau = f \frac{1}{2} \rho u^2 \quad (2.35)$$

f is friction coefficient.

It shall be remarked that in case of a Newtonian fluid (a fluid in which the viscous

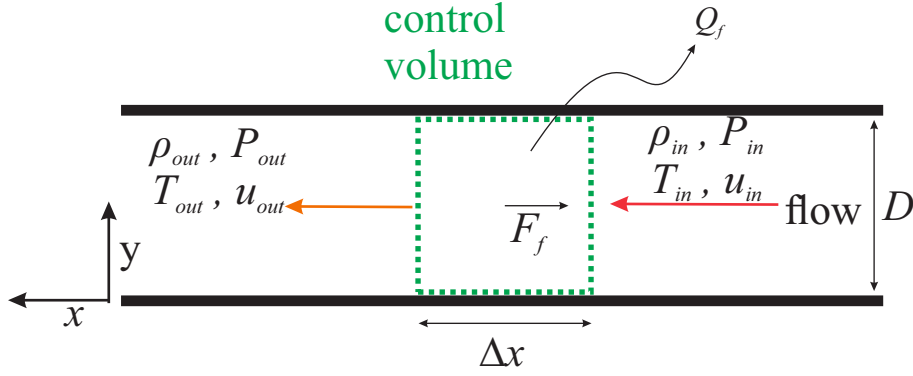


Figure 2.2: A control volume in a tube for studying wall friction and heat conduction. A shock wave is not in this control volume.

stresses arising from its flow are linearly proportional to the local shear strain rate), the shear stress is related with the shear strain rate du/dy by the relation $\tau = \mu \frac{du}{dy}$ (for a fix position x). The Newtonian fluid assumption will be very useful in later sections. But in order not to lose the generosity, we start with the general case in Eq. 2.35 for this part of the thesis. The friction force on the control volume with the length Δx can be denoted as F_f (indicating a small element), thus:

$$F_f = \tau \cdot A_f = \left(f \frac{1}{2} \rho u^2\right) \cdot (\pi D \Delta x) \quad (2.36)$$

with

$$A_f = \pi D L_f \quad (2.37)$$

As stated in section 2.1.3, the momentum conservation for the control volume means that total forces = rate of momentum change:

$$P_{in} A_h - P_{out} A_h - F_f = \rho_{out} A_h u_{out}^2 - \rho_{in} A_h u_{in}^2 \quad (2.38)$$

Now we insert Eq. 2.34 and 2.36 into the equation above. After simple algebraic rearrangements, there is:

$$\boxed{-\frac{2f\rho u^2 \cdot \Delta x}{D} = (P_{out} + \rho_{out} u_{out}^2) - (P_{in} + \rho_{in} u_{in}^2)} \quad (2.39)$$

The equation above is thus the momentum equation, which has the wall friction term as the left-hand side of the equation. This first step to answer the question from the very beginning of this section is done.

Now, we deal with the wall heat conduction. In this project, there is no external source for heat addition. Actually the heat is transferred out from the flow to the tube walls. Therefore, it is a cooling process. It is thus logical that we shall focus on studying the cooling process in this part of the thesis.

The energy conservation for the control volume means that: heat conduction + work = energy output - energy input. Therefore, the energy conservation equation for the control volume can be formulated as:

$$\mathbb{Q}_f + W_f = (h_{out} + \frac{1}{2}u_{out}^2) - (h_{in} + \frac{1}{2}u_{in}^2) \quad (2.40)$$

Wall heat conduction per mass flow rate is \mathbb{Q}_f with the unit J/kg, while friction work per mass flow rate is W_f with the unit N·m/kg. The equation above is thus the energy equation containing the wall heat conduction term. The flow only with wall friction or only with wall heat conduction are called Fanno or Rayleigh flow, correspondingly. Further discussions on these flows are to be found in textbooks e.g. [32].

By definition, \mathbb{Q}_f is:

$$\mathbb{Q}_f = \frac{Q}{\dot{m}} \quad (2.41)$$

Q is the total heat flow rate with the unit Watt. \mathbb{Q}_f thus has the unit W/(kg·s⁻¹) or simply J/kg. The heat flux q is by definition the total heat flow rate divided by the heat conduction surface, i.e. the wall surface A_f . Thus q is:

$$q = \frac{Q}{A_f} \quad (2.42)$$

q has the unit W/m².

The mass flow rate across the cross-section of the control volume is:

$$\dot{m} = \rho_{out}A_h u_{out} = \rho_{in}A_h u_{in} = \rho_{in}(\pi D^2/4)u_{in} \quad (2.43)$$

Apply the Fourier's law for thermal conduction:

$$q = -k \frac{dT}{dy} = -k \frac{T_{mid}(x) - T_{wall}}{D/2} \quad (2.44)$$

with thermal conductivity k , temperature in the tube middle $T_{mid}(x)$ and temperature at the tube wall T_{wall} . The negative sign indicates that heat flux moves from the higher temperature region to the lower temperature region.

Derive from Eq. 2.37, Eq. 2.41, 2.42, 2.43 and 2.44, \mathbb{Q}_f can be brought to the form:

$$\mathbb{Q}_f = \frac{q \cdot A_f}{\dot{m}} = \left(-k \frac{T_{mid}(x) - T_{wall}}{D/2}\right)(\pi D L_f) \frac{1}{\rho_{in} \pi (D^2/4) u_{in}} = -\frac{8 L_f k (T_{mid}(x) - T_{wall})}{\rho_{in} D^2 u_{in}} \quad (2.45)$$

Under the no-slip assumption that leads to $W_f = 0$, the energy conservation equation

in Eq. 2.40 can be brought to the form as:

$$\boxed{-\frac{8L_f k(T_{mid}(x) - T_{wall})}{\rho_{in} D^2 u_{in}} = (h_{out} + \frac{1}{2}u_{out}^2) - (h_{in} + \frac{1}{2}u_{in}^2)} \quad (2.46)$$

The wall heat conduction term is the left-hand side of the equation above.

Notice that, $\mathbb{Q}_f \propto 1/D^2$. A smaller hydraulic diameter D corresponds to a dramatic increase in wall heat conduction term \mathbb{Q}_f . As an example, we compare the flow in a 100 μm diameter tube and a 1 mm tube. Their diameter ratio is just 10, but \mathbb{Q}_f of the smaller tube is 100 times as big as the larger tube.

2.1.5 Navier-Stokes equation

The Navier-Stokes equation is among the most important equations in fluid mechanics. Here without going into details, the Navier-Stokes equation is derived from Newton's second law which is actually the momentum equation as already mentioned in section 2.1.3. In short, the Navier-Stokes equation is the momentum equation for an unsteady viscous Newtonian fluid.

For incompressible fluid i.e. $\nabla \cdot \vec{u} = 0$ (equivalent as the material derivative $D\rho/Dt = 0$), the Navier-Stokes equation is [45]:

$$\frac{\partial \vec{u}}{\partial t} + (\vec{u} \cdot \nabla) \vec{u} = -\frac{1}{\rho} \nabla P + \frac{\mu}{\rho} \nabla^2 \vec{u} \quad (2.47)$$

For compressible fluid i.e. $\nabla \cdot \vec{u} \neq 0$, the Navier-Stokes equation is [45]:

$$\frac{\partial \vec{u}}{\partial t} + (\vec{u} \cdot \nabla) \vec{u} = -\frac{1}{\rho} \nabla P + \frac{\mu}{\rho} \nabla^2 \vec{u} + \frac{1}{3} \mu \nabla (\nabla \cdot \vec{u}) \quad (2.48)$$

Shock flows are compressible flows. Therefore, the compressible form of the Navier-Stokes equation is of central interest in this thesis. Together with supplemental equations e.g. conservation of mass and boundary conditions, the Navier-Stokes equations can be applied to model fluid motion. At very small scales or very low pressure, real fluids made of discrete molecules will produce results deviating from the continuous fluids modeled by the Navier-Stokes equations. For fluid with large Knudsen number, the Boltzmann equation may be a suitable replacement. Failing that, one may have to resort to molecular dynamics or various hybrid methods. The detailed discussion of the Knudsen number and the related governing physics is made in section 2.2.4.

2.2 Shock wave theory

This section presents the relevant fundamental theory of shock wave.

2.2.1 Rankine-Hugoniot relations

How do the gas properties change across the shock wave? If we know one parameter e.g. Mach number, how do we derive the other thermodynamical parameters of the gas? The questions can be answered by the Rankine-Hugoniot relations. The derivation of the Rankine-Hugoniot relations is explained here. This section is my interpretation of the work [42] and [32].

As indicated in Fig. 2.3, consider a control volume surrounding the shock wave with the gas coming from region 1 into region 2 crossing the fixed shock wave.

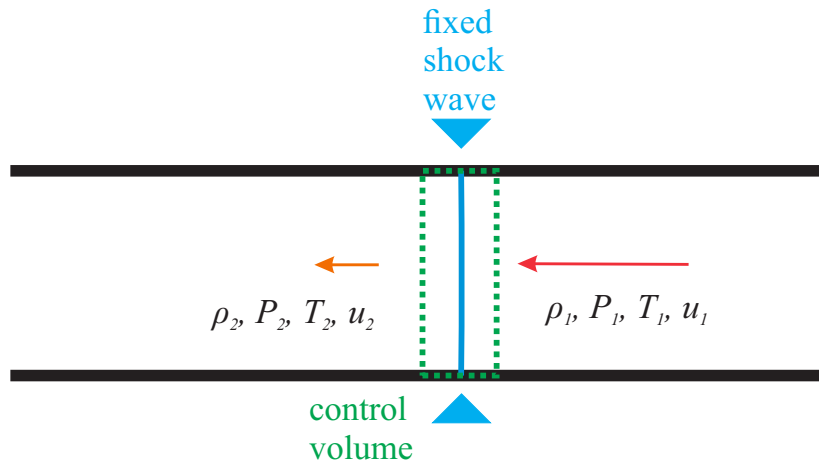


Figure 2.3: Illustration of gas propagating through a shock wave (shock-fixed reference frame).

It shall be remarked that, the subscript indicates the shock flow region e.g. u_1 is the gas flow velocity in region 1, which is upstream of the shock wave. In this section, the flow is considered as inviscid and adiabatic. Taking the conservation of mass into account, one can apply the continuity equation to the input A_1 and output A_2 surface of the control volume:

$$\rho_1 u_1 A_1 = \rho_2 u_2 A_2 \quad (2.49)$$

It means, the mass flow rate coming into the control volume is equal to the mass flow rate coming out $\dot{m}_1 = \dot{m}_2$.

Since the tube has constant cross-section, there is $A_1 = A_2$ which can simply be written as A_h with 'h' for hydraulic. The continuity equation can be further written as:

$$\boxed{\rho_1 u_1 = \rho_2 u_2} \quad (2.50)$$

Momentum conservation is essentially Newton's second law $F = d(m \cdot v)/dt$ in general form [46]. It means the rate of momentum change of a body, is directly proportional to the force applied.

Apply Newton's second law to the control volume:

$$F = \frac{d(mu)}{dt} = \frac{\rho_2 A u_2 dt \cdot u_2 - \rho_1 A u_1 dt \cdot u_1}{dt} = \rho_2 A u_2^2 - \rho_1 A u_1^2 \quad (2.51)$$

So, the total force acting on the control volume is $P_1 A_h - P_2 A_h$.

After simplification, the equation for the momentum conservation of the control volume is:

$$P_1 A_h - P_2 A_h = \rho_2 A_h u_2^2 - \rho_1 A_h u_1^2 \quad (2.52)$$

$$\Rightarrow \boxed{P_1 - P_2 = \rho_2 u_2^2 - \rho_1 u_1^2} \quad (2.53)$$

Rearrange Eq. 2.53:

$$\frac{P_2}{P_1} - 1 = \frac{\rho_1 u_1^2}{P_1} - \frac{\rho_2 u_2^2}{P_2} \quad (2.54)$$

$$\Rightarrow \frac{P_2}{P_1} - 1 = \frac{\gamma \rho_1 u_1^2}{\gamma P_1} \left(1 - \frac{\rho_2 u_2 u_2}{\rho_1 u_1 u_1}\right) \quad (2.55)$$

Apply the sound velocity equation $u_a = \sqrt{\gamma R T} = \sqrt{\gamma P / \rho}$ and conservation of mass to simplify the equation above, we can achieve the pressure ratio from the momentum conservation:

$$\Rightarrow \frac{P_2}{P_1} = 1 + \gamma M_1^2 \left(1 - \frac{\rho_1}{\rho_2}\right) \quad (2.56)$$

Now, we turn to the energy conservation equation:

$$\boxed{h_1 + \frac{u_1^2}{2} = h_2 + \frac{u_2^2}{2}} \quad (2.57)$$

The mass flow rate on both sides of the equation is dropped due to the mass conservation. The gravity terms are also canceled, since the flow goes horizontally. The stagnation or total enthalpy coming into the control volume $h_1 + \frac{u_1^2}{2}$ must equal to the total enthalpy leaving $h_2 + \frac{u_2^2}{2}$. Rankine and Hugoniot made the assumption that the gas is calorically perfect. It means that 1. the ideal gas law applies $P = \rho R_s T$; 2. the specific heat constant C_P and C_V don't change.

Insert $h = c_P T$ into Eq. 2.57:

$$c_P T_1 + \frac{u_1^2}{2} = c_P T_2 + \frac{u_2^2}{2} \quad (2.58)$$

$$\Rightarrow \frac{T_2}{T_1} = 1 + \frac{u_1^2}{2c_P T_1} - \frac{u_2^2}{2c_P T_1} \quad (2.59)$$

Again apply the equations of sound velocity and conservation of mass into the equation above. Also, apply the well known relation between the specific heat capacity with gas constant R_s , which is $c_P = R_s \gamma / (\gamma - 1)$.

$$\Rightarrow \frac{T_2}{T_1} = 1 + \frac{u_1^2}{2c_P T_1} \left(1 - \frac{u_2^2}{u_1^2}\right) \quad (2.60)$$

$$\Rightarrow \frac{T_2}{T_1} = 1 + \frac{\gamma - 1}{2} M_1^2 \left(1 - \left(\frac{\rho_1}{\rho_2}\right)^2\right) \quad (2.61)$$

Apply the ideal gas law to the equation above:

$$\frac{T_2}{T_1} = \frac{P_2 \rho_1}{P_1 \rho_2} = 1 + \frac{\gamma - 1}{2} M_1^2 \left(1 - \left(\frac{\rho_1}{\rho_2}\right)^2\right) \quad (2.62)$$

Rearrange the equation above, one can thus also achieve the pressure ratio from the energy conservation:

$$\frac{P_2}{P_1} = \left(1 + \frac{\gamma - 1}{2} M_1^2 \left(1 - \left(\frac{\rho_1}{\rho_2}\right)^2\right)\right) \frac{\rho_2}{\rho_1} \quad (2.63)$$

Since the momentum and energy conservation shall deliver the same pressure ratio, one can Equate Eq. 2.56 and 2.63:

$$1 + \gamma M_1^2 \left(1 - \frac{\rho_1}{\rho_2}\right) = \left(1 + \frac{\gamma - 1}{2} M_1^2 \left(1 - \left(\frac{\rho_1}{\rho_2}\right)^2\right)\right) \frac{\rho_2}{\rho_1} \quad (2.64)$$

When one solves for $\frac{\rho_1}{\rho_2}$ from the equation above, there are two solutions. But one of the solutions is $\rho_1 = \rho_2$, which is trivial. The other solution gives the Rankine-Hugoniot relation for density ratio across the shock [32]:

$$\boxed{\frac{\rho_2}{\rho_1} = \frac{(\gamma + 1)M_1^2}{2 + (\gamma - 1)M_1^2}} \quad (2.65)$$

Insert Eq. 2.65 into Eq. 2.56, there is the Rankine-Hugoniot relation for static pressure ratio across the shock [32]:

$$\boxed{\frac{P_2}{P_1} = \frac{2\gamma M_1^2 - \gamma + 1}{\gamma + 1}} \quad (2.66)$$

Insert Eq. 2.65 into Eq. 2.61, there is the Rankine-Hugoniot relation for temperature ratio [32]:

$$\boxed{\frac{T_2}{T_1} = \frac{(2\gamma M_1^2 - \gamma + 1)[2 + (\gamma - 1)M_1^2]}{(\gamma + 1)^2 M_1^2}} \quad (2.67)$$

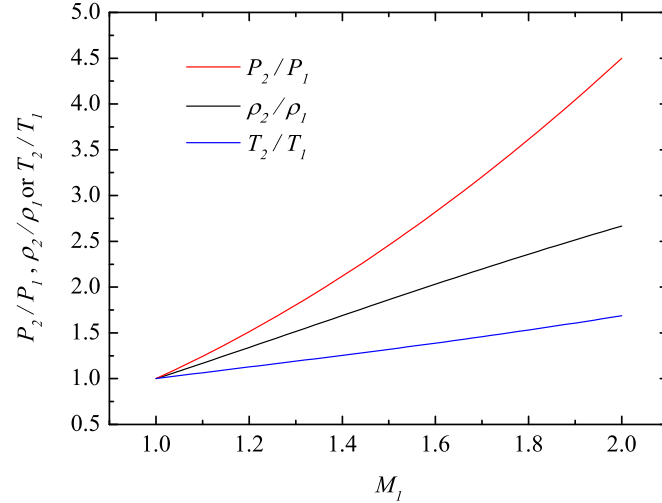


Figure 2.4: Change of gas properties across the shock wave.

The Mach number downstream of the shock can also be obtained by inserting Eq. 2.65 into the continuity equation [32]:

$$M_2 = \sqrt{\frac{2 + (\gamma - 1)M_1^2}{2\gamma M_1^2 - \gamma + 1}} \quad (2.68)$$

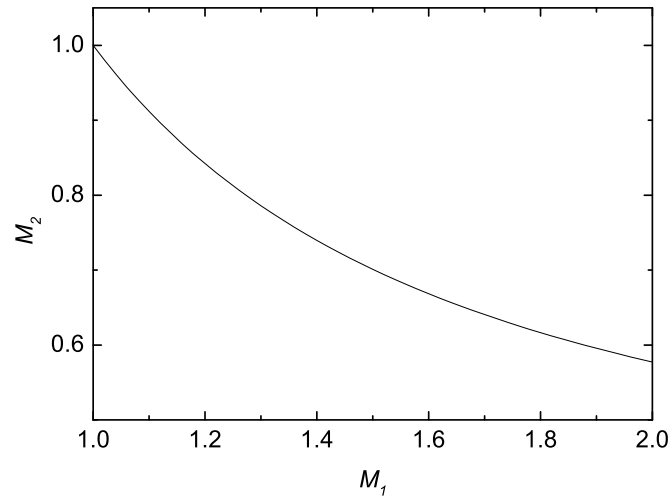


Figure 2.5: Theoretical flow Mach number behind the shock wave.

Specially interesting for this work is the density ratio ρ_2/ρ_1 depending on the Mach number of the shock wave M_s , which has the same value as M_1 (notation difference due to different reference frames). In the experimental section, ρ_2/ρ_1 and M_s are measured independently. Therefore, this relation can be experimentally investigated, also for

micro scale shock waves.

In Fig. 2.4 and 2.5, the Rankine-Hugoniot relations are plotted using relevant parameters for the experiments presented later in this thesis, namely: M_1 in the range of 1 to 2; $\gamma = 1.4$ for shock waves propagating in ambient air. From the theoretical curves, one can see the shock wave induced change in thermodynamic properties.

2.2.2 Physical properties in a shock tube

This section explains briefly the physical properties of the gas, i.e. pressure, density, temperature and velocity distribution inside an ideal shock tube. A conventional shock tube has the structure sketched in Fig. 2.6. The diaphragm separates a high pressure chamber and a low pressure chamber of the shock tube.

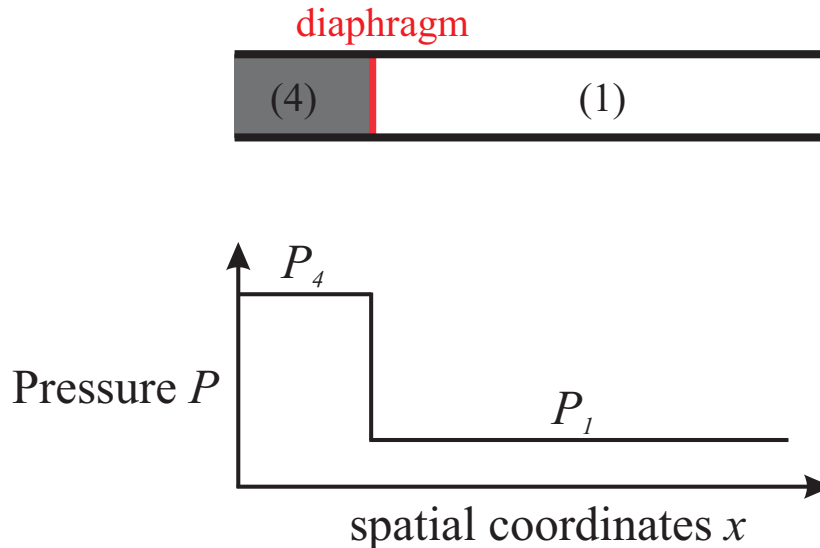


Figure 2.6: A conventional shock tube. The high pressure chamber is noted as region 4, while the low pressure chamber is noted as region 1.

Once the diaphragm ruptures, a series of compression waves starts propagating from the high pressure chamber into the low pressure chamber. Every compression wave increases the speed of sound behind it, because a compression wave ahead creates a hotter environment for the one behind. At the end, they catch up with the front running compression wave and combine into a sharp shock front. Simultaneously, a rarefaction wave, often referred to as the Prandtl-Meyer wave, travels back in to the driver gas. Fig. 2.7 is a snapshot of the shock tube at the time point, when a shock wave is fully developed.

The gas in front of the shock wave is in an undisturbed state (region 1). Behind the shock wave (region 2), the gas get compressed by the shock wave and brought into motion. The contact surface marks the separation between the driver (region 3) and test gases. The gases ahead and behind the contact surface have different values in density but the same value in pressure. The expansion fan divides the driver gas into the expansion-fan-processed area and the unprocessed area (region 4).

The relations ρ_2/ρ_1 , P_2/P_1 , T_2/T_1 and u_2/u_1 are already explained in section 2.2.1 as Rankine-Hugoniot relations. The other relations, e.g. ρ_3/ρ_2 , P_4/P_3 , are not the central point of this thesis. Those relations can be easily found in textbooks such as [33] and [32] under the key word ‘shock tubes’.

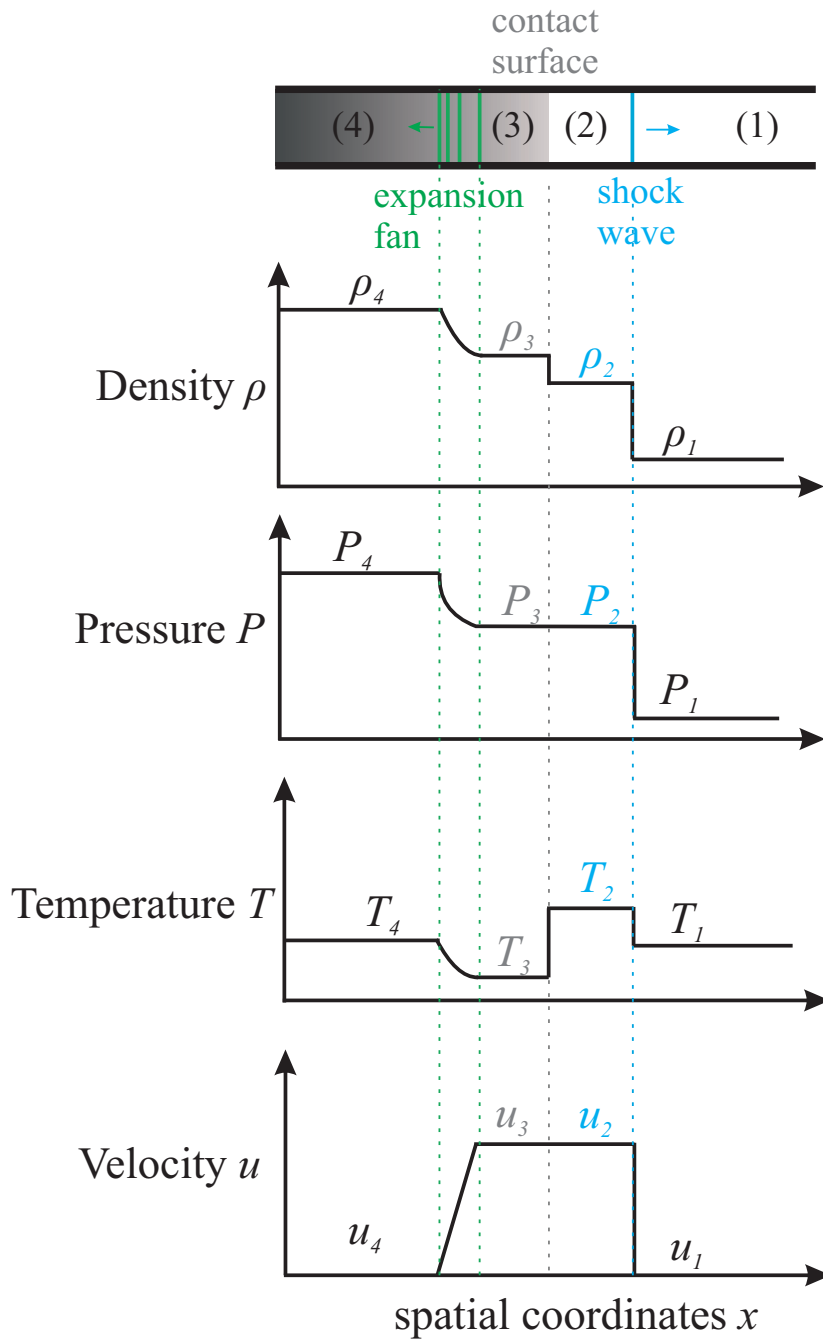


Figure 2.7: Snapshot of the distribution of density, pressure, temperature and velocity inside an ideal shock tube (lab frame reference). The sketch is based on shock tube theories in textbooks e.g. [33] and [32].

Here in Fig. 2.7, one can notice that across the contact surface there is $P_2 = P_3$ but $\rho_2 \neq \rho_3$ and $T_2 \neq T_3$. Therefore, if we want to detect the contact surface, we shall perform a density or temperature measurement. This is an important theoretical base for my thesis, because the contact surface alongside the shock wave are in the scope of the investigations.

Without going into all the mathematical details as in textbooks, the density and temperature between region 2 and region 3 can be explained as: The post-shock particles

closely behind the shock wave are compressed and ‘dragged’ into motion by the shock wave. On the other side, the contact surface is not ‘dragged’ by the shock wave, but rather ‘pushed’ by the expanding driver gas. These are two different mechanisms. Therefore, region 2 is hotter due to shock-compression, while the region 3 is colder due to gas expansion. The difference in temperature results in different density across the contact surface, because the corresponding pressure stays constant. The constant pressure across the contact surface can be proved by calculations involving the conservation of mass, momentum and energy.

2.2.3 Entropy growth associated with shock waves

This section discusses the entropy growth of the flow system associated with shock waves. The entropy growth is considered as a ‘loss’, which indicates a loss of the ability to extract work from the gas. In this section, it will be shown that entropy increases when a flow passes through a normal shock wave.

The theory of stagnation pressure will be used to calculate the entropy change. The stagnation pressure itself is derived from the equations of state and isentropic flow relations. Therefore, in order for the readers of this Ph.D thesis to understand this sub-chapter, previous sub-chapters shall be read first.

Recall the classical ‘definition’ of entropy (intensive) s :

$$ds = \frac{\delta q}{T} \quad (2.69)$$

dq is an incremental amount of heat added reversible to the system. At this point, one shall wonder that shock wave generation and propagation are not reversible, how can we use this equation to calculate the entropy change? Anderson [32] has written in his textbook: ‘entropy is a state variable, and it can be used in conjunction with any types of processes, reversible or irreversible. By irreversible process, an effective value of reversible heat δq can be assigned to relate the initial and the end states’.

Refer to Fig. 2.8 to make it clear that the shock wave is not an isentropic flow, but the stagnation process is.

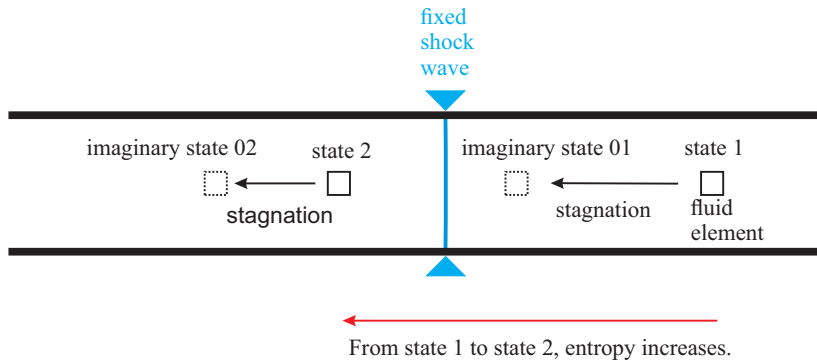


Figure 2.8: Illustration for shock wave induced entropy growth (shock-fixed reference frame).

As the approach described in [32]: From state 1 to imaginary state 01, the gas is brought to rest isentropically. The same process happens to state 2 and imaginary state 02.

The stagnation temperature is:

$$T_{01} = T_1 + \frac{1}{2c_P} u_1^2 \quad (2.70)$$

$$T_{02} = T_2 + \frac{1}{2c_P}u_2^2 \quad (2.71)$$

Apply the energy conservation Eq. 2.57 for the state 1 and state 2, there is:

$$h_1 + \frac{u_1^2}{2} = h_2 + \frac{u_2^2}{2} \quad (2.72)$$

For calorically perfect gas, the enthalpy is $h = c_P T$.

$$\Rightarrow c_P T_1 + \frac{u_1^2}{2} = c_P T_2 + \frac{u_2^2}{2} \quad (2.73)$$

$$\Rightarrow T_1 + \frac{u_1^2}{2c_P} = T_2 + \frac{u_2^2}{2c_P} \quad (2.74)$$

$$\Rightarrow T_{01} = T_{02} \quad (2.75)$$

As a result, the stagnation temperature doesn't change across the shock wave.

Now, the stagnation pressure shall be studied:

$$P_{01} = P_1 \left[1 + \frac{\gamma - 1}{2} M_1^2 \right]^{\gamma/(\gamma-1)} \quad (2.76)$$

$$P_{02} = P_2 \left[1 + \frac{\gamma - 1}{2} M_2^2 \right]^{\gamma/(\gamma-1)} \quad (2.77)$$

P_{02}/P_{01} is thus:

$$\frac{P_{02}}{P_{01}} = \frac{P_2 \left[1 + \frac{\gamma-1}{2} M_2^2 \right]^{\gamma/(\gamma-1)}}{P_1 \left[1 + \frac{\gamma-1}{2} M_1^2 \right]^{\gamma/(\gamma-1)}} \quad (2.78)$$

The functions $P_2/P_1 = f(M_1)$ and $M_2 = f(M_1)$ are given by Rankine-Hugoniot relations in Eq. 2.66 and 2.68, respectively.

$$\Rightarrow \frac{P_{02}}{P_{01}} = \left(\frac{(\gamma + 1)M_1^2}{2 + (\gamma - 1)M_1^2} \right)^{\gamma/(\gamma-1)} \left(\frac{\gamma + 1}{2\gamma M_1^2 - \gamma + 1} \right)^{\gamma/(\gamma-1)} \quad (2.79)$$

Derived from the definition of entropy in Eq. 2.69, there is a classical thermodynamic equation to calculate the entropy change from temperature and pressure. Apply it to the imaginary states 01 and 02 [32]:

$$s_{02} - s_{01} = c_P \cdot \ln\left(\frac{T_{02}}{T_{01}}\right) - R_s \cdot \ln\left(\frac{P_{02}}{P_{01}}\right) \quad (2.80)$$

Since state 1 to imaginary state 01 is isentropic, $S_{01} = S_1$. And $S_{02} = S_2$ is valid for

the same reason. The equation above becomes:

$$s_2 - s_1 = c_P \cdot \ln\left(\frac{T_{02}}{T_{01}}\right) - R_s \cdot \ln\left(\frac{P_{02}}{P_{01}}\right) \quad (2.81)$$

It is shown earlier that $T_{01} = T_{02}$, thus the temperature term is zero.

$$\Delta s = s_2 - s_1 = -R_s \cdot \ln\left(\frac{P_{02}}{P_{01}}\right) = -R_s \cdot \ln\left(\left(\frac{(\gamma + 1)M_1^2}{2 + (\gamma - 1)M_1^2}\right)^{\gamma/(\gamma-1)} \left(\frac{\gamma + 1}{2\gamma M_1^2 - \gamma + 1}\right)^{\gamma/(\gamma-1)}\right) \quad (2.82)$$

This equation gives the entropy change of the gas flow crossing the shock wave as a function of the Mach number M_1 along (assume γ known). Once again, the Mach number proves to be a very useful parameter which can be used to calculate many other thermodynamic properties. In Fig. 2.9 the change of entropy of the gas is plotted as a function of the Mach number M_1 according to Eq. 2.82. The Mach number in the experiments of this thesis is between 1 and 2. M_1 below 1 is also plotted in this figure to illustrate that, a shock wave (or say, the gas flow ahead the shock in the shock-fixed reference frame) can not be slower than sound velocity. If a shock wave was slower than a sound wave, it would lead to violation of the 2nd law of thermodynamics, which says the entropy of an isolated system must grow or stay constant.

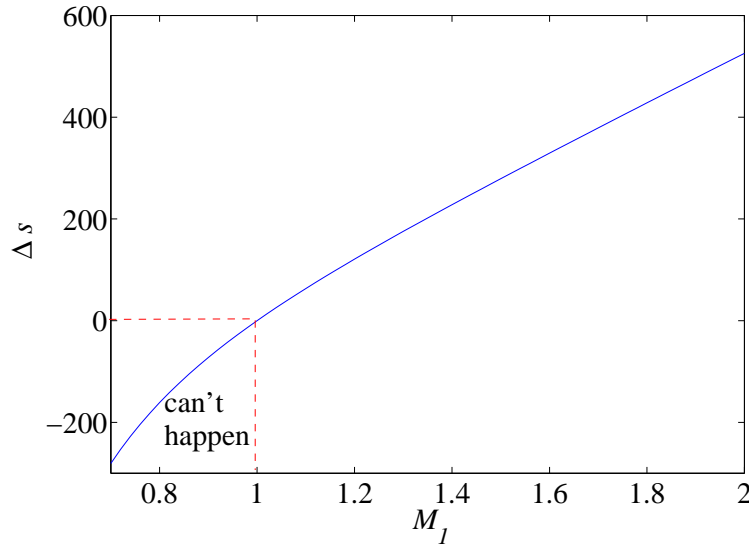


Figure 2.9: Shock wave induced theoretical entropy change as a function of the Mach number.

The higher is M_1 , the bigger is the entropy growth. Therefore, the gas has less capability to do work, when a stronger shock wave has propagated through this gas. For micro shock waves with a low Mach number, the shock wave attenuation is strong, meaning the absolute propagation length is small (mm range shown by experiments). Thus, the loss is small. As for the application side of view, for example in aerospace

industry, it is important to minimize the strength of any shock waves in the engine, so that we can have more opportunity to extract work from the gas.

The discussion of entropy in this section contributes to later experiments (specially relevant to section 5.5) in this project. This section gives a important information that a shock wave must always have supersonic velocity.

2.2.4 Knudsen number

In the frame of continuum mechanics, a subject is modeled as infinitely divisible rather than as discrete particles. Modeling objects in this way ignores the fact that matter is made of atoms, so that it is not continuous in reality. However, if the scale of the subject is much greater than the inter-atomic distance, continuum mechanics is appropriate. Fundamental physical laws such as the conservation of mass, the conservation of momentum, and the conservation of energy can be applied in the case of continuum mechanics.

Therefore, one would naturally ask: when does the continuum mechanics apply? This section shall clarify the question. This answer to the question is very important because a flow in a micro tube may not always fulfill the precondition for applying continuum mechanics i.e. the characteristic scale of the flow may not be sufficiently larger than the inter-atomic distance.

In order to answer the question, the so-called Knudsen number Kn shall be introduced and discussed here. Kn helps to determine whether continuum mechanics or molecular physics should be applied to model a flow. Kn can be formulated as (taken from [47]):

$$Kn = \frac{\Lambda}{D} = \sqrt{\frac{\pi\gamma}{2}} \frac{M}{Re} \quad (2.83)$$

with collisional mean free path Λ , hydraulic diameter D , heat capacity ratio γ , Mach number M and Reynolds number Re .

The mean free path Λ can be calculated as:

$$\Lambda = \frac{k_B T}{\sqrt{2} P \pi \sigma^2} \quad (2.84)$$

with Boltzmann constant k_B and molecular diameter σ . $\Lambda \approx 68$ nm for ambient air [23].

Shock wave thickness D_s is related to Λ through the relation [10]:

$$\frac{D_s}{\Lambda} \approx \frac{12\gamma}{\gamma + 1} \frac{P_1}{P_2 - P_1} \quad (2.85)$$

with P_2 and P_1 as the pressure behind and ahead the shock wave, correspondingly. For a shock wave propagating in ambient air with $\gamma = 1.4$, $P_1 = 1$ bar, $M_1 = 1.3$ (typical in this project) and $P_2/P_1 \approx 1.75$ (read from Fig. 2.4 for this Mach number), there is $D_s \approx 600$ nm calculated from Eq. 2.85.

Fig. 2.10 shows different Knudsen number ranges with the corresponding governing physics. Molecular physics may (doesn't have to) be applied for all ranges of Kn , but this would cause enormous amount of calculation for a macroscopic flow with very small Kn (low Kn corresponds to large D if Λ stays constant, see Eq. 2.83). Rarefied fluid flows are encountered in small geometries or in low-pressure situations. Kn of

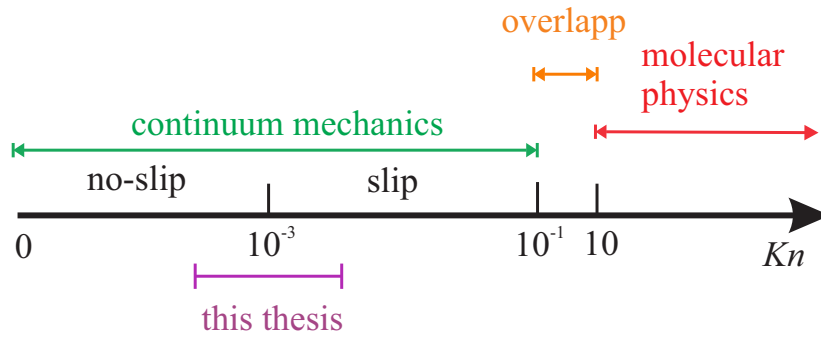


Figure 2.10: Knudsen number ranges of a fluid flow. Kn ranges are defined in [47].

the particular flow determines the degree of rarefaction and the degree of validity of the continuum model. The different Knudsen number regimes are actually determined empirically, while the pioneer experiments in rarefied gas dynamics were conducted by Knudsen [48].

From the findings of Knudsen and later works (summarized in the review article [47]), the Knudsen number regimes can be listed as follows.

1. $Kn \approx 0$: Euler equations can be applied. Here the transport diffusive terms (terms regarding the wall friction and heat conduction) in the momentum and energy equations are negligible, thus the Navier–Stokes equations reduce to the inviscid Euler equations.
2. $Kn < 10^{-3}$: Navier-Stokes with no-slip conditions can be applied. No-slip conditions indicate that the flow velocity at the boundary (e.g. tube wall) is zero.
3. $10^{-3} < Kn < 10^{-1}$: Navier-Stokes with slip conditions can be applied. In contrast to no-slip conditions, here the flow velocity at the boundary is not zero.
4. $Kn > 10$: Molecular physics shall be applied. The corresponding models can be deterministic (e.g. MD - Molecular Dynamics) or statistic (e.g. Boltzmann equation, DSMC - Direct Simulation Monte Carlo).

In the experiments of this thesis, the corresponding Kn calculated from Eq. 2.83 is around $3.4 \cdot 10^{-4}$ in the case of the shock flow in the capillary with $D = 200 \mu\text{m}$, or $1.36 \cdot 10^{-3}$ in the case of $D = 50 \mu\text{m}$ (the smallest capillary in this project). This clear takeaway from the discussion on Kn in this section is that our Kn is sufficiently far away from zero, thus the wall friction and heat conduction cannot be neglected. Moreover, slip conditions may apply.

2.3 Gaussian optics

Gaussian optics is applied to calculate the laser focus dimensions, which are important for e.g. evaluating the optical breakdown process in the later sections. Therefore, the related theory from [49], [50] and [51] is summarized and briefly explained in this section of the thesis.

It is well known that light as an electromagnetic wave can be described by the Maxwell equations system. The so-called wave equation (here consider the electrical field) can be derived from this equations system:

$$\left(\frac{\partial^2}{\partial x^2} + \frac{\partial^2}{\partial y^2} + \frac{\partial^2}{\partial z^2} - \frac{1}{c^2} \frac{\partial^2}{\partial t^2}\right)E(x, y, z, t) = 0 \quad (2.86)$$

One of the solutions of the wave equation is the plane wave:

$$E(z, t) = E_0 e^{-i(kz - \omega t)} \quad (2.87)$$

An another solution is the spherical wave:

$$E(r, t) = \frac{A}{r} e^{-i(kr - \omega t)} \quad (2.88)$$

with $r = \sqrt{x^2 + y^2 + z^2}$ and A as a constant.

A plane wave is infinitely wide stretched. A spherical wave propagates in all directions. These two solutions can't directly describe the TEM₀₀ laser beam, which has a certain propagation direction and a finite beam width. TEM₀₀ is the fundamental transverse mode of the laser resonator and has the same form as a Gaussian beam. But by applying the paraxial approximation to the spherical wave solution, a description of the laser beam can be made [49]:

$$E(r, z, t) = \frac{B}{q} e^{-\frac{r^2}{w^2(z)}} e^{-i\frac{kr^2}{2R(z)}} e^{i(\omega t - kz)} \quad (2.89)$$

with $q = z + iz_R$, $r = \sqrt{x^2 + y^2}$ and $B = Ae^{kz_R}$. $w(z)$ is the laser beam $1/e^2$ -radius and $R(z)$ is the curvature radius. In Fig. 2.11, geometrical and Gaussian optics are illustrated. Eq. 2.89 is an approximated solution of the wave equation near the optical axis, which is the gaussian beam. It describes the propagation of the TEM₀₀ mode.

The definition of the beam quality factor M_q^2 is [49]:

$$M_q^2 = w_0 \theta \frac{\pi}{\lambda} \quad (2.90)$$

θ is the divergence angle of the laser beam. Far away from the focus point, the beam radius has asymptotically linear relation with the distance z in optical axis. θ can be

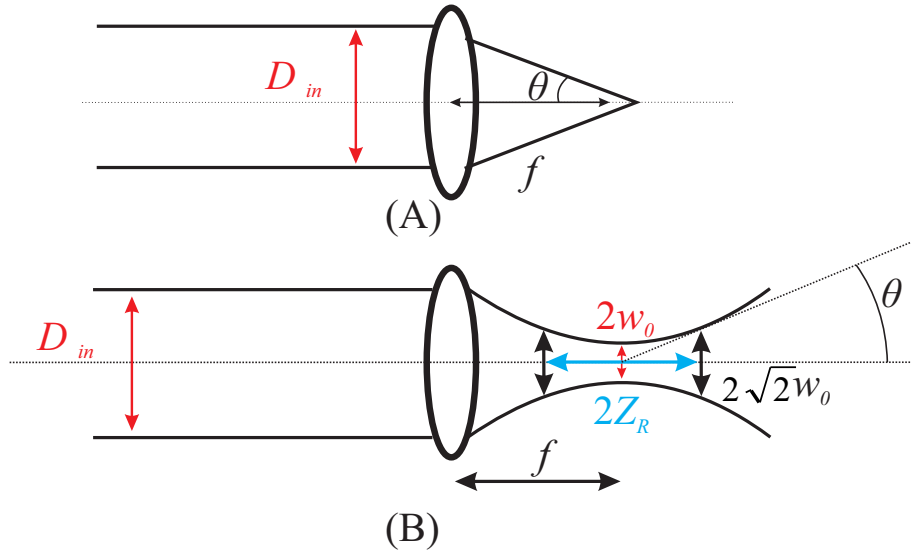


Figure 2.11: Illustration (A) geometrical optics (B) Gaussian beam. If there isn't a specific note, the radius and diameter are the $1/e^2$ -radius and $1/e^2$ -diameter, respectively.

calculated as [49]:

$$\theta = \frac{w_0}{Z_R} \quad (2.91)$$

Z_R is the Rayleigh length is the distance along the propagation direction of a beam from the waist to the place where the area of the cross section is doubled.

The geometrical approximation for θ is [49]:

$$\theta \approx \frac{D_{in}/2}{f} \quad (2.92)$$

Insert Eq. 2.92 into Eq. 2.90, one can obtain the focus radius/diameter [49]:

$$D_0 = 2w_0 = M_q^2 \frac{4f\lambda}{\pi D_{in}} \quad (2.93)$$

In case $M_q^2 = 1$, the equation above becomes the same as stated in [49]. Combine Eq. 2.91, Eq. 2.91 and Eq. 2.93, one can achieve the Rayleigh length [49]:

$$z_R = \frac{4\lambda f^2 M_q^2}{D_{in}^2 \pi} \quad (2.94)$$

The FWHM intensity of a laser pulse can be calculated as [49]:

$$I_{FWHM} \approx \frac{0.4 \cdot E}{\tau_{FWHM}(\pi/4) D_{FWHM}^2} \quad (2.95)$$

with

$$D_{FWHM} = D_0 \sqrt{\frac{\ln(2)}{2}} \quad (2.96)$$

τ_{FWHM} and D_{FWHM} are the laser pulse FWHM-duration and FWHM-diameter, respectively. D_0 is the $1/e^2$ -diameter. The factor 0.4 comes from 3D Gaussian distribution, meaning 40% of the laser pulse energy is encircled within the FWHM range. In this work, I_{FWHM} is a very important parameter, since the optical breakdown process occurs intensively during the FWHM range. The following plasma and shock wave generation depend on the breakdown process. Therefore later in the experimental part of the thesis, I_{FWHM} is frequently used.

The peak intensity I_{peak} is interesting for the study of the breakdown or ablation threshold. In the following part, it is presented how to calculate I_{peak} .

Peak intensity I_{peak} calculation:

To make the analysis more clear, a 3D illustration of a gaussian laser pulse is presented in Fig. 2.12. It can obviously be seen that, the temporal and spatial peak of the laser pulse corresponds to the peak intensity.

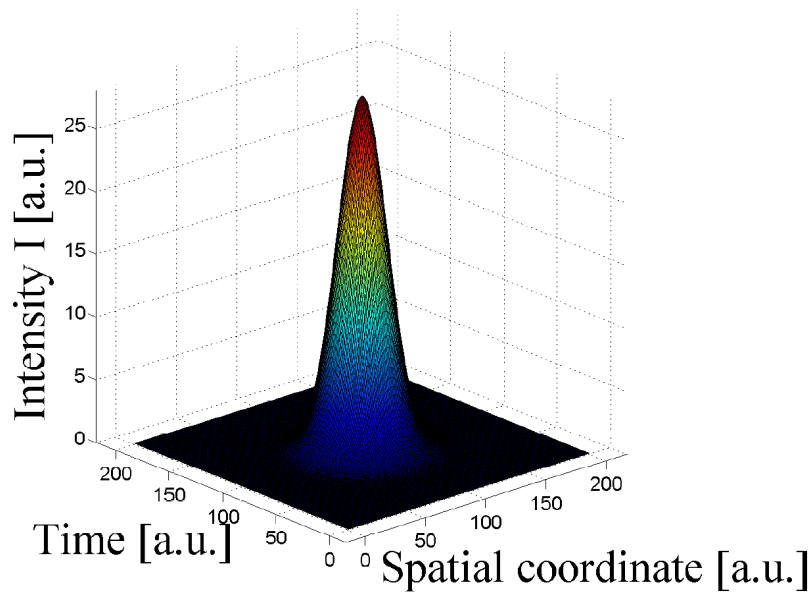


Figure 2.12: 3D illustration of a gaussian pulse using Matlab.

The fluence $F_{fl}(r)$ of a radially symmetrical Gaussian laser pulse has also a Gaussian distribution [51]:

$$F_{fl}(r) = F_{fl,peak} e^{-2\frac{r^2}{w_0^2}} \quad (2.97)$$

The area integration of the fluence gives the laser pulse energy E :

$$E = \int_0^{2\pi} \int_0^\infty F_{fl,peak} e^{-2\frac{r^2}{w_0^2}} r dr d\theta \quad (2.98)$$

After simple algebraic calculations, one can obtain:

$$E = \frac{F_{fl,peak}\pi w_0^2}{2} = \frac{F_{fl,peak}\pi D_0^2}{8} \quad (2.99)$$

The peak fluence $F_{fl,peak}$ can then be determined with known laser pulse energy and beam diameter, which can be directly measured in the experiments:

$$F_{fl,peak} = \frac{8E}{\pi D_0^2} \quad (2.100)$$

The intensity distribution of a Gaussian laser pulse can be written as:

$$I(t) = I_{peak} e^{-4\ln(2)\frac{t^2}{\tau^2}} \quad (2.101)$$

τ is the laser pulse duration. The peak fluence is the integral of the intensity distribution:

$$F_{fl,peak} = \int_{-\infty}^{+\infty} I_{peak} e^{-4\ln(2)\frac{t^2}{\tau^2}} dt \quad (2.102)$$

Thus, the peak intensity can be displayed as:

$$I_{peak} = \frac{2F_{fl,peak}}{\tau} \sqrt{\frac{\ln(2)}{\pi}} = \frac{16E}{\tau D_0^2} \sqrt{\frac{\ln(2)}{\pi^3}} \quad (2.103)$$

I_{peak} is important, because it tells whether an optical breakdown process occurs by comparing with the ionization threshold of certain material. Once the I_{peak} exceeds this threshold, a plasma and a subsequent shock wave can be generated.

Chapter 3

Experimental methods

3.1 Laser differential interferometry (LDI)

The shock flows are investigated by a LDI in the frame of this work. The prototype of the LDI is designed by Smeets [52], while its modification has been applied by our group [40, 53–55]. The basic equations on LDI are firstly derived by Walter Garen (one of my supervisors), and then complemented by me with detailed derivation of the equations, all the sketches and the corresponding description. In contrast to pressure transducers applied by other groups, the LDI offers shock wave density and velocity measurements. This makes our experiments special, among other reasons (will be discussed in the results section).

The working principle of the LDI shown in Fig. 3.1 is explained as follows. The intensities of the two interferometric beams $I_I(t)$ and $I_{II}(t)$ are measured by two photodiode chips (rise time 10 ns), which yield the photo voltage $U_I(t)$ and $U_{II}(t)$, correspondingly. The two photodiodes are integrated into one custom electrical circuit, which gives an output voltage signal $U(t) = U_I(t) - U_{II}(t)$. The circuit is designed to work linearly, meaning $U(t)$ is linearly proportional to $I(t)$. The light intensity on each photodiode chip can be modulated by the interference, because one chip detects the interference maximum, the other chip detects the interference minimum. The interference correlates with the phase difference between the two interferometric beams.

The phase difference between the probe beam and the reference beam results from the difference in the index of refraction, which correlates with the flow density via the Gladstone-Dale relation. As a result, the density $\rho(t)$ of the flow (including shock wave, boundary layer, contact surface, high pressure driver gas) can be deduced from $U(t)$ read from the oscillograph.

The polarization in the first (from left) Wollaston prism of Fig. 3.1 is illustrated in Fig. 3.2. At the exit of this Wollaston, the interference occurs. This Wollaston serves as the mixer for the two components (indicated as a blue and a yellow arrow in the figure)

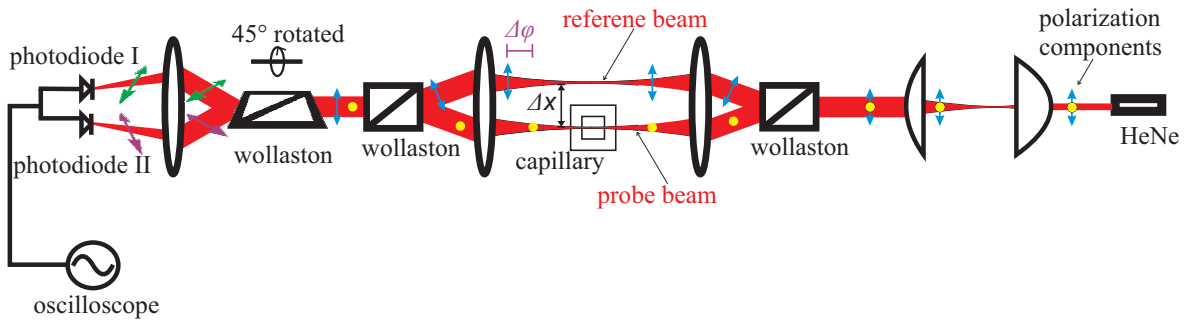


Figure 3.1: Basic setup of a laser differential interferometer LDI.

of the incident beam. In this figure, the two components of the incident beam are sketched with different length indicating the difference in their intensity. Component B of the incident beam may have lower intensity, because it travels through the glass capillary where reflection occurs. However, the outgoing beam I and II have the same intensity, because each outgoing beam takes half the intensity from component A and the other half from component B (due to the 45 degree angle indicated in the figure).

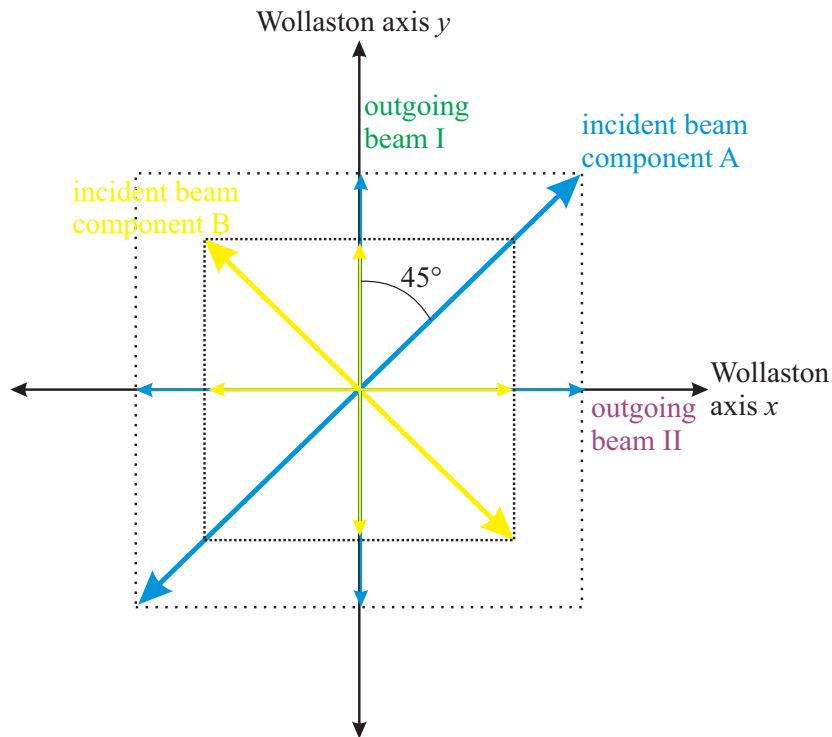


Figure 3.2: Polarization in the first (from left) Wollaston prism. The different sketch colors correlate with the polarizations indicated in Fig. 3.1.

Similar as a Mach-Zehnder or Michelson interferometer, at the plane of the photodiodes, the intensity of one beam is a cosine function of the phase difference, the other beam is a sine function. The beam detected by photodiode I is indicated as beam I, the other is beam II. The photo voltage U_I corresponding to beam I has the following relation with the phase difference $\Delta\varphi$ between the reference beam and the probe beam (marked

in Fig. 3.1):

$$I_I(t) \propto U_I = U_{00} \cos^2(\Delta\varphi) = U_{00} \cos^2\left(\pi \frac{OPD}{\lambda}\right) \quad (3.1)$$

OPD is the optical path difference and U_{00} is the maximum photo voltage.

For the other interferometer beam arrives at the other photodiode:

$$I_{II} \propto U_{II} = U_{00} \sin^2(\Delta\varphi) = U_{00} \sin^2\left(\pi \frac{OPD}{\lambda}\right) \quad (3.2)$$

The photo voltage (corresponds to beam intensity) of the photodiodes as a function of the phase difference is illustrated in Fig. 3.3.

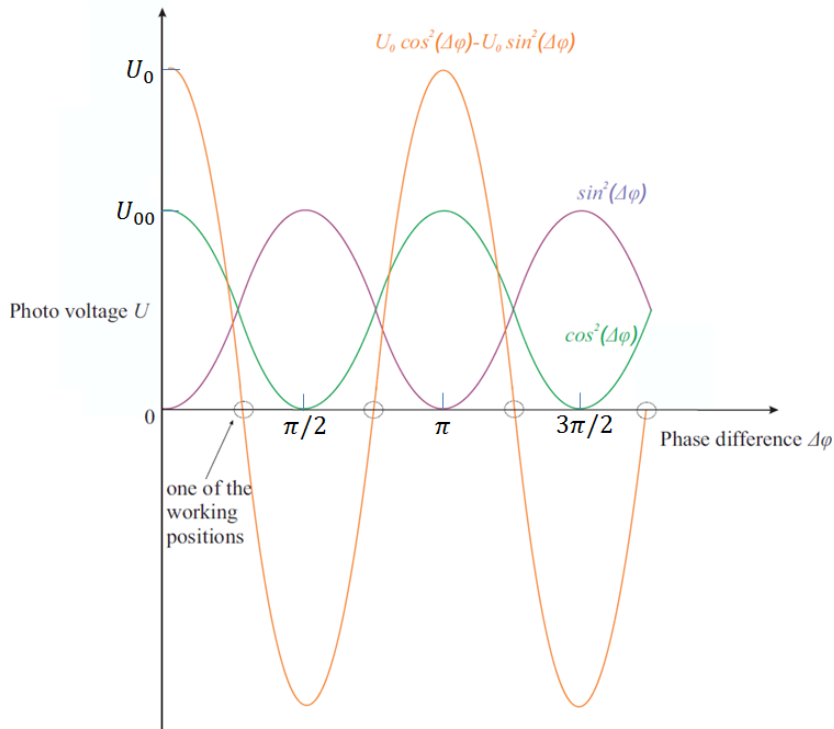


Figure 3.3: Photo voltage U as a function of optical phase difference $\Delta\varphi$. For illustration purpose, not a measured curve.

In this experimental arrangement, the measured total photo voltage U is the difference of the photo voltages delivered by the two photo diode chips. Before the experiment begins, the LDI shall be adjusted to be at a working position (indicated by the circle in the figure), which corresponds to $U = 0$. The adjustment is done through the translational movement of the Wollaston.

The equation for the photo voltage U is:

$$U = U_I - U_{II} = aU_{00} \left(\cos^2\left(\pi \frac{OPD}{\lambda}\right) - \sin^2\left(\pi \frac{OPD}{\lambda}\right) \right) = U_0 \cos\left(2\pi \frac{OPD}{\lambda}\right) \quad (3.3)$$

with a as a amplification factor, and aU_{00} is defined as U_0 . When $2\pi \cdot OPD/\lambda$ equals $(2m - 1)\pi/2$ with integer $m = 1, 2, 3, \dots$, photo voltage U will be zero. In other words,

when $OPD = (2m - 1)\lambda/4$, there is $U = 0$.

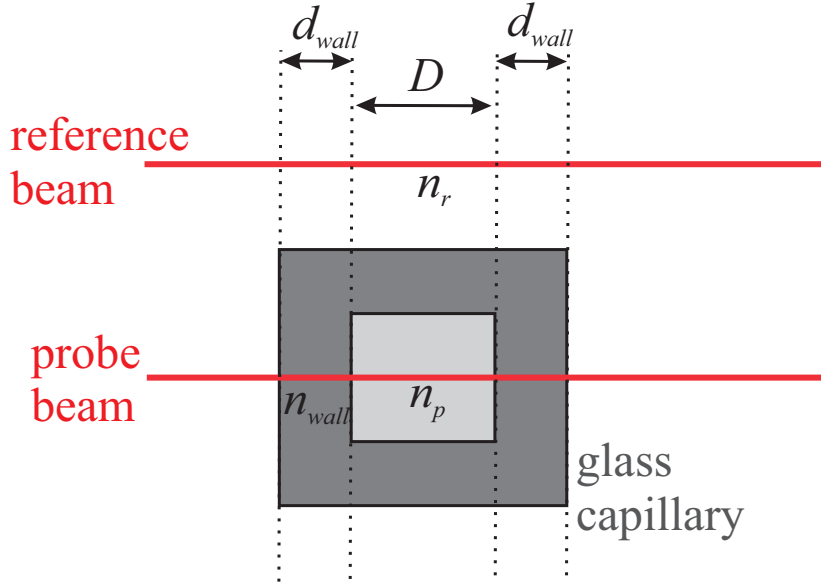


Figure 3.4: Illustration of the optical path difference OPD between the probe beam and the reference beam. The index of refraction of glass $n_{glass} \approx 1.5$.

As shown by Fig. 3.4, the OPD between the two beams is caused by the capillary walls, the flow in the capillary and the different paths in the Wollaston prism (displayed in Fig. 3.5).

$$OPD = (n_{glass} - n_r)2d_{wall} + (n_p - n_r)D + OPD_w \quad (3.4)$$

with the OPD introduced by the Wollaston prism OPD_w , the hydraulic diameter of the shock tube D and index of refraction n . The subscript r stands for ‘reference’, while p for ‘probe’. n_p can be a function of time t , when the medium is a moving shock flow.

Of course, the shock tube doesn’t have to be a glass capillary. Furthermore, it doesn’t even have to be a shock tube but just any phase object, which makes additional phase difference between the probe and reference beam. In order to keep the generosity, we can reformulate Eq. 3.4 as:

$$OPD = (n_o - n_r)d_o + (n_p - n_r)D + OPD_w \quad (3.5)$$

n_o is refractive index of the phase object, while d_o is the corresponding thickness.

The OPD introduced by the Wollaston crystal is:

$$OPD_w = (n_a L_1 + n_b L_2) - (n_b L'_1 + n_a L'_2) \quad (3.6)$$

n_a and n_b are indexes of refraction for the beam perpendicular and parallel to the crystal axis, respectively. L_1 and L_2 are the laser propagation paths (geometrical,

not optical) for one interferometer beam in the first half and the second half of the Wollaston prism, respectively. L'_1 and L'_2 correspond to the other interferometer beam. The sketch for the laser propagation paths in the Wollaston prism is in Fig. 3.5.

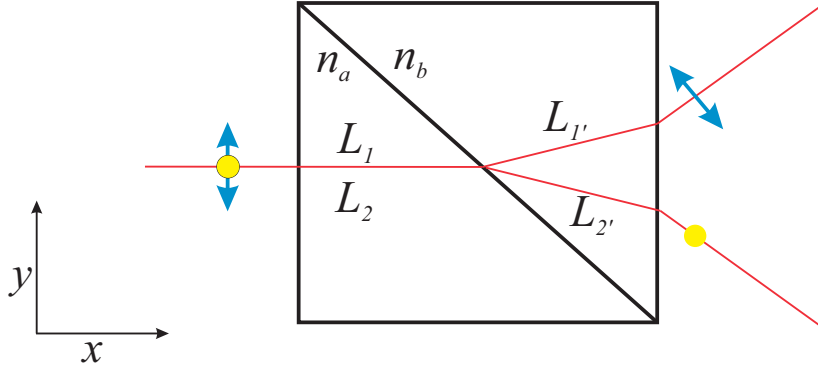


Figure 3.5: Laser propagation paths in the 2nd Wollaston prism from the left.

The Gladstone-Dale relation for gas is [56]:

$$n - 1 = G(\lambda)\rho \quad (3.7)$$

G is the Gladstone-Dale constant. λ is the wavelength in vacuum.

The dimensionless Gladstone-Dale constant κ is defined as:

$$\kappa = G(\lambda)\rho_N. \quad (3.8)$$

ρ_N is the gas density at normal condition.

G for gases depends weakly on the wavelength and temperature, and can be approximately by Taylor series [56]:

$$G(\lambda) = G_0 \left[1 + \left(\frac{A}{\lambda}\right)^2 + \left(\frac{B}{\lambda}\right)^4 \right] \quad (3.9)$$

A and B are parameters affected by the type of gas (given as tabular values in [56]). For our LDI, the wave length is fixed at $\lambda = 632.8$ nm (HeNe laser). The temperature influence is very small. Thus, G is approximately constant for a given gas.

Eq. 3.5 can thus be written as:

$$OPD = (n_o - n_{air})d_o + [(G_p\rho_p + 1) - (G_r\rho_r + 1)]D + OPD_w \quad (3.10)$$

$$= (n_o - n_{air})d_o + (G_p\rho_p - G_r\rho_r)D + OPD_w \quad (3.11)$$

The propagation paths L_1 , L_2 , L'_1 and L'_2 of the two interferometer beams inside the Wollaston prism can be adjusted by simple translational movement (through an optomechanical translational mount) of the prism in y -direction as indicated in Fig.

3.5. By doing this, it can be achieved that $(n_o - n_{air})d_o + OPD_w$ equals to $\frac{2m-1}{4}\lambda$. Therefore, Eq. 3.11 can be written as:

$$OPD = \frac{2m-1}{4}\lambda + (G_p\rho_p - G_r\rho_r)D = OPD_0 + OPD_p \quad (3.12)$$

with $OPD_0 = \frac{2m-1}{4}\lambda$ and $OPD_p = (G_p\rho_p - G_r\rho_r)D$

When the probe and reference beam travel through the same gas at the same condition, i.e. $G_p = G_r$ and $\rho_p = \rho_r$, there is $OPD = OPD_0$ according to Eq. 3.12. The measured signal $U = 0$ according to Eq. 3.3. This situation is thus considered as the equilibrium point or working position as mentioned earlier.

When the shock wave or gas flow starts propagating in the capillary, $OPD = OPD_0 + OPD_p$ with a non-zero OPD_p , thus U deviates from zero.

The combination of Eq. 3.3 and Eq. 3.12 yields:

$$U = U_0 \cos\left(\frac{2\pi}{\lambda}\left(\frac{2m-1}{4}\lambda + OPD_p\right)\right) = U_0 \cos\left(\frac{(2m-1)\pi}{2} + \frac{2\pi}{\lambda}OPD_p\right) \quad (3.13)$$

The LDI is at the working position prior to the experiments, i.e. $m=1, 3, 5, \dots$, thus Eq. 3.13 can be written as:

$$U = U_0 \sin\left(\frac{2\pi}{\lambda}OPD_p\right) \quad (3.14)$$

$$\Rightarrow U = U_0 \sin\left[\frac{2\pi}{\lambda}(G_p\rho_p - G_r\rho_r)D\right] \quad (3.15)$$

One can thus use the directly measured value U to calculate the density of the probed medium ρ_p :

$$\rho_p = \left[\sin\left(\frac{U}{U_0}\right) \frac{\lambda}{2\pi D} + G_r\rho_r \right] \frac{1}{G_p} \quad (3.16)$$

	ambient air	helium
density ρ_N [kg/m ³]	1.205	0.1664
index of refraction n_N	1.0002765	1.000032426
Gladstone-Dale constant G [m ³ /kg]	$2.295 \cdot 10^{-4}$	$1.949 \cdot 10^{-4}$
dimensionless Gladstone-Dale constant κ	$2.765 \cdot 10^{-4}$	$3.243 \cdot 10^{-5}$

Table 3.1: Gas properties of two typical gases used in shock wave research. Data originate in [57] and [58]. Properties correlate with normal conditions (20 °C, 1 atm) and the vacuum wave length $\lambda = 632.8$ nm (HeNe laser line).

The reference beam normally travels through ambient air at normal conditions. Therefore, Eq. 3.16 can also be formulated by using the dimensionless Gladstone-Dale con-

stant κ :

$$\rho_p = \left[a \sin\left(\frac{U}{U_0}\right) \frac{\lambda}{2\pi D} + \frac{\kappa_r}{\rho_{r,N}} \rho_r \right] \frac{\rho_{p,N}}{\kappa_p} \quad (3.17)$$

For the special case that the density jump ρ_2/ρ_1 induced by the shock wave occurs in ambient air, there is $\kappa_p = \kappa_r = \kappa$, $\rho_{p,N} = \rho_{r,N} = \rho_r = \rho_N$ and $\rho_p = \rho_2$. Insert these parameters into the equation above, thus:

$$\frac{\rho_2}{\rho_1} = a \sin\left(\frac{U}{U_0}\right) \frac{\lambda}{2\pi D \kappa} \frac{\rho_N}{\rho_1} + 1 \quad (3.18)$$

In the experiments, the initial pressure P_1 of the test chamber can be measured with a transducer. By using the ideal gas law $P = \rho R_s T$, the equation above is rearranged into the form:

$$\frac{\rho_2}{\rho_1} = a \sin\left(\frac{U}{U_0}\right) \frac{\lambda}{2\pi D \kappa} \frac{P_N}{P_1} + 1 \quad (3.19)$$

Operation arrangements of the LDI:

The LDI can be placed at different distances x from the shock onset position. The LDI has two different arrangements as shown in Fig. 3.6.

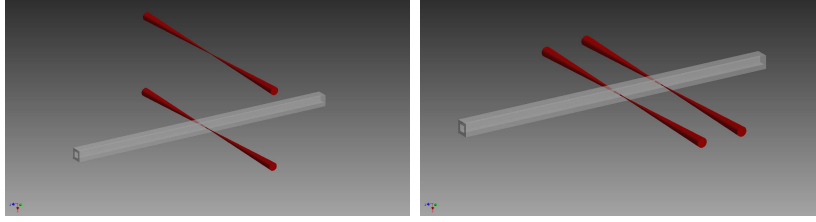


Figure 3.6: Sketch of the two different arrangements of the LDI. Left: one beam out. Right: two beams in.

1. ‘two beams in’ arrangement with both beams passing through the capillary. It is suitable for the time-of-flight method for a direct measurement of the shock wave velocity u_s :

$$u_s = \frac{\Delta x}{\Delta t} \quad (3.20)$$

The distance between the two interferometer beams is $\Delta x = (370 \pm 10) \mu\text{m}$ as default. Δt is the time difference between the shock wave reaching the first LDI beam and the second, $\Delta t = t_2 - t_1$ (as denoted in Fig. 3.7). Δt can be thus determined by reading the oscillograph. The system error of Δt is mainly the data reading error affected by the sampling rate of the oscilloscope, which has the maximum bandwidth of 500 MHz. An illustration (without presenting concrete values) of the shock flow density measured by the ‘two beams in’ arrangement is shown in Fig. 3.7.

2. ‘one beam out’ arrangement with only one beam passing through the capillary, the other passing above the capillary. This arrangement is especially useful for the long term measurements of the flow density $\rho(t)$, especially the density jump across the shock wave ρ_2/ρ_1 . The trajectories of the shock wave $x_s(t)$, the contact surface $x_c(t)$ and the expansion fan $x_e(t)$ are determined using this arrangement.

An illustration of the shock flow density measured by the ‘one beam out’ arrangement is shown in Fig. 3.8.

In this figure, it can be seen that the abrupt edges are induced by the shock wave and the contact surface, respectively. The slow increase in density corresponds to the boundary layer development. The detailed explanation of the measured curves are discussed later in the results chapters.

The timing to read the photo voltage corresponding to ρ_2/ρ_1 or ρ_2 (if ρ_1 is known) from the oscillograph trace in Fig. 3.8 is tricky. It can be explained by the sketch in Fig. 3.9.

As shown in Fig. 3.9, in case the shock wave is curved, the density behind the shock

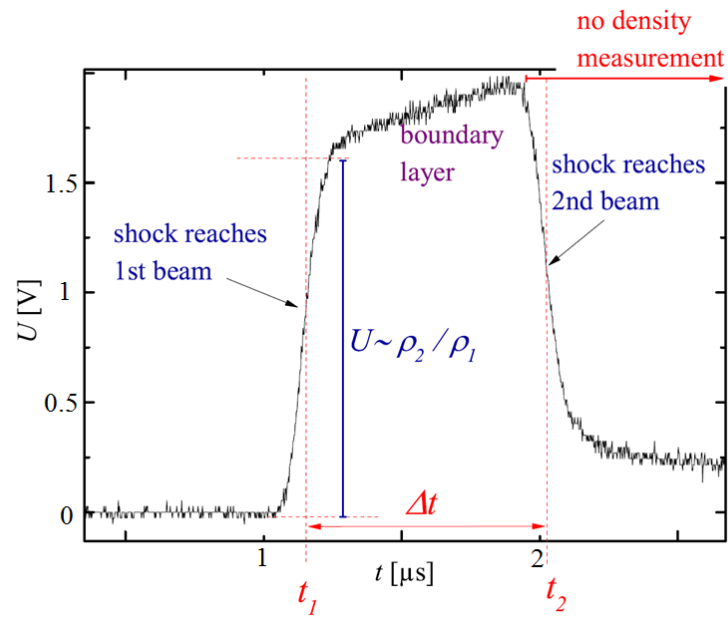


Figure 3.7: A typical oscillograph trace of a shock wave measured by the ‘two beams in’ arrangement of the LDI. The values on the axes are exemplar and trivial for the illustration.

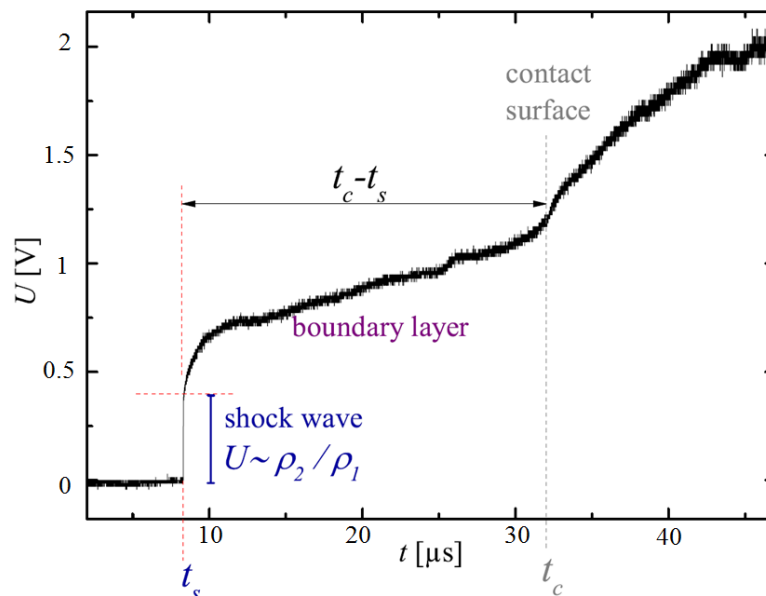


Figure 3.8: A typical oscillograph trace of a shock flow measured by the ‘one beam out’ arrangement of the LDI. The values on the axes are exemplar and trivial for the illustration.

wave ρ_2 measured by the interferometer may deviate from the actual ρ_2 . This is due to the fact that the probe beam of the LDI may integrate along the dot line through the region ahead the shock front and behind the shock front. On the other hand, when the probe beam travels through the boundary layer along the dash-dot line, the measured ρ_2 is actually a mixture of the boundary layer and the core flow behind the shock wave.

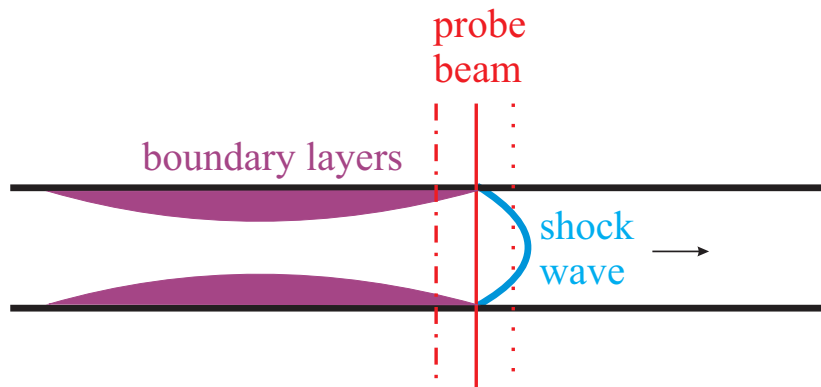


Figure 3.9: Measurement of the density behind the shock wave ρ_2 . Red straight line: the probe beam of the LDI is positioned behind the shock wave but before boundary layer development. Dash-dot line: the probe beam travels through the boundary layer. Dot line: the probe beam travels through the curved shock wave.

The best timing to determine the value of ρ_2 is when the probe beam travels along the solid line, i.e. it is behind the shock wave but before the boundary layer development. As long as the shock tube is not too small, i.e. the shock front is not spherical, a density measurement can be accurately performed. This statement can be evidently proved later in this thesis in Fig. 5.18.

Adjustment of the LDI

We observe the plane of the photodiodes in Fig. 3.1. Here instead of the photodiodes, a white screen e.g. a piece of A4 paper is placed there or simply further away. Beam I and beam II are visible on the screen as two spots, which are displayed in Fig. 3.10.

The distance between the interference maxima d_m shall be big enough, meaning that one beam on the screen can have almost completely constructive interference, the other almost completely destructive. In this case, the LDI has the highest sensitivity. The adjustment can be done by rotating the second Wollaston from the left in Fig. 3.1.



Figure 3.10: Beam profiles of the LDI at the plane of the photodiodes. They are displayed on a white screen for adjustment. Left: bad adjustment. Middle: good adjustment. Right: working position

Fig. 3.10 shows that white screen with the beams on it. In case of bad adjustment, the distance between the interference maxima d_m is not big enough, so that there are interference fringes inside each beam. In case of good adjustment $d_m \rightarrow \infty$, one beam has constructive interference, the other destructive interference. When good adjustment is achieved, the Wollaston can be moved translationally to the working position as indicated in Fig. 3.3. At the working position, each beam has the phase exactly in the middle of the interference maximum and minimum.

3.2 Schlieren optics using a double-cavity laser

In this part of the experiments, a setup of Schlieren optics is arranged. The working principle of Schlieren optics is described in details in [56]. The setup is sketched in Fig. 3.11.

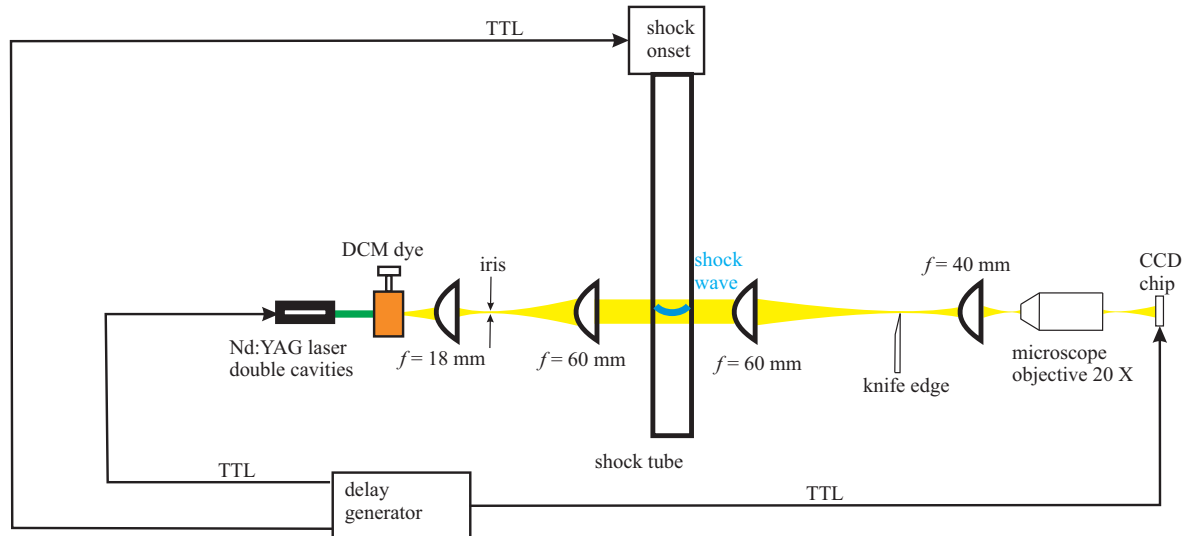


Figure 3.11: Schlieren setup for imaging the micro shock wave.

The schlieren setup uses collimated light propagating through the test object (in our case, the shock wave) to be photographed. Variations in the density gradients induced by the shock wave distort the collimated light beam. This distortion creates spatial variation in the intensity of beam, which can be visualized with a shadowgraph system. After propagating through the shock wave, the collimated light is focused with a converging lens. A knife-edge is placed at the focal point to block half of the beam. When this is no shock wave, the photograph is just half as bright as without the knife-edge. However, due to the appearance of a shock wave, the beam is deflected from its original orientation. This beam is no longer parallel, so it doesn't intersect the focal point of the focusing element and is not blocked by the knife-edge. In some circumstances the deflected beam escapes the knife-blade and reaches the camera to create a point-like image on the camera-sensor, with a position and intensity related to the inhomogeneity experienced by the beam. An image is then formed in this way.

The result is a set of lighter and darker patches corresponding to positive and negative fluid density gradients in the direction normal to the knife-edge. When a knife-edge is used, the system is referred to as a schlieren system, which measures the first derivative of density in the direction of the knife-edge. If a knife-edge is not used, the system is referred to as a shadowgraph system, which measures the second derivative of density [56].

Different from the LDI and fiber optics measurements, the Schlieren optics enable the 2

dimensional investigation of micro shock waves. Simply because the photographs taken by the Schlieren optics are 2D, which contain useful information not only along the shock wave propagation axis but also along the axis perpendicular to the propagation. The shock wave pattern can thus be studied this way. The study of the boundary layer development and the shock/wall interaction are also possible. The resolution of the Schlieren optics is not investigated in the frame of this thesis, because the main goal is to make a photo of the shock front instead of the detailed internal structure of the shock wave. The goal has been achieved.

The Schlieren setup is to be seen in Fig. 3.11. The main component is a double-cavity Nd:YAG laser (pulse duration 6 ns, pulse energy 25 mJ, model *Solo III 15*, New Wave). The reason to use two cavities is that two laser pulses can be emitted with a user-defined time delay. The double pulses enable double exposures for one photo. Later in the experiments, the propagation distance of the shock wave between the two exposures time can be measured from the photo. By applying the time-of-flight method, the shock wave velocity can be determined.

Another special component here is the DCM dye. After the laser is incident in the dye, fluorescence light will be emitted. Because the fluorescence light is not coherent, it will not produce speckle in the Schlieren photos. Avoiding the speckle is the reason, why the original laser pulse is not directly used for imaging. The fluorescence light pulse is measured (by a photodiode) to be around 10 ns, which is only a bit longer than the incident laser pulse with the duration of 6 ns.

Furthermore, by comparing the trajectory measurements ($x - t$ diagram) using the two different experimental methods, one can check the reliability of the two setups. In the reality, the trajectory of the shock wave shall be independent of the diagnostics methods. Of course, there are some limitations of this Schlieren setup: 1. It has proved to be less sensitive than LDI. 2. It can't record the long term evolution of a shock wave, because the exposure time is limited by the fluorescence light pulse.

3.3 Plasma induced shock waves

This section is published in [17, 59].

In general, it is a big challenge to directly generate shock waves at micro scale, because the conventional diaphragm shock tube (explained in section 2.2.2) fails since there is rarely a diaphragm which breaks spontaneously at this range. To meet this challenge, in the frame of the current project, a novel shock tube is developed involving laser-plasma induced micro shock waves (LIMS). The hereby induced shock wave can be as small as the focus diameter of the laser beam. Thus the theoretical lowest shock dimension is defined by the diffraction limit of the focusing optics (a lens or a microscope objective). Therefore, shock waves at the scale of several micrometers or even hundreds nanometers can be generated by this method. LIMS is not only applicable to such small dimensions, but also has the advantage that the high driver pressure can be created very quickly in a small volume, which results in very small shock formation length.

The working principle of LIMS is shown in Fig. 3.12. A high power laser pulse is focused through a thin glass plate onto a thin aluminum layer evaporated on the rear side of the plate, where it generates almost instantaneously a laser produced plasma. The sudden occurrence of a high pressure high temperature plasma is an extreme non-equilibrium. To achieve the balance again, a shock wave as natural phenomenon is emitted. Thus this plasma acts as a driver for the shock wave which then propagates into a capillary positioned in the immediate vicinity.

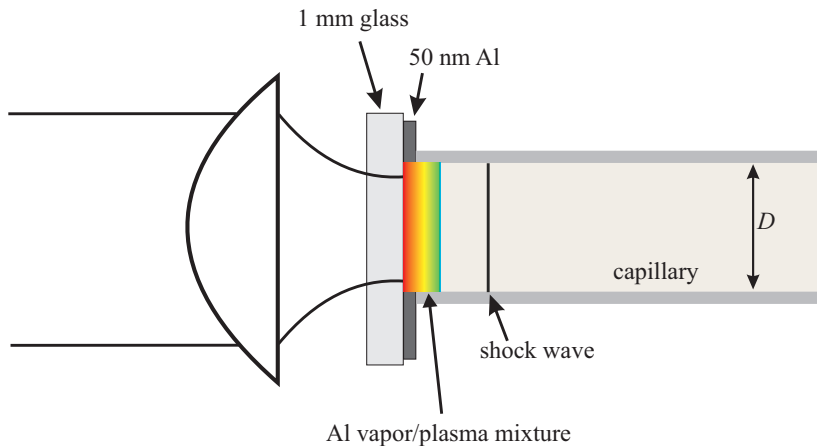


Figure 3.12: Illustration of the LIMS (Laser-plasma Induced Micro Shocks). The gradual color change illustrates the density distribution of the target after exposure. The original idea is developed by my advisers Teubner and Garen.

Fig. 3.13 shows the image of a target after exposure with one fs-laser pulse. The diameter of the ablated region fits well to the tube cross-section. It leaves an undisturbed glass surface behind. A similar statement can be made for bigger tubes analyzing a similar microscope image of the target. The smooth surface outside of the ablation region shows the condition prior to the exposure.

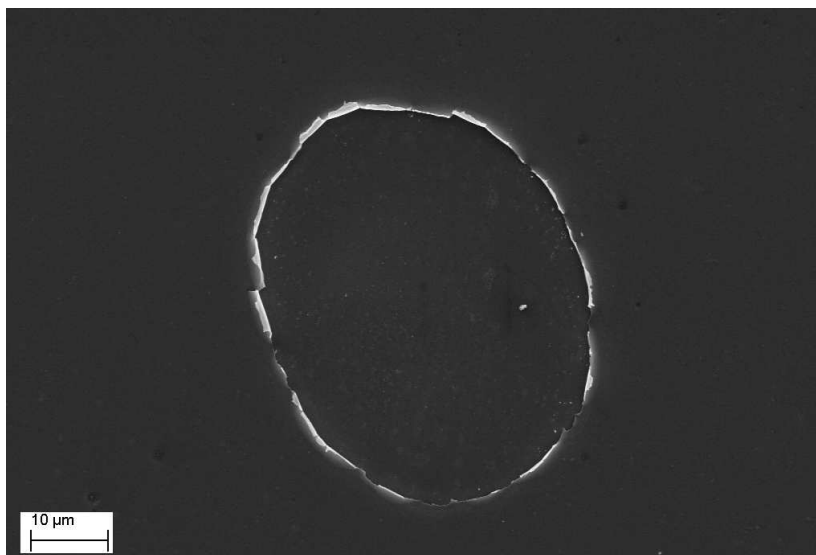


Figure 3.13: SEM (Scanning Electron Microscope) image of a target with a 50 nm Al layer after shock wave generation via plasma in front of a 50 μm tube (front view). $I = 2 \times 10^{13} \text{ W/cm}^2$, $E_L = 20 \mu\text{J}$

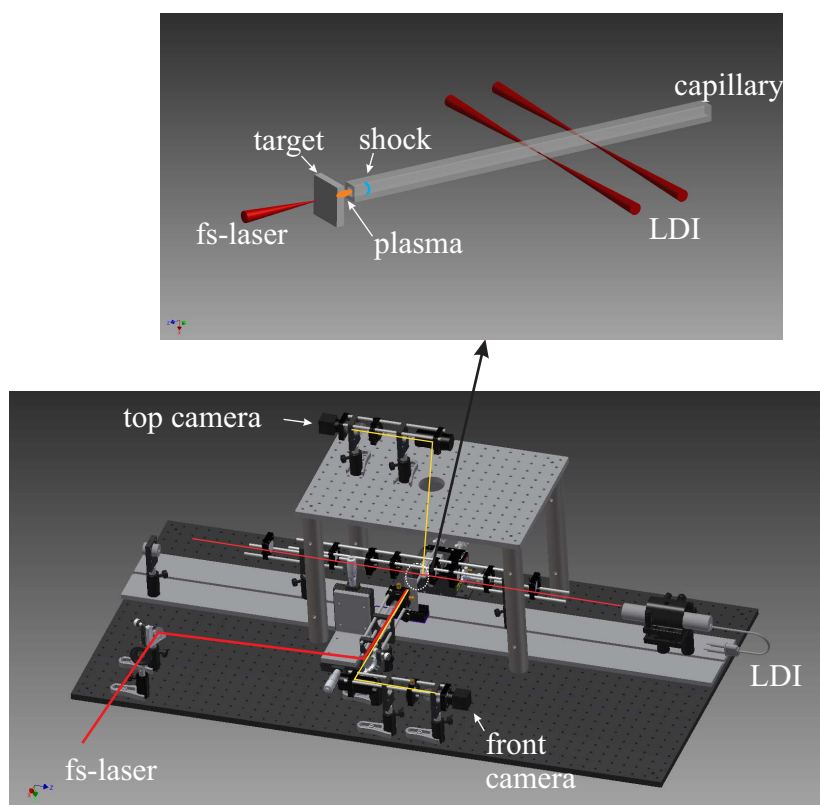


Figure 3.14: The setup for the LIMS experiments. The upper figure is a zoom-in view of the area indicated by the white circle.

The shock wave propagation in the capillary is investigated by the laser differential interferometer (LDI) as presented in section 3.1. Since the experiment requires very high precision and resolution, I have constructed a setup to incorporate the LDI, two

microscopes with cameras (to provide top view and front view of the capillary), a micro positioner holding the capillary, a motorized micro stage (to position the target) and a lens with micro translation mounts (to focus the fs-laser at variable positions). A sketch of the workstation is to be seen in Fig. 3.14.

Experimental conditions:

Titanium:Sapphire laser (Clark-MXR, linearly polarized, $\tau_L = 150$ fs in FWHM, wavelength 775 nm, maximum pulse energy 1 mJ) is applied for shock generation. The pulse of this fs-laser is focused at normal incidence by a plano-convex lens with long focal length f . This yields a large focus, which is necessary for a lateral plasma that well fits to the capillary diameter. Experiments are performed with lenses of different f . The peak intensity I_{peak} (calculated by Eq. 2.103) of the laser pulse is beyond the optical breakdown threshold of Al (2×10^{12} W/cm²) and close to the breakdown threshold of glass (2×10^{13} W/cm²), but well below the breakdown threshold of air (5×10^{14} W/cm²). All values given in brackets are deduced experimentally for conditions of the present work. The plasma formation is mostly restricted to the thin Al-layer (no detectable shock wave occurs, if there is only the glass without the Al layer).

The plasma here is treated by a simple 'δ-pulse model' (approximated by the mathematical δ-distribution) [33], which estimates the initial conditions of the plasma generated by an ultrashort laser pulse (examples in [60], [61]). The δ pulse model is a reasonable assumption, when the corresponding laser pulse duration τ_L is much shorter than the shock formation time. To achieve this, it is advantageous that τ_L is in the ps or fs range (later verified by the MULTI-fs simulation). The plasma acts as a homogenous quasi planar driver for the shock wave, because the plasma is generated in the way that it is approximately of the same lateral diameter as the corresponding capillary.

Due to the fast non-linear heat wave within the thin Al layer, the plasma is nearly homogeneously heated and ionized [33]. Thus the electron pressure P_e is approximately constant all over the plasma. For the typical value of $I = 2 \times 10^{13}$ W/cm² of the laser pulse in this work, the initial electron temperature is several eV, the average ionization degree of the plasma is approximately 3 and thus the electron density is approximately 2×10^{23} cm⁻³, which is hundred times the critical density. During the laser pulse itself, due to the large inertia, the electrons and ions are not in equilibrium. Only after a few ps both temperatures are equalized to a common temperature. Within a few ps, the plasma begins to expand significantly. [33]

Laser absorption on the Al target:

The absorbed energy of the fs-laser pulse in the target correlates with the energy input for the shock wave. That's why the absorption is an important parameter.

To determine the laser absorption on the Al target, the corresponding reflection and transmission measurements are carried out. The target with the Al layer thickness of 50 nm is chosen, because Al layers (partly oxidised) of different thickness between 30 nm and 100 nm are tried for shock generation, and the best suitable (in the sense of generating strong shocks) thickness is 50 nm.

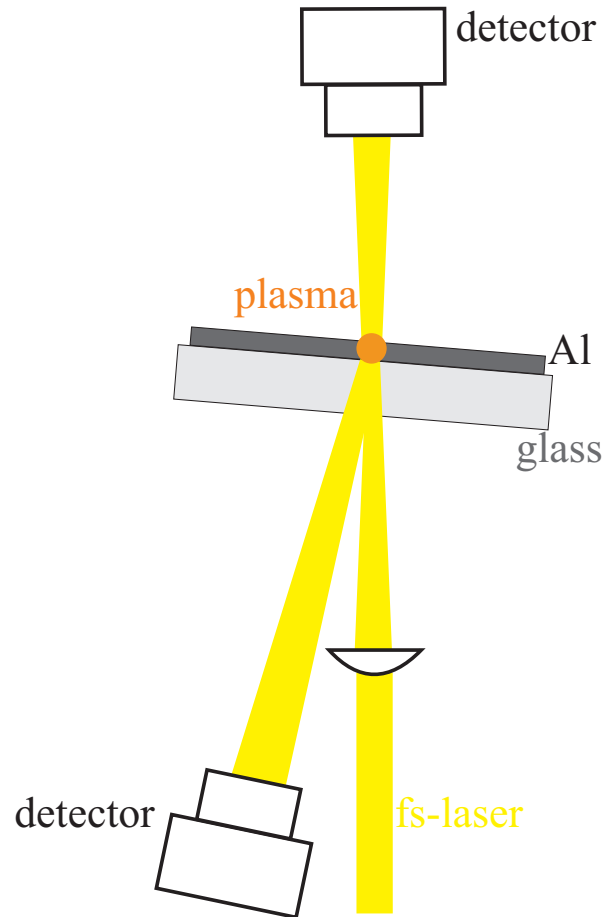


Figure 3.15: Transmission and reflection measurements of the fs-laser beam.

Fig. 3.15 shows the setup to measure the transmission and reflection of the fs-laser beam on the target. The target is slightly tilted against incident laser (not perpendicular incidence), but this angle is very small (around 1 degree). Here in this figure, we firstly applied a thermopile detector (Coherent, LabMax-TOP), which is set to detect the light of the wavelength 775 nm. Since plasma is generated, white light is emitted from the plasma. Therefore, the detector register not only the reflected and transmitted laser light, but also a small fraction of the white light as error. However, this error is negligibly small, because the white light has a broad band and is spherically (in all directions) emitted, while the detector is only sensitive to the wavelength 775 nm and covers spatially a small surface at a certain angle. In the experiments, the focusing lens can be removed to avoid plasma generation, thus avoiding the white light as the source of error. It is experimentally proved that, the reflection measurements with or

without the lens have the difference of much less than 5 %. The reflection of the Al layer is determined as 65 %, which is measured at $I_{peak} = 2 \times 10^{13}$ W/cm², i.e. the standard intensity for shock generation in this project.

The thermopile detector is also applied to measure the transmission at the same conditions, but the transmitted energy is smaller than the sensitivity limit of the detector. Consequently, a photodiode is applied instead to measure the transmission. For the transmission measurement, the lens in Fig. 3.15 is removed to avoid plasma generation. Consequently, the laser intensity on the target is lower, i.e. $I_{peak} = 3 \times 10^8$ W/cm². The thereby determined transmission is 4.8 %. Upon knowing the reflection and transmission, the absorption is determined as approximately 30%.

By the known transmission and the layer thickness, the corresponding penetration depth can be determined as 16.5 nm (by applying Beer-Lambert law). Due to oxidation, this penetration depth is larger than the penetration depth of pure Al (7.1 to 7.5 nm [62]), but it is still much smaller than 50 nm. As a result, strong absorption of the laser energy on the target occurs i.e. 6 μ J out of the 20 μ J incident laser energy is deposited on the target and then contributes to shock wave generation. A similar value of absorption is found in the MULTIfs simulation in section 4.2.

Estimation of the initial pressure:

In case of the conventionally generated shock waves involving a diaphragm, the pressure of the driving gas is one of the most important parameters that affect the shock strength. Naturally one can come to the question, what is the initial pressure driving the plasma shock wave? In this part, the question shall be answered.

The acoustic wave intensity I can be calculated according to [63]:

$$I = P \cdot u_a \quad (3.21)$$

P and u_a are the pressure and sound velocity, correspondingly. For the plasma, the δ -pulse model evaluation yields the ion sound velocity $u_{a,p} \approx 10^4$ m/s, the pressure $P_p \approx 10$ Mbar [33]. Here, the subscript ‘p’ indicates plasma, while ‘A’ indicates air.

Therefore, the acoustic wave intensity in plasma I_p is calculated according to Eq. 3.21 as:

$$I_p = P_p \cdot u_{a,p} \approx 10 \text{ Mbar} \times 10^4 \text{ m/s} = 10^{12} \text{ W/cm}^2 \quad (3.22)$$

The wave impedance can be calculated as [63]:

$$Z = \rho \cdot u_a \quad (3.23)$$

ρ is density.

According to Eq. 3.23, the wave impedance of air Z_A is:

$$Z_A = \rho_A \cdot u_{a,A} = 1.205 \text{ kg/m}^3 \cdot 343 \text{ m/s} \approx 413 \text{ kg/(m}^2\text{s)} \quad (3.24)$$

with ambient air density $\rho_A = 1.205 \text{ kg/m}^3$ and sound velocity in air $u_a = 343 \text{ m/s}$.

By assuming that the initial density of the plasma ρ_p is approximately the aluminum density $\rho_{Al} = 2.7 \times 10^3 \text{ kg/m}^3$, the wave impedance of plasma Z_p is calculated according to Eq. 3.23:

$$Z_p = \rho_p \cdot u_{a,p} \approx \rho_{Al} \cdot u_{a,p} = 2.7 \times 10^3 \text{ kg/m}^3 \cdot 10^4 \text{ m/s} = 2.7 \times 10^7 \text{ kg/(m}^2\text{s)} \quad (3.25)$$

The pressure of the plasma is transmitted into the air with certain loss due to reflection. The transmitted wave intensity in air is [63]:

$$I_A = 4I_p \frac{Z_p Z_A}{(Z_p + Z_A)^2} \quad (3.26)$$

Inserting previously determined Z_A , Z_p and I_p into Eq. 3.26, one can determine $I_A \approx 6 \times 10^7 \text{ W/cm}^2$. Furthermore, when I_A and $u_{a,A}$ are inserted in Eq. 3.21, the transmitted pressure into air can be determined:

$$\boxed{P_A = I_A / u_{a,A} = 6 \times 10^7 \text{ W/cm}^2 \cdot 343 \text{ m/s} \approx 1.8 \times 10^4 \text{ bar}} \quad (3.27)$$

P_A is roughly the initial driving pressure for the shock wave in air.

3.4 Magnetic valve induced shock waves

This section presents a novel method for micro shock wave generation involving a high-speed magnetic valve, which is integrated into a sophisticated high pressure and vacuum system.

Different from other works, the current setup detects flow density instead of flow pressure by the use of a laser differential interferometric (LDI). Most importantly, the present method resolves the contact surface. To the best of my knowledge, the current work presents the first measurement of the contact surface together with the corresponding shock wave at micro scale.

The detailed experimental setup is sketched in Fig. 3.16. The flow system consists of: 1. a high-pressure part, whose pressure is controlled by the pressure regulator of the gas bottle. 2. a vacuum system, which regulates the low-pressure part of the system, namely the capillary and the buffer volume.

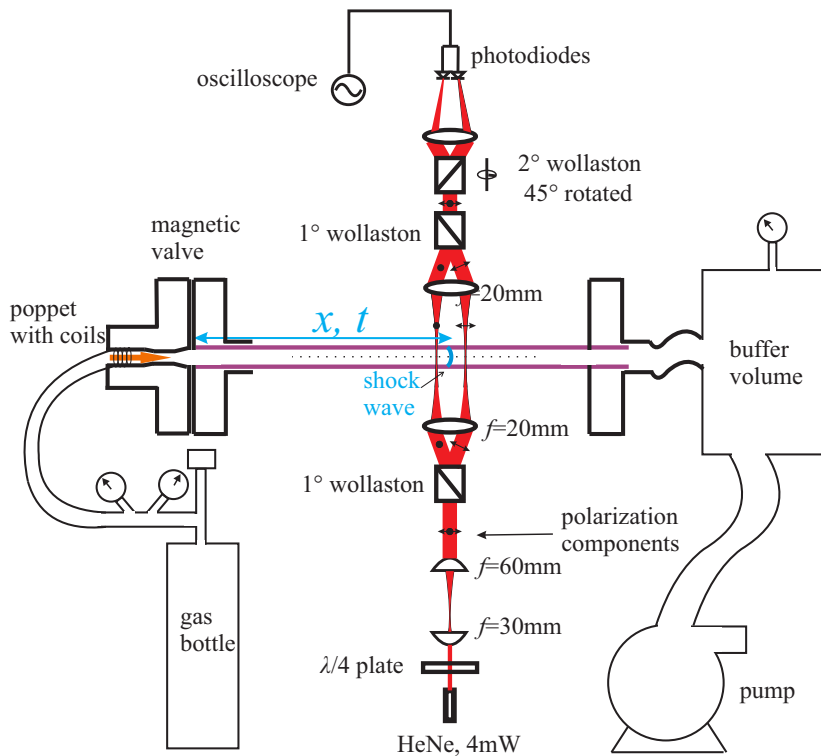


Figure 3.16: Experimental setup. Diagnostics by the LDI. Shock wave generation by the high-speed magnetic valve. Blue: shock wave and related variables, purple: capillary.

The working principle of the magnetic valve (Parker Hannifin, series 9) is as follows: When the valve is triggered, the electric current flows in the coil (in the valve) and creates a magnetic field, which pulls the poppet towards the bottom of the valve. Subsequently, the high pressure gas passes around the poppet and enters the capillary. The valve opening time or called rise time is $160 \mu\text{s}$ (given by the data sheet). This is

verified in our interferometric measurement (170 ± 10) μs , which detects the mechanical vibration of the capillary wall induced by the poppet movement. The mechanical vibration doesn't disturb the measurement of shock wave. Because the sound speed in glass (between 3950 and 5000 m/s) is much faster than in air (343 m/s) under normal conditions, the signal of the shock wave and the wall vibration can be well separated. Square glass capillaries (CM scientific) with an hydraulic diameter of $D = 200 \mu\text{m}$ and $300 \mu\text{m}$ are mainly applied. The length of the $200 \mu\text{m}$ capillary is 300 mm, while the $300 \mu\text{m}$ capillary has the length of 600 mm. The capillary wall is half as thick as the diameter of the corresponding capillary.

3.5 Measurement error

The main experiments of this thesis are performed by using the setups from section 3.1 to section 3.4, i.e. shock generation via plasma or valve with the LDI as the diagnostic. The corresponding measurement scheme and error are explained in this section. The main measurement schemes are illustrated in Fig. 3.17.

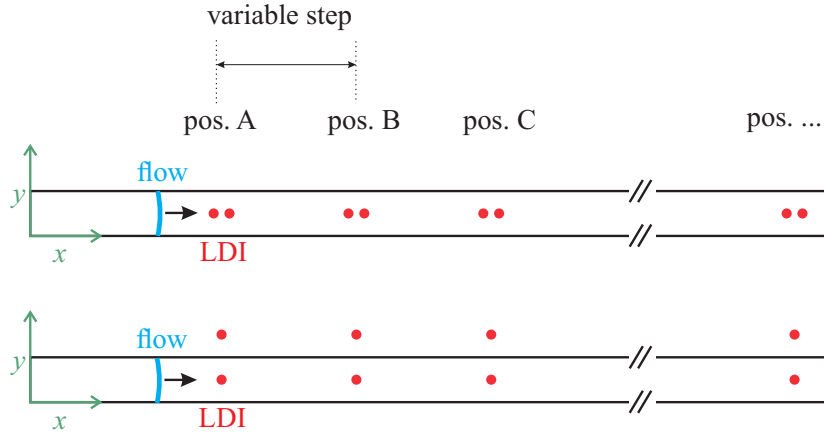


Figure 3.17: Illustration of the measurements. Top: measurements using the LDI with the ‘two beams in’ arrangement. Bottom: measurements using the LDI with the ‘one beam out’ arrangement. (refer to section 3.1) ‘pos.’ is short for position.

As indicated in Fig 3.17, the measurements are performed at different positions with spatial coordinates x , which is also the propagation distance of the shock wave. $x = 0$ is the position where the shock wave is generated. The shock wave is repeatedly generated, and then measured at different x again and again i.e. multi-shots experiments. In the end, the experiments at each x are repeated at least 20 times. Of course, due to maladjustment, some measurements are not suitable for further evaluation. A maladjustment can be immediately noticeable during the measurement e.g. the signal is specially noisy, the aluminum target has irregularities on its surface, or the contact surface doesn’t make a clear signal due to insufficient pumping (to pump out the rest helium from previous experiment) of the capillary prior to each measurement.

The data evaluation uses the average value of 5 successive measurements for each position x . Although the experiments are actually repeated much more than just 5 times as mentioned before, the initial few shots serve for the adjustment purpose. Therefore, when the setup is well adjusted and stable, 5 successively repeated measurements are taken into the calculation. The shot-to-shot difference or error is mainly due to the reasons:

1. The electronics has uncertainties e.g. jitter (a few ns) of the trigger signal supplied by the fs-laser controller or the valve controller with fluctuation in the reaction time ($< 8 \mu\text{s}$).
2. The room temperature has certain fluctuation that is normally $\pm 2 \text{ }^\circ\text{C}$. This affects

the local sound velocity, which affects the shock velocity.

3. Atmospheric pressure has fluctuation around 50 mbar, which is monitored by a pressure sensor. The variation in atmospheric pressure can affect the driven section pressure P_1 (when it is set to ambient conditions), which further affects the driver/driven pressure ratio P_4/P_1 of the shock tube. When this ratio is changed, the thereby generated shock wave strength is influenced.

4. Mechanical vibration of the setup can occur if there is transport of heavy object near the lab. Small vibration can disturb the micro scale experiments. But this doesn't happen regularly and special attention is paid. For example, experiments are repeated on different days at different time (sometimes even at the evening).

The effect of each of the aforementioned uncertainty cannot be singled out and measured individually. But the combined effect i.e. the shot-to-shot difference is measured in the experiments.

Data reading from the corresponding oscillograph is performed through a Matlab-script, which is written in the frame of the project.

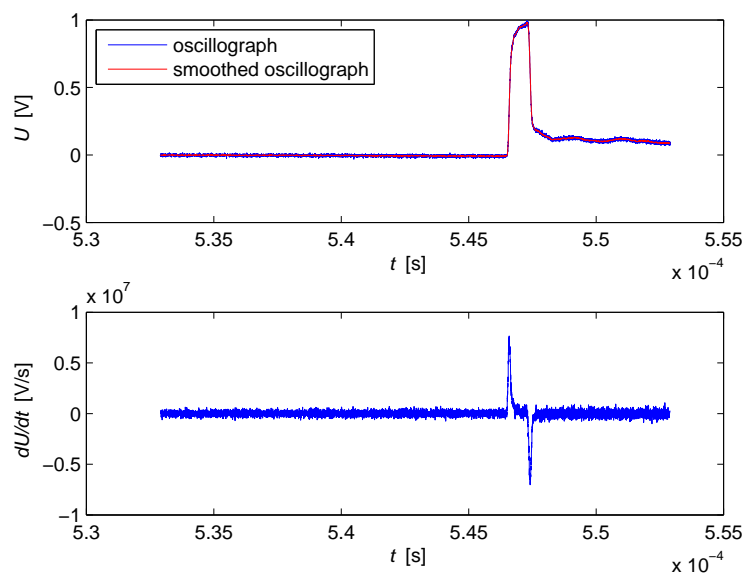


Figure 3.18: Illustration for data reading using a Matlab-script. Top: an oscillograph trace and a smoothed oscillograph trace of the shock wave measured by the ‘two beams in’ arrangement of the LDI. Bottom: derivative of the smoothed oscillograph trace.

Fig. 3.18 shows a representative Matlab graph. In this case, a shock wave is measured by the ‘two beams in’ arrangement of the LDI. Firstly, the Matlab-script imports the oscillograph trace of the shock wave into the program, and then makes a smoothed oscillograph trace (the top part of the figure). The smoothing is done by using a moving average filter with a span of 5, 9, 19 or 29. The best span is automatically chosen by the script under the criterion that the smallest shot-to-shot error shall be resulted. As a remark, all the spans here don't violate the Nyquist sampling theorem.

The smoothed oscillograph trace is differentiated and presented as the bottom part of the figure. The maximum and minimum of the differentiated curve delivers the arrival time instants of the shock wave at the first and the second LDI beams, respectively. These arrival times are involved in the later data analysis to calculate the shock velocity. The shot-to-shot difference in the shock arrival time at each x is several dozens of ns for plasma experiments, while a few μs for the valve experiments (no more than 20 μs). These errors are orders of magnitude smaller than the shock propagation time (several μs for plasma experiments, up to a few ms for valve experiments).

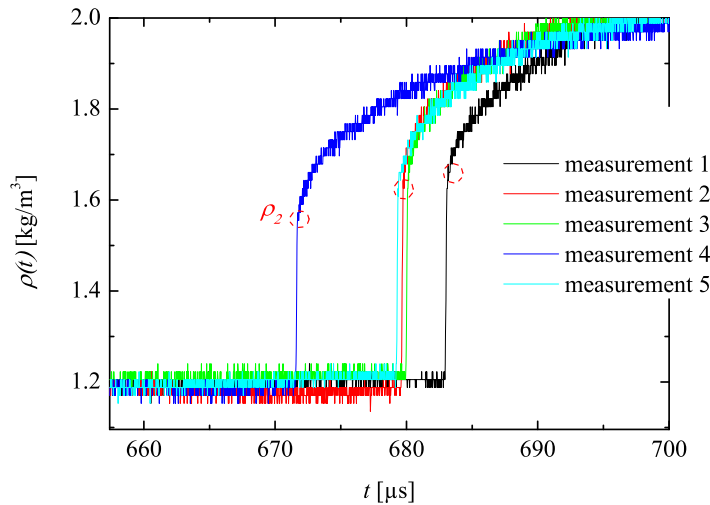


Figure 3.19: Density histories of a shock wave measured five times (repeated under the same conditions) by the ‘one beam out’ LDI arrangement.

In addition to the aforementioned temporal error, there is also error in the amplitude signal. Both errors in the temporal signal and in the amplitude signal occur in the density measurements (here valve induced shocks serve as an example, plasma shocks have similar situation) shown in Fig. 3.19, which is taken at a fixed position x . The sharp edge corresponds to the shock wave, while the slow density growth after the edge corresponds to the boundary layer. The value of the post-shock flow density ρ_2 can be read from the curve highlighted by the red dash circle. In the data reading, there is uncertainty caused by the fact that one cannot be fully sure where exactly the boundary layer growth starts. The data reading error in density is estimated as 0.01 kg/m^3 .

Moreover, the figure shows that there is the shot-to-shot difference between the five repeated density measurements. In the figure, the edges don’t perfectly overlap, which means that each measurement has slightly different shock wave arrival time and the post-shock flow density. Note that this figure is highly zoomed-in, so that this shot-to-shot difference is exaggerated. The value of the shot-to-shot difference is documented

and taken into error propagation analysis.

Beside the shot-to-shot difference, there is a system error mainly due to the length measurements of x using a CMOS camera (for plasma shock experiments) or a tape ruler (for valve experiments). The error of x is estimated as $5\ \mu\text{m}$ for plasma shock experiments, while $0.2\ \text{mm}$ for valve experiments, which are orders of magnitude smaller than the corresponding total measurement length.

Altogether, the error bars are derived from the standard deviation resulted from the shot-to-shot difference and the system error. The error for each measured value is calculated using error propagation. In general, the error is no more than 5 %.

Chapter 4

Results of micro plasma shock waves

Shock waves generated by the LIMS-method (Laser-plasma Induced Micro Shocks) are investigated in this chapter. The corresponding setup is the one in section 3.3. The major results are already published as journal articles in [59] and [17], except the correction of the Rankine-Hugoniot relations.

4.1 LIMS onset

The geometry of the plasma can be manipulated by choosing a lens with different f-numbers to focus the fs-laser pulse.

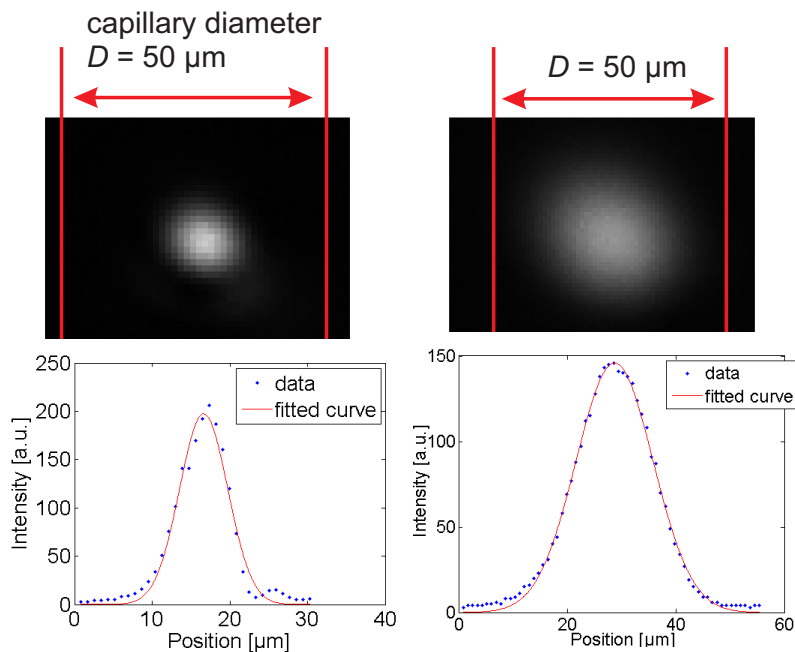


Figure 4.1: fs-laser beam profiles intended for the 50 μm capillary. Left: beam for quasi point-like shocks generation with the focus diameter of 6 μm (FWHM). Right: beam for quasi planar driver with the focus diameter of 21 μm (FWHM).

The focused fs-laser beam at the target position is imaged by a CCD camera and

displayed in Fig. 4.1. Such an image is loaded into Matlab, where a beam profile along a spatial line across the image can be generated. Multiple lines (typically 10 lines here) with different orientations are drawn across the image, so that an average width of the beam can be obtained.

When the incident focused beam has the size close to the capillary diameter, the plasma as driver has quasi planar geometry. When the beam is much smaller than the capillary diameter, the driver is considered as point-like (of course with finite initial volume). Here it may be mentioned that despite the high laser power supplied to the glass plate, the laser pulse intensity is always below the threshold for self-focusing.

In Tab. 4.1 the parameters for shock generation are given.

Capillary diameter D [μm]	No tube	Quasi planar			Quasi point-like
	∞	50	100	200	50
Focus length f [mm]	150	150	300	750	40
f -number	30	30	61	153	40
Focus FWHM-diameter ϕ [μm]	21	21	42	106	6
Laser pulse energy E_L [μJ]	20	20	120	740	20
Laser peak intensity I_{peak} [$10^{13}\text{W}/\text{cm}^2$]	2	2	2	2	30

Table 4.1: Parameters (max. 5% error) for shock wave generation. ‘quasi planar’ and ‘quasi point-like’ correspond to the geometry of the plasma as shock driver.

4.2 MULTIfs simulation

The MULTIfs simulation is done in the frame of a cooperation with Dr. Theodor Schlegel (leading role) from Helmholtz Institute in Jena. This section has already been published in our common paper [17]. The program MULTIfs [64] is applied to make 1D simulation for the light-material interaction between the fs-laser pulse and the Al target. The secondary effect of the light-material interaction is the generation of a shock wave, which also appears in this simulation. Note that, this 1D simulation is limited to the formation phase of the shock wave without the geometrical confinement enforced by the capillary. This is legitimate, because also in the experiments the capillary doesn't play a role yet in the very early stage (i.e. $x \leq D$) of shock onset and propagation. The theoretical study of the subsequent shock propagation through the whole capillary requires 2D Navier-Stokes computation, which is beyond the scope of the present work, which initiates a new method of micro shock generation.

MULTI-fs is a Lagrangian hydrodynamic code with multi group radiation transport. It simulates the laser pulse propagation in the plasma region up to the critical surface by solving the wave equation, which results in a correct model of light reflection in plane geometry and thus provides realistic absorption values. Hence, the overestimation of the dynamic pressure by excessive absorption in the aluminum layer can be avoided.

The ions and electrons in the short-pulse-driven plasma may be far from thermodynamic equilibrium, the code implies separate equation of states (EOS) tables for both species. The EOS data for Al are calculated with FEOS [65, 66] using the soft-sphere approximation [67], which avoids overestimated plasma pressures in the two-phase region up to the critical point. The EOS tables are taken from SESAME library [68, 69]. The MULTI-fs simulation solves equations for electron and ion internal energies, therefore the inverse EOS tables apply. These tables contain pressure and temperature data as functions of plasma mass density and specific internal energy. The data of temperature is required for the evaluation of transport processes in the plasma. Electron collision frequency in the range of classical plasma and in the range of dominating electron-phonon interaction depend on temperature, and determine absorption and electron-ion energy relaxation. The electron thermal conduction is taken into account by means of a harmonic law. It stands for the limitation of an unphysically high collisional Spitzer conductivity in steep temperature gradients by the natural thermal electron flux. Since this work has gentle gradients, a flux limiter of 0.6 was used, which favors the classical conduction process. The opacity coefficients for radiation transport are calculated by SNOP [70], which is a stationary non-equilibrium opacity code. The opacity for nitrogen is applied as approximation for ambient air.

Just as the experimental conditions, the MULTI-fs simulation uses the same set of laser parameters, namely: wavelength 775 nm, FWHM duration of 150 fs with a sin-squared

intensity envelope, peak intensity $2 \cdot 10^{13} \text{ W/cm}^2$. The transparent glass support for the 50 nm aluminum layer is mimicked by the boundary condition of zero flow velocity on the laser-illuminated Al boundary. The simulation shows 26% absorption of the laser energy in the Al layer. This result generally agrees with the experiment. Simulations also show that the electron number density is kept overcritical, which confirms the measured very low transparency. The final simulation results are the mass density, ion/electron pressure, ion/electron temperature and flow velocity as functions of the shock propagation distance for different time instants. The most relevant values for this work are the mass density, ion pressure and flow velocity.

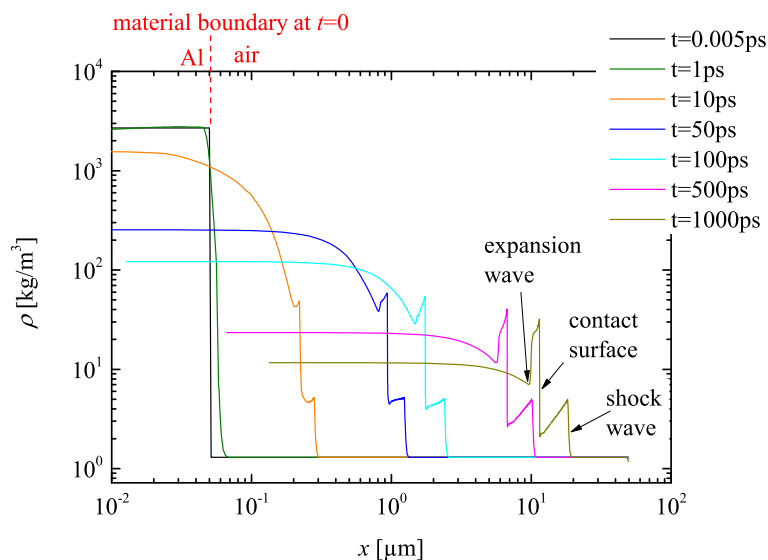


Figure 4.2: MULTIfs simulation of the density (spatial) profiles of the LIMS at initial stage (t from 0 to 1 ns). Different time instant corresponds to different color.

In Fig. 4.2, the simulated mass density (spatial) profiles of the target is firstly chosen to be displayed. $t = 0$ indicates the arrival time of the fs-laser pulse at the left boundary of the Al layer, thus approximately the initiation time of the plasma. Observing the curve corresponding to $t = 1 \text{ ns}$, one can identify the first edge from right to be the shock wave, while the second edge from right the contact surface. At some point, the LIMS is actually quite similar as the shock wave in a conventional shock tube, because of the existence of the contact surface as a driving ‘piston’ behind the shock. But there is also difference: the driver (namely the plasma) of LIMS is extremely short in space and highly unsteady (notice the decreasing plateau). This causes the decrease of the flow density immediately behind the shock front. It is important to remark that the contact surface only exists in the early stage, before the plasma recombination process finishes. This early stage is in the range of ns, but our experiment mainly has the measurement window in the range of μs . Therefore we can not expect to directly measure the contact surface in the experiment. Thus this simulated study on is rather

a supplement for the experimental work. Note that the boundary layer development is not included, since it is 1D simulation. The expansion wave can be identified in the density profile as the first negative peak from left (marked as ‘expansion’ in Fig. 4.2). However, the density behind the contact surface is also influenced by the temperature gradient. Thus, the statement about the expansion wave needs to be verified, which can be done through the pressure profiles in Fig. 4.3.

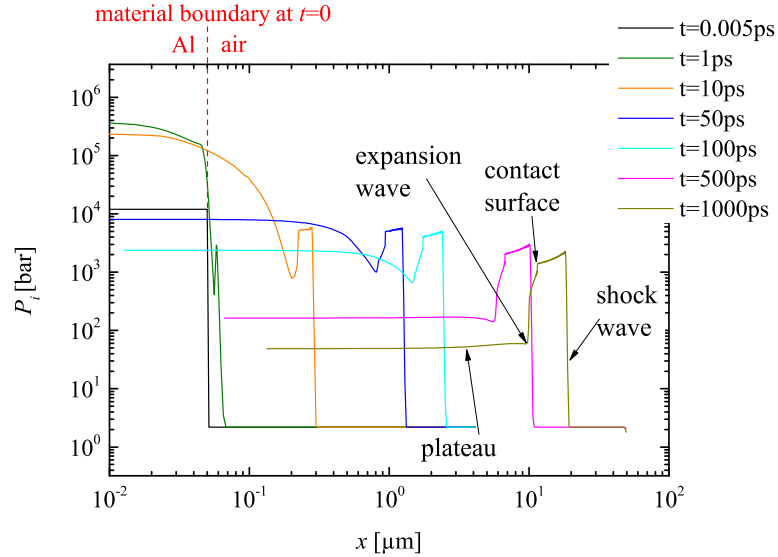


Figure 4.3: MULTIFS simulation of the density (spatial) profiles of the LIMS at initial stage.

The simulated ion pressure profiles are displayed in Fig. 4.3. The electron pressure is also simulated but not shown here, because it is around an order of magnitude lower than the ion pressure after the shock wave breaks out from the plasma into air (a few ps after plasma initiation). Thus the ion pressure is considered as the main driver of the shock. Here the pressure drops immediately behind the contact surface, while the pressure across the contact surface is constant in a conventional shock tube (e.g. in [32]). This difference may be caused by the complicated plasma development and not of further relevance for the present work. Here the contact surface corresponds to the first falling edge (from right, marked in Fig. 4.3), whose verification is shown in Fig. 4.4. Because in Fig. 4.4 the trajectory of the 1st falling edge in the pressure profile overlaps with the trajectory of the 2nd rising edge (already known as the contact surface) in the density profile. The reflected expansion wave (moving from left to right) in the pressure profile corresponds also to the first negative peak from the left (again verified by Fig. 4.4). Further it is consistent with our expectation that the flow density and pressure behind the expansion (towards left hand side) will return to certain plateau value of the driver (marked as ‘plateau’ in Fig. 4.3).

The wave diagram in Fig. 4.4 provides important information on the flow trajectories,

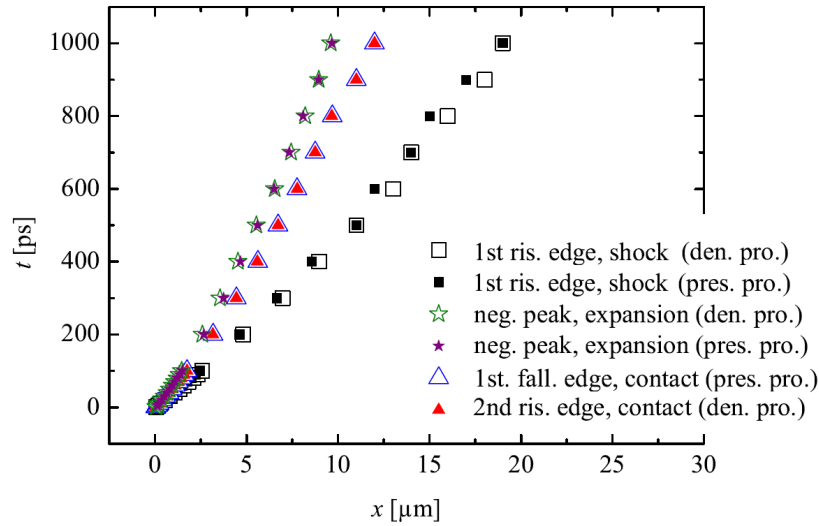


Figure 4.4: Wave diagram of the LIMS at initial stage, retrieved from the simulated data in Fig. 4.2 and 4.3. ‘den. pro.’ is short for density profile and ‘pres. pro.’ for pressure profile.

specially the shock wave and the contact surface. It is noticed that, the contact surface departs further away from the shock wave during the propagation. It is as expected, because the driver density and the corresponding pressure decrease during the propagation, which are the results of the colder plasma due to recombination process and expanding volume.

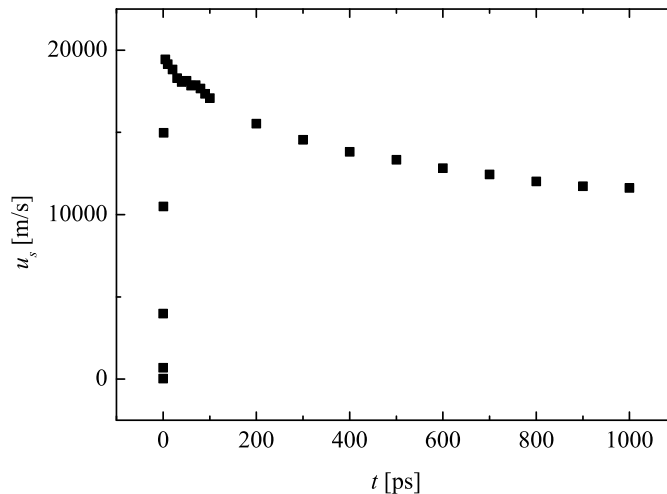


Figure 4.5: Shock wave velocity development of the LIMS at initial stage. Retrieved from the MULTI-fs simulation data of the flow velocity.

Fig. 4.5 shows that the shock wave in air has a formation phase at the beginning, where shock acceleration occurs. This is similar to shock generation in conventional shock tubes. However, the formation phase has taken only dozens of ps. And then, the shock

wave attenuates rapidly. After 1 ns, the shock velocity reduces to approximately half of its maximum value. A few ns later (not simulated here, due to limited computation power), after the plasma fully recombines and gets cold, the shock is expected to attenuate stronger (no more driver). The hydrodynamic equations of the code contain only an artificial viscosity term to broaden the shock front over a couple of mass cells, thus there is no other feasible explanation for this shock attenuation except expansion waves and unsteady driver.

As a final remark, the limited quality of the applied EOS especially in the low-temperature range may distort the quantitative output of the simulations at some extent.

4.3 Geometric influence on shock wave attenuation

In this section, the influence of the propagation geometry on the shock attenuation is investigated. In Fig. 4.6 one can see that the quasi planar shock wave is stronger than the initially point-like shock wave. This is due to the fact that instead of propagating only in the axial direction of the capillary, the initially point-like shock wave propagates also towards the capillary walls and lost its energy in this direction.

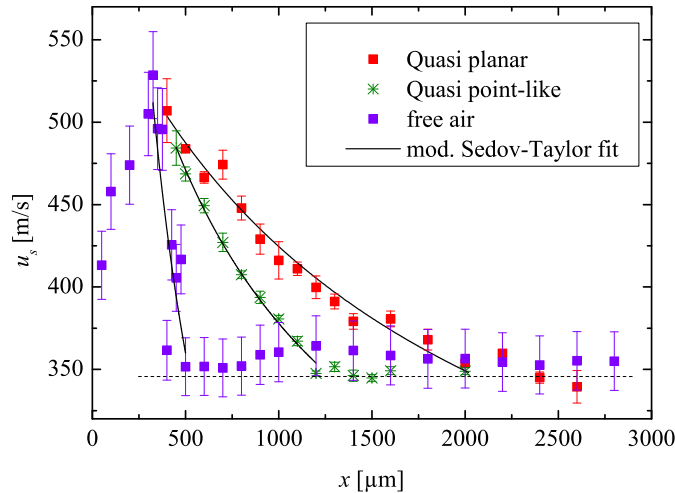


Figure 4.6: Shock wave attenuation affected by geometrical confinement from the capillary. The diagram shows the shock wave velocity u_s as a function of propagation distance x . 1. quasi planar plasma driver in a 50 μm capillary; 2. quasi point-like driver in a 50 μm capillary; 3. in free air, without a capillary. The experimental points are obtained from the time-of-flight method. Same laser energy E is applied for all geometries. Solid fit curves: modified Sedov-Taylor relations.

Fig. 4.6 shows the experimental results of shock wave attenuation affected by the geometry. As expected, for the same laser energy $E = 20 \mu\text{J}$, shock wave is strongest when it is driven by a quasi planar plasma in a capillary. Without the capillary as geometric confinement, the shock wave in free air has a spherical propagation. The pressure behind the shock front decreases rapidly. Similar as the conventionally generated shock waves, the plasma-induced shock wave also has a speed-up phase. Due to optomechanical limitations of the velocity measurements, the speed-up phase can't be resolved in the capillary. Because the interferometer beams can't come spatially closer to the shock generation spot. But in the free air, it is clearly resolved. Thanks to the geometric confinement, shock waves in the 50 μm capillary can be investigated on a total propagation distance of circa 2000 μm (after that it becomes a sound wave), which is 40 times of the capillary diameter.

Fig. 4.7 illustrates the different propagation pattern of the quasi planar and quasi point-like shock waves. The quasi planar shock wave has a very straight forward propagation

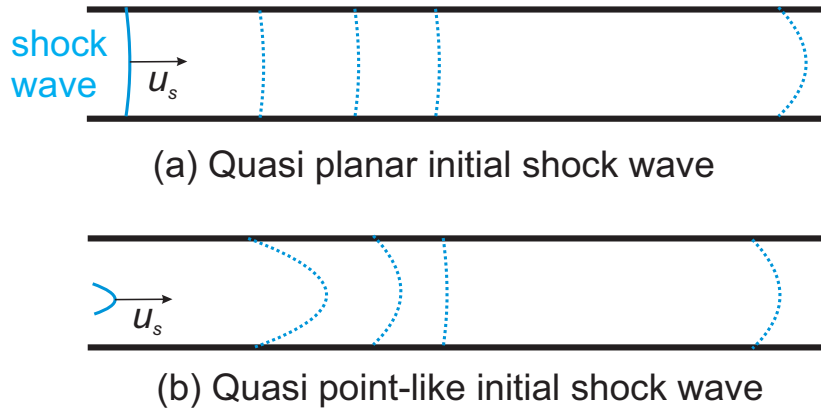


Figure 4.7: Illustration of the quasi planar and quasi point-like initial shocks.

in the axial direction of the capillary, while the point-like shock wave is expected to undergo reflections (perpendicular to the capillary axis) on the capillary walls. Due to those results, all the following experiments with different capillaries are restricted to the quasi planar geometry with the focal spot diameters and intensities shown in Tab. 4.1. It shall be remarked that even the initially planar shock wave will not be 100 % planar later on, because the friction deforms the wave front [71].

The curves in Fig. 4.6 can be fitted based on the Sedov-Taylor approach [72], where the corresponding volume expansion is modeled according to our experimental conditions (published in our paper [53]) as follows.

Case I: shock wave propagation in free air

Following Sedov-Taylor expansion approach [72], the pressure behind the shock front $P_2(x)$ is proportional to $1/V(x)$. Therefore:

$$\frac{P_2(x)}{P_2(0)} = \left(\frac{V(0)}{V(x)} \right)^{\gamma_i} \quad (4.1)$$

where γ_0 is the specific heat ratio for the initial phase with $\gamma_i = 1.2$ [72]. $\gamma = 1.4$ is the specific heat ratio for ambient air. $V(x)$ is the volume behind the shock front.

In free air, $V(x)$ is estimated from the geometry of a free expanding sphere:

$$V(x) = \frac{4}{3}\pi(r_0 + x)^3 \quad (4.2)$$

where r_0 is the radius of the equivalent initial volume behind the shock front, which is a fit parameter. It should be emphasized that the initial radius is not the radius of the plasma, because Sedov's model doesn't cover the early phase (this is the region close to the plasma where the shock wave is generated). Furthermore it should be mentioned that within the present work, the evolution of $V(x)$ is restricted to a quite simple model. A detailed simulation is beyond the scope of the current work and may be subject of future work.

From the Rankine-Hugoniot relation:

$$\frac{P_2(x)}{P_1} = \frac{2\gamma M_1^2 - \gamma + 1}{\gamma + 1} \quad (4.3)$$

where $M_1(x)$ is the shock Mach number at the distance x . P_1 is the initial test gas pressure (1 bar for ambient air).

From all the equations above, M_1 can be deduced as a function of x :

$$M_1(x) = \sqrt{\left[\left(1 + \frac{2\gamma}{1+\gamma} (M_0^2 - 1) \right) \frac{r_0}{x+r_0} - 1 \right] \frac{1+\gamma}{2\gamma} + 1} \quad (4.4)$$

where M_0 is the equivalent initial shock Mach number (here a fit parameter). r_0 mm and M_0 are fit parameters.

Case II: shock wave propagation in capillary

The volume $V(x)$ behind the shock front can be approximated by a volume consisting of a cylinder and a half sphere within the capillary:

$$V(x) = \epsilon\pi \left(\frac{D}{2} \right)^2 x + \pi \frac{2}{3} \left(\frac{D}{2} \right)^3 \quad (4.5)$$

ϵ is a fit parameter. With this estimation, the initial value $P_2(0)$ leads to $V(0) = \pi 2/3 (D/2)^3$. Note that similar to case I, $V(0)$ is the initial volume according to Sedov's model. This volume is thus a half sphere within the diameter of the capillary. From Eq. 4.1, 4.3 and 4.5 one can deduce the shock wave Mach number $M_1(x)$ as a function of the propagation distance x in the capillary:

$$M_1(x) = \sqrt{\left[\frac{1 + 2\gamma/(1+\gamma)(M_1(0)^2 - 1)^{\gamma_i}}{1 + 3x\epsilon/D} - 1 \right] \frac{1+\gamma}{2\gamma} + 1} \quad (4.6)$$

In the present experiments, the capillary is not sealed at the entrance. Therefore the shock wave also propagates towards the target and leaks into the ambient air. However, the simple fit still describes the experimental data sufficiently well.

The modified Sedov-Taylor fit is a preliminary attempt to describe our first experimental results. Wall friction and heat conduction are not considered in the fit function in Eq. 4.6. Only the expanding volume is taken into account for the shock attenuation. Therefore, Eq. 4.6 is not a model that can predict the shock propagation by given initial conditions. But it has the physical background of Sedov-Taylor expansion. In the following sections, detailed investigations of shock attenuation including the wall friction, heat conduction and expanding volume (expansion fan/waves) will be presented.

4.4 Shock wave propagation in different capillaries

This section investigates the micro shock flow propagation. Fig. 4.8 is the wave diagram of the shock waves. The diagram shows that shock waves generated with the same laser intensity in larger capillaries propagate faster than those in smaller capillaries. As expected, due to the wall friction and heat conduction, the shock wave in all capillaries attenuates to sound velocity (straight dash lines in the diagram). The positions where shocks become sound waves are $x_{sw} = 1888 \mu\text{m}$, $x_{sw} = 2707 \mu\text{m}$, $x_{sw} = 7913 \mu\text{m}$ for the capillaries with diameters 50, 100 and 200 μm , respectively. This shows stronger attenuation for smaller capillaries. Experiments with a 300 μm capillary is also performed, but the corresponding plasma (shall also be around 300 μm) is too large and becomes unsuitable for our overall optomechanics of the setup.

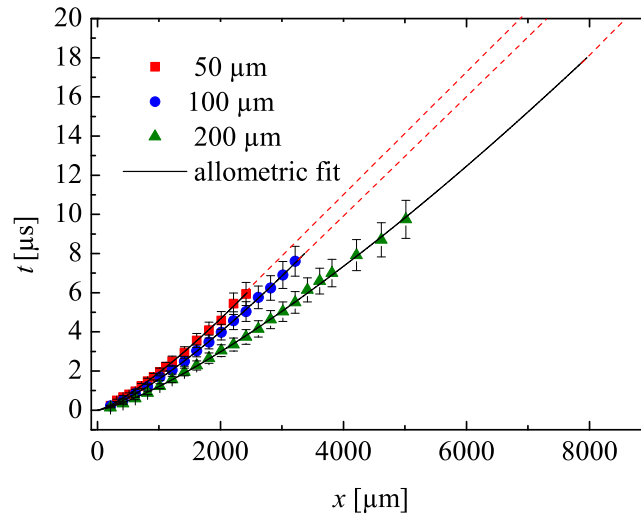


Figure 4.8: Shock wave 't-x' diagram determined by LDI. Red dash lines indicates wave propagation at sound speed. The laser intensity is the same for all experiments. Extrapolation of the 200 μm capillary is made till sound wave propagation.

When the calculation using directly measured data is inappropriate (in the sense that this may introduce large errors, specially by the derivation of fluctuating signal), it is quite common to represent the experimental data by a fit function prior to the calculations. Following this procedure, an so-called allometric function $x(t) = a \cdot t^b$ that consists only of the parameters a and b is applied for the shock wave trajectory. Simple algebraic calculations can be done using this fit function:

$$u_s(t) = \dot{x}(t) = abt^{b-1} = x(t)b/t \quad (4.7)$$

By setting $\dot{x}(t_{sw}) = u_a$ (u_a is the sound speed), the critical values t_{sw} and x_{sw} can be

obtained.

$$t_{sw} = \left(\frac{ab}{u_a} \right)^{\frac{1}{1-b}} \quad (4.8)$$

$$x_{sw} = a \cdot t_{sw}^b \quad (4.9)$$

Fig. 4.9 presents the shock wave attenuation in different capillaries. The curves show that the two different methods (either via time-of-flight or via trajectory measurements) measure the same shock velocity within the 5% error range (error analysis is made in section 3.3). However, the trajectory measurements provide higher spatial resolution, which is of particular interest for the early stage of the shock propagation (near field). Trajectory measurements have smaller steps between measurement positions (namely $\Delta x = 100 \mu\text{m}$ for the first 1000 μm propagation distance and $\Delta x = 200 \mu\text{m}$ for larger distances), while the the time-of-flight method has the step $\Delta x = 370 \mu\text{m}$.

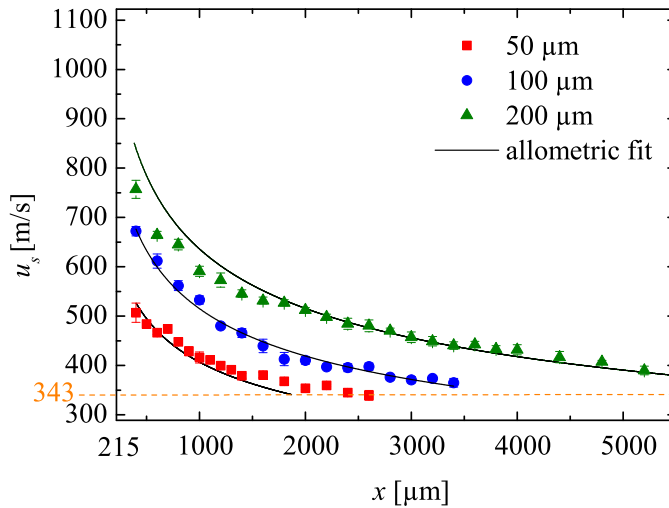


Figure 4.9: Shock velocity u_s attenuation in capillaries of different diameters. u_s is determined experimentally by the time-of-flight method.

Fig. 4.9 clearly shows that the shock waves generated with the same laser intensity in bigger capillaries are stronger than in smaller capillaries, when plotted in absolute values. This can be explained the fact that a capillary with bigger hydraulic diameter D corresponds to less wall friction and wall heat conduction than a smaller one. As already discussed in the section 2.1.4, the wall friction and heat conduction correlates with the hydraulic diameter D . To be concrete, Eq. 2.39 shows that the wall friction term of the momentum equation is $\frac{2f\rho u^2 \cdot dx}{D}$ which scales with $1/D$. Meanwhile, Eq. 2.46 shows that the wall heat conduction term of the energy equation scales with $\frac{8L_f k(T_2 - T_1)}{\rho_1 D^2 u_1}$ which scales with $1/D^2$. Consequently, a capillary with larger D correlates with higher

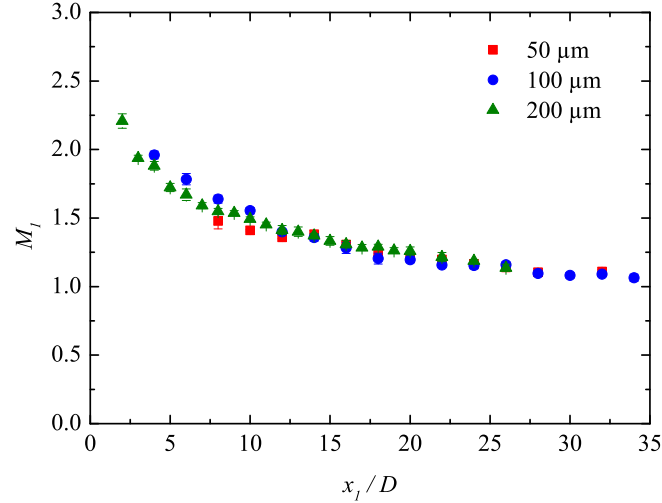


Figure 4.10: Shock Mach number $M_1 = u_s/u_a$ attenuation in capillaries of different diameters. Recalculated from Fig. 4.9.

loss in momentum and energy.

However, if the propagation distance is normalized to the capillary diameter, the shock wave Mach numbers doesn't differ significantly. (see Fig. 4.10). This becomes evident, when the shock trajectory $x(t)$ is normalized by x_{sw} and t_{sw} , respectively. Fig. 4.11 shows that the corresponding normalized shock trajectories are almost the same. From this we may state that much less laser energy (at fixed laser intensity) is needed to achieve the same shock strength (with respect to normalized values) in small capillaries than in those with larger diameter (parameters are in Tab. 4.1).

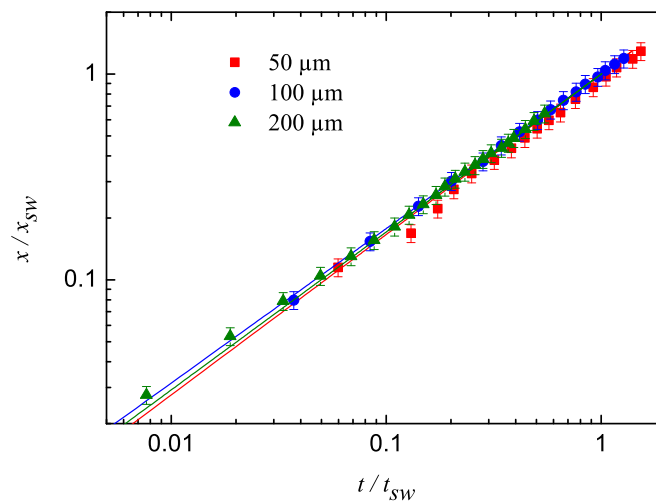


Figure 4.11: Relative trajectory derived from Fig. 4.8. Solid lines are allometric fits.

In Fig. 4.12, the development of the density jump ρ_2/ρ_1 across the shock is displayed.

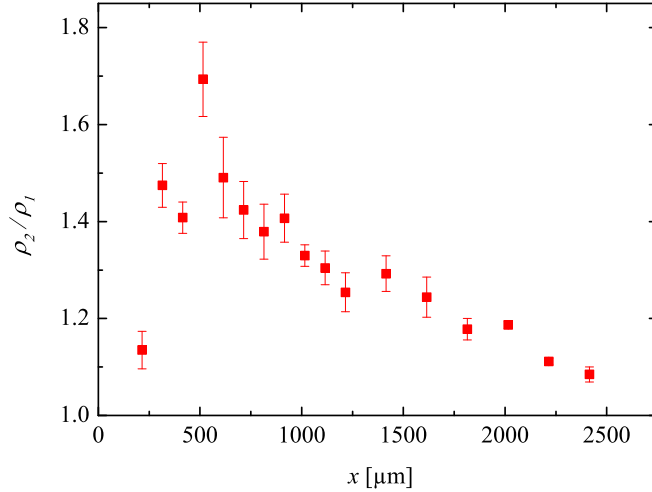


Figure 4.12: The development of the density jump across the shock in the 50 μm capillary. The error bars here correspond to the standard deviation resulted from the shot-to-shot errors.

For positions very close (here it is $x/D < 10$, regarded as near-field) to the capillary entrance where the shock onset takes place, the density jump increases with x . In the far-field (here $x/D > 10$), the expected shock attenuation process occurs i.e. the density jump decreases with x .

This behavior can be explained by the sketch in Fig. 4.13. For the near-field, the shock wave isn't very planar, yet. In this case, the LDI beam 'see' through a bend instead of a flat surface of the shock wave. This density measured by the LDI beam is actually the average density $mean(\rho)$ along the beam path in the capillary. Here $mean(\rho)/\rho_1 \neq \rho_2/\rho_1$. Therefore, the density jump is not measured correctly in the near-field. This shows the limitations for near-field measurements by LDI.

However, when it is further away ($x/D > 10$) in the far field, the shock wave becomes more planar, where $mean(\rho)/\rho_1 = \rho_2/\rho_1$. As indicated in the sketch, the beam propagates along the shock front. The measurements here show the correct results of the density jump across the shock wave.

A detailed view of the detection of the shock wave and the expansion fan are shown in Fig. 4.14. It is explained in Eq. 3.19 of section 3.1 that, the photo voltage signal $U(t)/U_0$ correlates with the flow density. The shock wave corresponds to the sharp rising and falling edges in the oscillograph trace. This curve also shows the expansion fan (indicated by the dotted circles), which causes relatively gentle density changes. The expansion fan initially propagates towards the bottom of the capillary, and then it get reflected from the target. It further follows the shock wave propagating in the same direction. This experimental observation agrees with the Navier-Stokes computations presented later in the section 4.7, which provides more information about the reflected

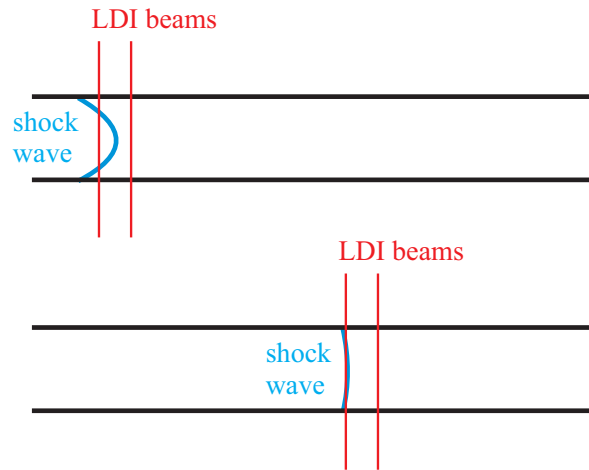


Figure 4.13: Form of the shock wave in Top: near-field (close to the onset position); Bottom: far field (fully developed, away from the onset).

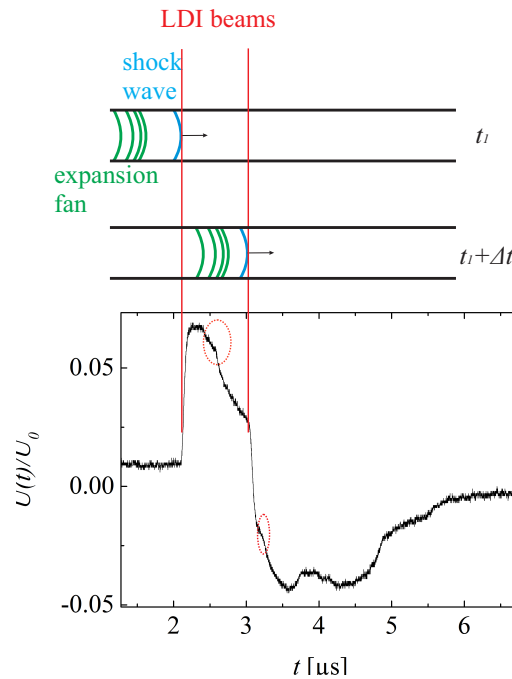


Figure 4.14: Illustration of the detection of a shock wave using the LDI. The oscillograph trace is taken at $x = 1000 \mu\text{m}$ in the $50 \mu\text{m}$ capillary. The sharp rising and falling edges are caused by the shock wave. The dotted circles highlight the expansion wave signal.

expansion fan. Moreover it can be recognized that fairly soon after the shock wave reaches the first LDI beam (but before it reaches the second one), the expansion fan also reaches the first LDI beam.

The argument about the wave form and expansion fan are further supported by Fig. 4.15, which are oscillograph traces. The figure shows that, for the curve at $x = 400 \mu\text{m}$, the first rising edge is not sharp but rather gradual. This is a typical signal, where the LDI beam sees through a curved shock front. A similar signal is observed, when the

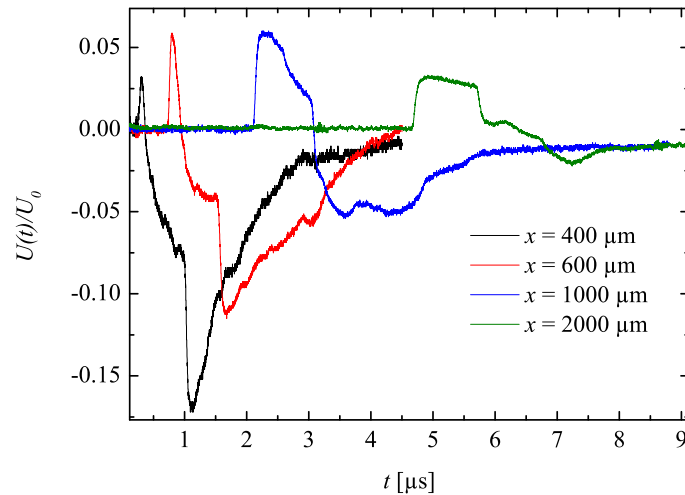


Figure 4.15: The oscillograph traces (normalized by the maximum voltage of the working range U_0) corresponding to the shock detections in the $50 \mu\text{m}$ capillary. ‘two beams in’ arrangement of the LDI

LDI measures a shock wave propagating in free air without a capillary, i.e. the shock wave propagates spherically. By a larger x , the first rising edge becomes sharper, i.e. more planar. Observe the curve $x = 600 \mu\text{m}$ (or the curve $x = 1000 \mu\text{m}$) in the figure, the signal firstly rises due to the shock wave. But immediately behind the shock wave, there is a drop in the signal. This signal drop corresponds to a drop in flow density due to the expansion fans.

4.5 Shock induced mass motion and Reynolds number

A shock wave is a pressure wave with supersonic velocity. The shock wave itself is not mass transport but a propagation of vibration. However due to its supersonic nature, the gas molecules behind the shock wave are pulled into motion by the shock wave. Therefore, mass transport can be induced by a shock wave.

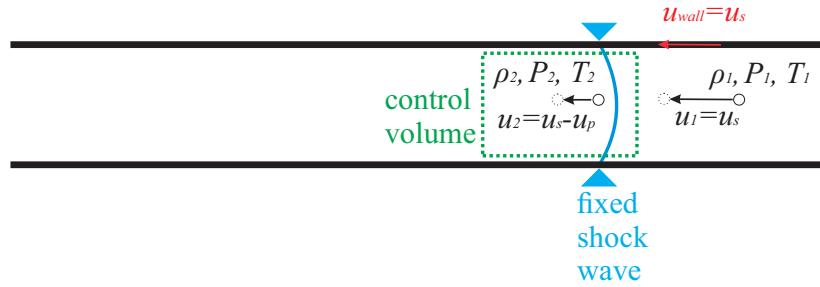


Figure 4.16: Illustration of gas propagating through a stagnate shock wave in a capillary. The shock-fixed reference system is applied.

An illustration of shock wave propagation is shown in Fig. 4.16. Instead of a lab reference frame, here a shock-fixed reference frame is applied, so that the continuity equation can be used for control volume analysis. Following [32], then the mass motion u_p can be determined by inserting the measured u_s and ρ_2/ρ_1 into the continuity equation. Note that in the shock-fixed reference system, u_1 and u_{wall} have now the value of u_s from the lab reference system (indicated in Fig. 4.16).

Apply the continuity equation:

$$(u_1 - u_p)\rho_2 = u_1\rho_1 \quad (4.10)$$

$$\Rightarrow (u_s - u_p)\rho_2 = u_s\rho_1 \quad (4.11)$$

where $\rho_1 = 1.177 \text{ kg/m}^3$ at normal conditions [73]. The right hand side of the equation describes the entrance of the control volume, the left hand side the exit.

The ratio ρ_2/ρ_1 can be obtained from the Rankine-Hugoniot relation for the fluid density ratio across the shock wave

$$\frac{\rho_2}{\rho_1} = \frac{(\gamma + 1)M_1^2}{2 + (\gamma - 1)M_1^2} \quad (4.12)$$

γ is the specific heat ratio, which is 1.4 for air.

The combination of Eq. 4.11 and Eq. 4.12 yields an equation for the calculation of the

mass motion u_p

$$u_p = u_s \left(1 - \frac{\rho_1}{\rho_2}\right) = M_1 u_a \left(1 - \frac{2 + (\gamma - 1)M_1^2}{(\gamma + 1)M_1^2}\right) \quad (4.13)$$

Inserting $M_1(x)$ (deduced from $M_1 = u_s/u_a$, with u_a as sound velocity) into Eq. 4.13. it yields u_p as a function of x (see Fig. 4.17).

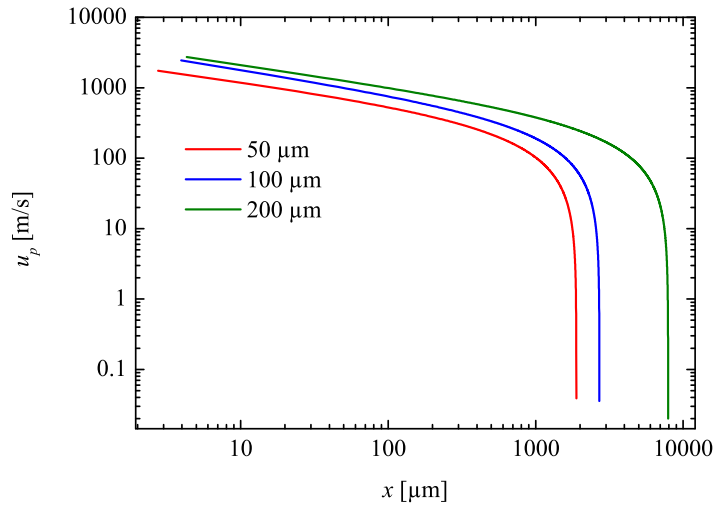


Figure 4.17: Velocity of the shock induced mass motion plotted against the propagation distance. Derived from the trajectory fit.

With the knowledge of u_p , it is possible to derive the Reynolds number for the flow. This is helpful for the analysis of the flow behavior immediately behind the propagating shock wave. Due to the large particle velocity u_p behind the shock, the mainstream flow is turbulent in conventional shock tubes with large diameters. However, the situation can change with extremely thin tubes and/or with very dilute gases, so that the flow behind the shock becomes laminar. This is indicated by the Reynolds number Re_2 ([8, 40]) for the flow field closely behind the shock wave:

$$Re_2 = u_p D \rho_2 / \mu_2 \quad (4.14)$$

Here it should be remarked that the definition of a Reynolds number Re_2 may not always be useful, if this definition is with respect to a location x where a significant boundary layer is present. However, here we define Re_2 closely behind the shock wave where boundary layer effects can be ignored. Thus Re_2 can be regarded as a useful quantity.

Since for small to moderate Mach numbers the dynamic viscosity does not depend on temperature and pressure, μ_2 can be replaced by the known viscosity $\mu_1 = 1.85 \cdot 10^{-5}$ kg/(m·s) (ambient air at room temperature 300 K) ([73]). From the combination of

Eq. 4.11, 4.12, 4.13 and 4.14, one obtains:

$$Re_2 = \frac{u_s D \rho_1}{\mu_1} \left(\frac{(\gamma + 1) M_1^2}{2 + (\gamma - 1) M_1^2} - 1 \right) \quad (4.15)$$

which can be simplified as:

$$Re_2 = Re_0 M_1 \frac{M_1^2 - 1}{0.2 M_1^2 + 1} \quad (4.16)$$

Here $Re_0 = \gamma_1 D p_1 / (u_a \mu_1)$, where γ_1 is the adiabatic exponent. Re_2 therefore only depends on the variable M_1 . As a result, a measurement of the time-dependent Mach number $M_1(t)$ yields the time-dependent Reynolds number $Re_2(t)$. This is shown in Fig. 4.18. It can be well seen that the flow behind the shock wave is turbulent for short periods only. In particular, for quite small capillaries, the laminar region is reached rather quickly. Whereas in larger capillaries, the shock propagates significantly longer (both, in space and time) in the turbulent regime. Nevertheless, at long enough x or t , the flow becomes always laminar for all capillaries. This is different with macroscopic tubes, where the propagation is nearly always in the turbulent regime.

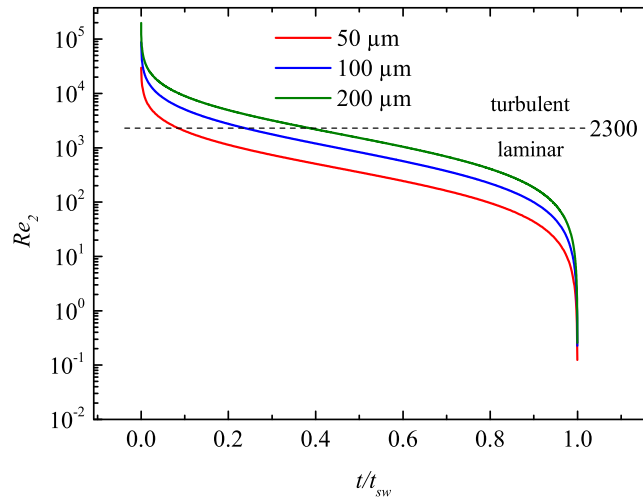


Figure 4.18: The Reynolds number Re_2 closely behind the shock front as a function of the normalized propagation time (t_{sw} is the time, when the shock wave has slowed down to sound wave velocity; see last section).

4.6 Boundary layer development after shock

The previous sections have discussed about the importance of the boundary layer behind the shock wave. In this section, the boundary layer thickness δ is estimated. The sketch in Fig. 4.19 illustrates the boundary layer behind a shock wave in a capillary. The flow velocity u inside the boundary layer as a function of the spatial coordinate y is also sketched in the figure and displayed in orange color.

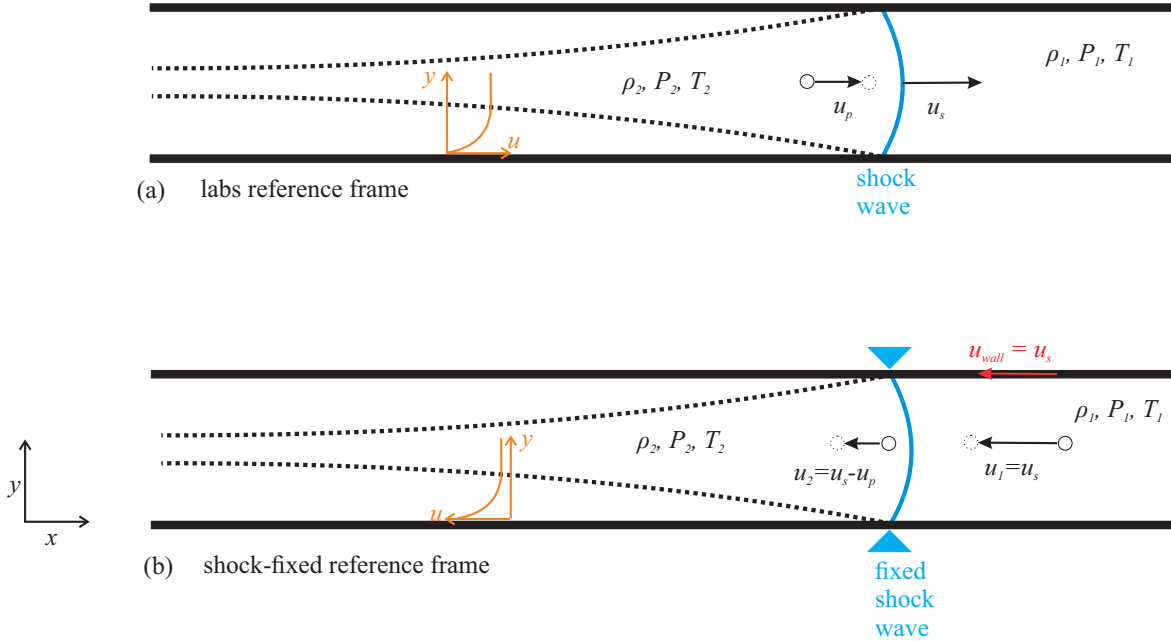


Figure 4.19: Boundary layer development in the capillary. The dash lines indicate the boundary layer thickness, while the block circle indicates an exemplar gas particle.

Mirels [36] has investigated the laminar boundary layer in shock tubes and developed the correlations formulas. His results are later on worked by Schlichting [74]. Following Schlichting's work, Mirshekari [10] used a simplified equation (refer to Eq. 4.17) to calculate the boundary layer thickness. This equation is applied in the current work.

$$\delta = 1.1\sqrt{2\nu t_1} \quad (4.17)$$

$\nu = 1.568 \text{ m}^2/\text{s}$ is the kinematic viscosity of ambient air. Knowing the trajectory of the shock waves in Fig. 4.8, the propagation time $t_1(x/D)$ can be inserted into the Eq. 4.17, thus the development of the boundary layer can be achieved and plotted in Fig. 4.20.

Observing Fig. 4.20, the boundary layer in the $50 \text{ }\mu\text{m}$ capillary can develop so much that it can fill 40 % of the capillary diameter in the end (when the shock becomes a sound wave at time instant $t_1/t_{sw} = 1$). As reported by Mirshekari and Brouillete [9, 10], the boundary layer contributes to the attenuation of micro shock waves. Therefore, the boundary layer effects are taken into consideration in the Navier-Stokes

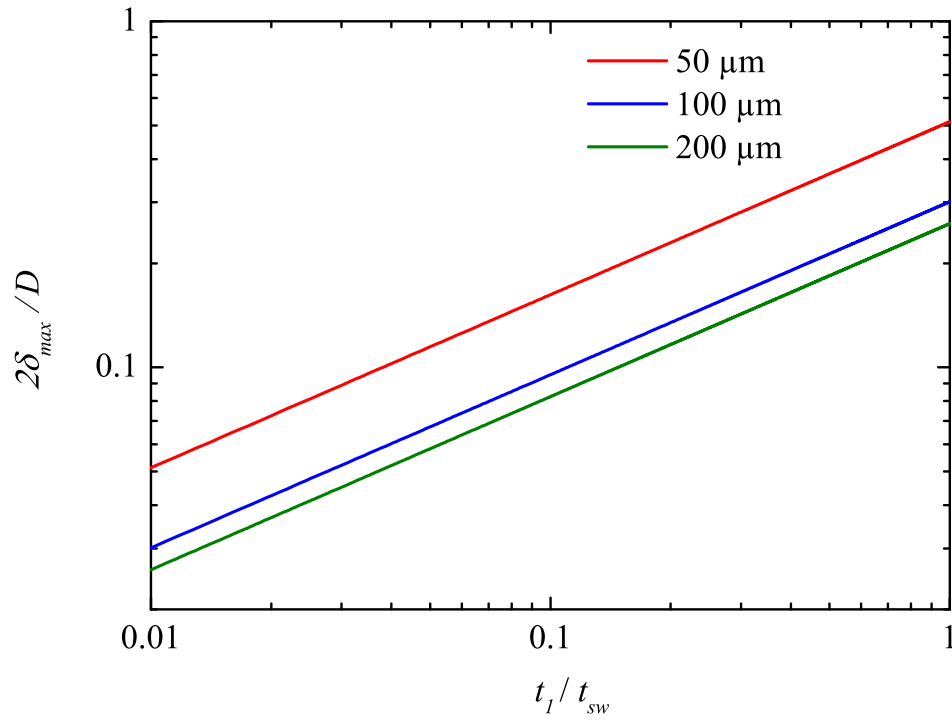


Figure 4.20: Relative maximum boundary layer thickness $2\delta/D_{max}$ in the capillary as a function of normalized shock propagation time t_1/t_{sw}

computation in section 4.7.

4.7 CFD investigations

The CFD (Computational Fluid Dynamics) investigations are done in the frame of a cooperation with Prof. David E. Zeitoun (leading role in this section) from the University of Aix Marseille. The results are published in our common paper [17].

Compressible laminar unsteady viscous flows in a micro capillary are governed by unsteady axisymmetric compressible Navier-Stokes equations coupled with the multi-species conservation equations for a mixture. This set of equations may be written in a compact integral conservative form as

$$\int_V \frac{\partial U_{NS}}{\partial t} dV + \int_S F_{NS} dS - \int_S G_{NS} dS = 0, \quad (4.18)$$

where the volume of a computational cell is denoted by V and its surface by S . The definitions of U_{NS} , F_{NS} and G_{NS} are:

$$U_{NS} = [\rho_l, \rho \vec{u}, E]^T, \quad (4.19)$$

$$F_{NS} = [\rho_l (\vec{u} \cdot \vec{n}), \rho \vec{u} (\vec{u} \cdot \vec{n}) + P \vec{n}, (E + P) (\vec{u} \cdot \vec{n})]^T, \quad (4.20)$$

$$G_{NS} = [\rho_l \vec{V}_l^d, \vec{\tau}^s, \vec{\tau}^s \cdot \vec{u} + \vec{q}^s \cdot \vec{n}]^T, \quad (4.21)$$

$$\vec{\tau}^s = \bar{\tau} \cdot \vec{n}, \quad (4.22)$$

with τ as shear stress and \vec{n} as unit vector; $\bar{\tau}$ and \vec{q}^s denote the viscous stress tensor and the heat flux vector, respectively. Quantities ρ_l , P , $\vec{u} = [u, v]^T$ and E are the density of the l species, the pressure, the velocity vector and the total energy per unit volume, respectively. \vec{u}_l^d is the diffusion velocity of the l -species. The subscript $l = 1, 2$ represents the species involved in the driven mixture.

Energy E can be calculated by the relation

$$E = \rho \left(\mathbb{U}_i + \frac{\vec{u}^2}{2} \right), \quad (4.23)$$

where \mathbb{U}_i is the internal energy per unit mass defined as

$$\mathbb{U}_i = \sum_{l=1}^N Y_l u_{i,l}(T), \quad (4.24)$$

with the mass fraction of each species, $Y_l = \rho_l / \rho$, and the density of the mixture ρ .

The specific internal energy for each species may be expressed as

$$\mathbb{U}_{i,l}(T) = \frac{3}{2}RT + \psi_l(\mathbb{U}_{rot,l}(T)), \quad (4.25)$$

with $\psi_l = 0$ for atoms or 1 for molecules.

Finally, pressure P will be determined from the Dalton law: $P = \sum_l P_l$, where P_l is the partial pressure of the l -species, assumed to behave as a perfect gas following the relation $P_l = \rho_l TR/M_l$. Here, M_l is the mass per mole of the l -species, R the universal perfect gas constant. Knowing the mass fraction of the species, their densities can be found from relations $\rho_l = \rho Y_l$.

The numerical solution of these equations is performed by using the parallel version of a multi-block finite-volume home code [75], [13] with an exact Riemann solver coupled with an AUSM-DV solver assuring second-order MUSCL extrapolation for the inviscid fluxes. The viscous and heat transfer terms are discretized using a central difference scheme. Grid cells are refined near the wall with a minimum non-dimensional y/D step equal to 10^{-2} at the wall, and the mesh size is $1000 \cdot 30$ in x, y directions. The resulting integration time step is 10^{-11} s.

As in experiments, three hydraulic diameters D are chosen equal to 50, 100 and 200 μm . The high pressure chamber of the shock tube is hard to define, because unlike the conventional shock tubes in section 2.2.2 Fig. 2.6, here the high pressure chamber doesn't have a fixed length. As a rough approximation, this high pressure chamber length is defined as 2.5 μm which is one thin layer in the numerical grid. The shock generation is simulated by the burst of an diaphragm at $t = 0$. The shock wave is immediately developed without formation length. The initial temperature in the capillary is equal to 300 K and the driven pressure P_1 is atmospheric pressure, while the driver pressure P_4 is variable.

On the solid walls, the following boundary conditions are used:

$$u = v = 0, \quad T = T_w, \quad \frac{\partial P}{\partial n} = 0,$$

where the subscript w refers to the wall quantities.

The first test case in a 200 μm diameter capillary has been computed with an initial pressure ratio $P_4/P_1 = 100$. Although this pressure is rather low when compared to the corresponding P deduced from the MULTI-fs hydrocode simulations (section 4.2), it must be stated that $P_4/P_1 = 100$ indicates the 'effective' pressure ratio for shock formation.

The pressure distribution along the center line of the capillary at different times is plotted in Fig. 4.21. The computations stop when the shock wave reaches the capillary exit ($t = 10^{-5}$ s). It can be clearly seen that the shock wave attenuates during its

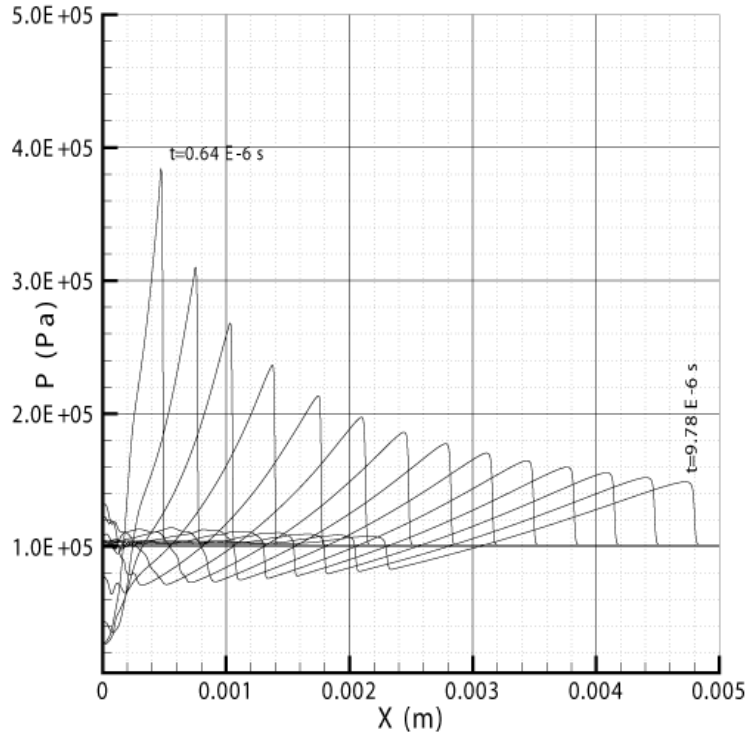


Figure 4.21: Calculated centerline pressure distribution at different times t in a 200 μm diameter capillary.

propagation along the capillary with decreasing pressure peaks. One can also see the wave expansion and its reflection at the bottom of the capillary. A secondary shock wave appears, which brings the pressure back to the atmospheric one. Between the main and secondary shock waves, the pressure decreases and thus this behavior is different to the classical shock tube, where a plateau pressure appears behind the shock wave.

In order to show the flow structure in the capillary, the axial velocity contours are drawn at three different times in Fig. 4.22.

The main and secondary shock propagation and the wall boundary layer development between them are clearly visible. The distance between these two shock waves increases with time. The intensity of the shock wave velocity along the capillary can be deduced from the computations and is plotted in Fig. 4.23. The numerical results agree well with the experimental data and tend to validate this numerical description.

The same computations have been conducted for the two other diameters 100 and 50 μm with the same mesh size. The main difference is the choice of the initial pressure ratio which has been reduced to 65 for these two cases, in order to have the best fitting with experimental data as shown in Fig. 4.24, where the influence of the initial pressure ratio is tested on the shock velocity evolution along the 100 μm diameter capillary.

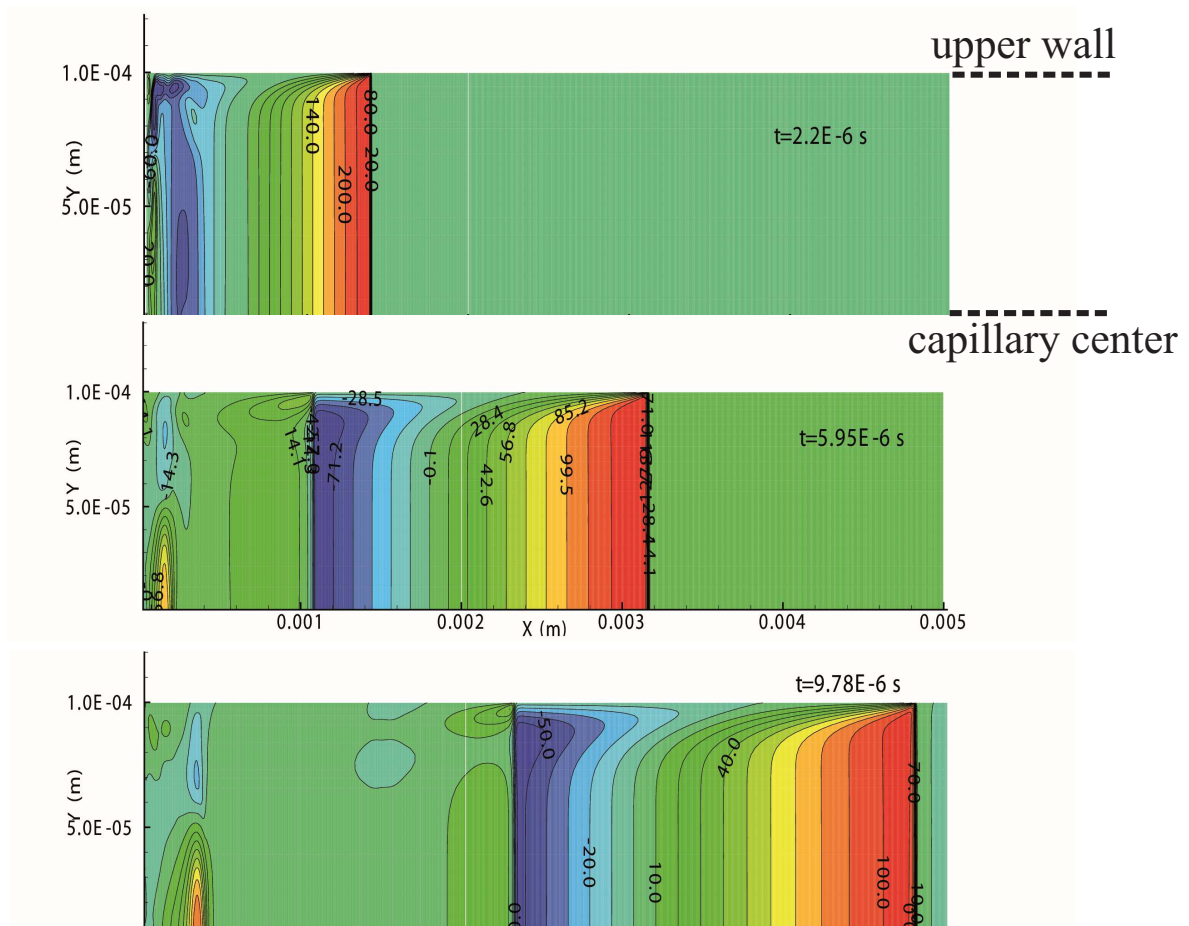


Figure 4.22: Velocity contours (m/s) at three different times in the 200 μm diameter capillary.

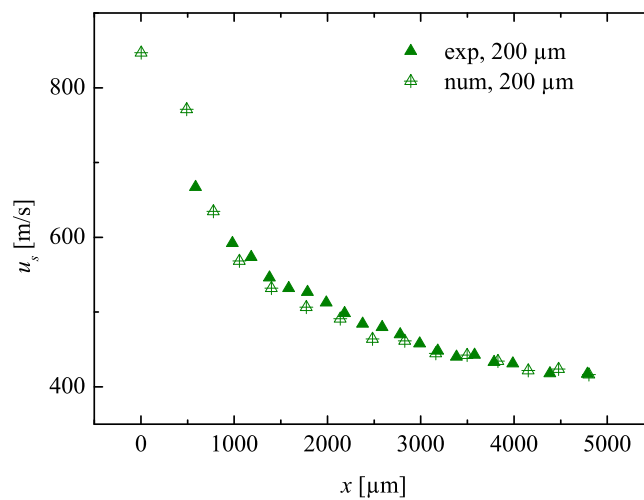


Figure 4.23: Shock wave velocity along the 200 μm capillary. Comparison of experiments (labeled exp.) and numerical simulations (labeled num.).

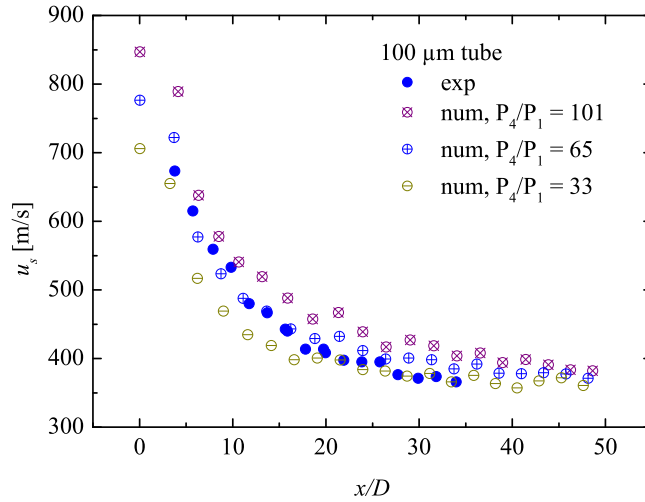


Figure 4.24: Influence of initial pressure ratio on shock wave velocity along the 100 μm capillary.

The main requirement for the appropriate choice of the initial pressure ratio is to obtain a good agreement with experimental data on the first part of the capillary (approximately 20 diameters). It can be also noted that whatever this ratio is, the shock velocity tends to the same final value (sonic value).

For the investigated three cases with different capillary diameters, the shock wave velocity along the capillary is plotted in Fig. 4.25, which shows good agreement of the numerical values with experimental data. The slope of attenuation along the capillary and the limiting values are also well described.

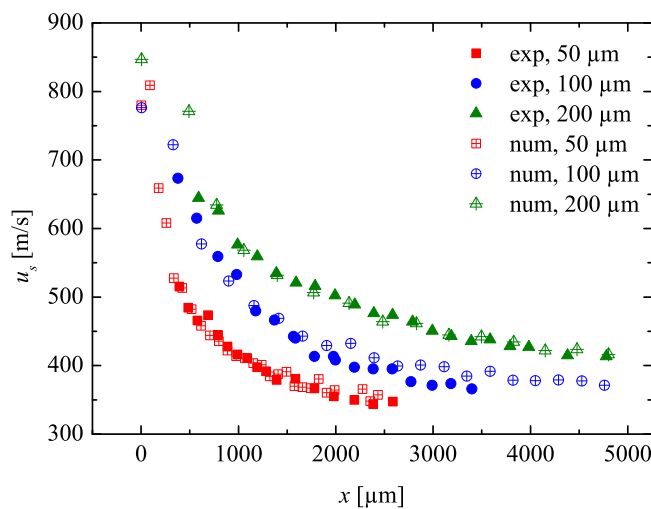


Figure 4.25: The shock wave velocity along capillaries for the three cases: 200, 100 and 50 μm diameters.

The observed behaviour of the shock wave (main) velocity decline along the capillary can be explained by two processes: the first process is the core flow expansion fan behind the created shock wave which is caused by the initial pressure ratio and a very short driver. The second process is the development of the wall boundary layer (due to viscosity) which interacts with the core flow. These two processes lead to a decrease of the shock wave velocity.

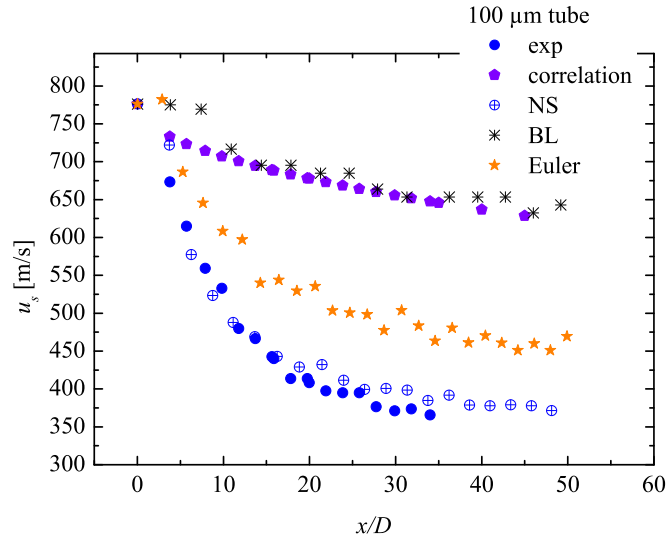


Figure 4.26: Comparison of the experimental (exp) and numerical shock wave velocity behaviour in a 100 μm capillary for different computations (correlation, Navier-Stokes, boundary layer and Euler). Published in [17].

Figure 4.26 shows the influence of each process on the shock wave attenuation. The main process is the aforementioned first process, i.e. expansion fan. The reason is that, compared to boundary layer computation (labeled BL), the Euler computation (labeled Euler) is closer to the experimental values (labeled exp). As it is well-known in fluid mechanics, the Euler equation is inviscid. As a side note, the boundary layer computation agrees with the shock-scaling factor correlation (labeled correlation, details in [14]). The Navier-Stokes computation (labeled NS) considering the expansion fan as well as the wall boundary layer has the best (among the computations presented here) agreement with the experiments.

To sum up, the propagation behaviour of shock waves in the investigated micro capillaries, where the shock wave is initially produced in a laser plasma, is mainly determined by the expansion of the flow behind the shock front along the capillary. This leads to a decrease of the shock wave density. The effect is compounded by the influence of the wall boundary layer, which interacts with the core flow and attenuates the shock wave. The whole propagation scenario is well described by solving the laminar compressible Navier-Stokes equations. This approach is confirmed by the agreement between experimental and numerical findings.

4.8 Correction of Rankine-Hugoniot relations

The goal of this section is to achieve a corrected version of the Rankine-Hugoniot-relation (RH relation, in short) by applying the control volume analysis for the shock flow. This corrected RH shall be valid for shock waves at micro scale as well as at macro scale.

It is well known in the field of nano and micro technology that, wall friction and heat transfer become more significant for smaller structures due to larger area-to-surface ratio. As stated in section 2.1.4 in Eq. 2.39 and Eq. 2.46, the friction term of the momentum equation scales with $1/D$ and heat transfer conduction term in the energy equation scales with $1/D^2$. This can make a noticeable difference between a micro and a macro shock wave, since the macro shock propagation is conventionally treated as inviscid and adiabatic. Logically, a more accurate version of Rankine-Hugoniot relations shall be now derived from the three (mass, momentaum and enegy) conservation equations containing the friction and heat conduction terms.

It must be pointed out that, here the basic path to correct the RH relations follows Brouillete [9]. Especially Brouillete [9] and Garen [40] have achieved a certain modified version of RH relation. However, there are major differences between the previous models and my model:

1. Different wall friction model. The friction model firstly concerns the plasma shock wave, which is approximately a blast wave i.e. there is no steady driver behind the shock. The contact surface exists only in the early onset stage but not in the far-field (away from the plasma influence, only fluid mechanical effects). In far field, the length where the wall friction force works on, is not the length L between the shock wave and the contact surface, but the thickness of the mass layer behind the shock. The mass layer is a layer of accumulated particles dragged by the shock wave. The thickness Δr of this mass layer is calculated by assuming a strong-explosion model originally developed by Chernyi [76] and presented in the textbook of Zel'dovich [33]. On the other side, the magnetic valve generated shock flow assimilate the conventional shock tube flow, thus its friction length is equal to the shock-contact distance L .
2. Instead of the pressure ratio as a function of density and Mach number $P_2/P_1 = f(\rho_1/\rho_2, M_1)$ by Brouillete [9], the density ratio is here derived as a function of (only) Mach number $\rho_2/\rho_1 = f(M_1)$. The density ratio and Mach number can be separately determined in the experiments of this project, that's why the theoretical function $\rho_2/\rho_1 = f(M_1)$ is of special interest here.
3. The wall friction and heat conduction terms are modeled under the assumption of Newtonian fluid and Fourier fluid, respectively. Here in this thesis, it is assumed that the post-shock flow has zero velocity and ambient temperature at the wall, while it has the highest velocity and temperature at the center (This is not the case by Brouillette,

which might simply be his writing mistakes.).

4. In the work of Garen [40], Prandtl number Pr and the scaling factor Sc are applied in the correction of RH relation. The wall friction and heat transfer, however, seem to have less weight compared to my version of the correction, which will be presented together with the experimental results later in this chapter. Unfortunately the detailed derivation of Garen's correction is not found anymore, only the final equation is available.

The following calculations are performed for the control volume CV in Fig. 4.27.

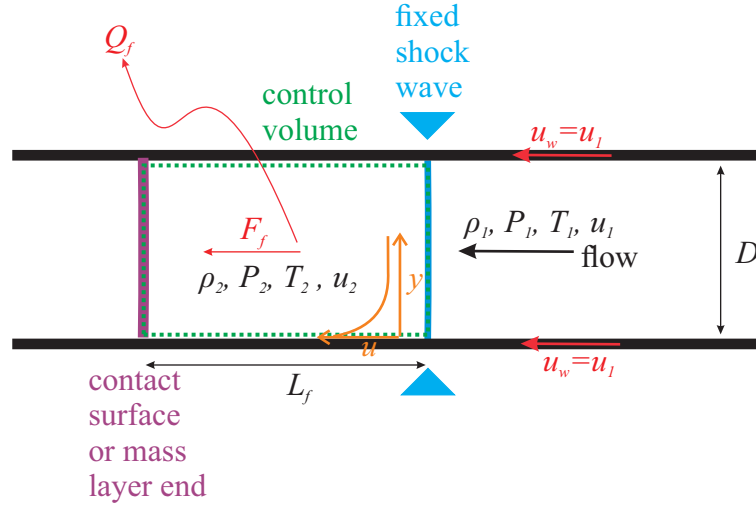


Figure 4.27: Snap-shot sketch of a shock flow in a shock-fixed reference frame. The shock front is treated as infinitely thin.

The wall friction force F_f on the control volume is the shear stress τ multiplied by the corresponding wall surface A_f of the control volume (not the flow cross-section A related to the hydraulic diameter):

$$F_f = \tau \cdot A_f \quad (4.26)$$

where the wall surface A_f of the control volume is:

$$A_f = \pi D L_f \quad (4.27)$$

L_f is the friction length.

For a Newtonian fluid, the shear stress is related with the strain rate by the relation:

$$\tau = \mu \frac{du}{dy} \approx \mu \frac{\Delta u}{\Delta y} = \mu \frac{u_{wall} - u_2}{D/2} = 2\mu \frac{u_1 - u_2}{D} \quad (4.28)$$

Here it is assumed that the flow velocity changes linearly from u_{wall} at the wall to u_2 at the geometrical center of the flow. The wall friction force can be derived from Eq. 4.26, 4.27 and 4.28 as:

$$F_f = 2\mu(u_1 - u_2)\pi L_f \quad (4.29)$$

The equation above is a linear approximation. In reality, the flow velocity is of course not a linear function of spatial coordinate y , but rather a distribution depending on the turbulent or laminar characteristics of the post-shock flow field (indicated in Fig. 4.27 in orange color).

The continuity equation (mass conservation equation) for the main stream flow in the control volume is:

$$\frac{\partial \rho}{\partial t} + \nabla(\rho \vec{u}) = 0 \quad (4.30)$$

Quasi-steady assumption for the CV is applied. This is legitimate, because there is no flow through the side walls i.e. the mass coming in through the right side of the CV goes out through the left side of the CV. Therefore, there is approximately no mass accumulation in such a small CV so that the flow is quasi-steady over a short time interval dt . Note that, the boundary layer growth in the small CV is neglected. The continuity equation can be thus brought to the simplified form as:

$$\boxed{\rho_1 u_1 = \rho_2 u_2} \quad (4.31)$$

$$\Rightarrow \tau = 2\mu \frac{u_1 - u_2}{D} = 2\mu \left(1 - \frac{\rho_1}{\rho_2}\right) \frac{M_1 u_a}{D} \quad (4.32)$$

The wall friction term is now added into the momentum conservation equation. The gravitational term can be neglected, because the flow has approximately the same height in region 1 and region 2. There is thus:

$$\boxed{P_1 A - P_2 A + F_f = (\rho_2 A u_2) u_2 - (\rho_1 A u_1) u_1} \quad (4.33)$$

Similar as the derivation of the ideal Rankine-Hugoniot relation (stated earlier in section 2.2.1), the combination of the sound velocity equation $u_a = \sqrt{\gamma RT} = \sqrt{\gamma P/\rho}$, the continuity equation, Eq. 4.26, Eq. 4.32 and Eq. 4.33 delivers the shock induced pressure jump:

$$\frac{P_2}{P_1} = 1 + \gamma M_1^2 \left(1 - \frac{\rho_1}{\rho_2}\right) + \frac{8L_f \mu M_1 \gamma}{\rho_1 D^2 u_a} \left(1 - \frac{\rho_1}{\rho_2}\right) \quad (4.34)$$

Notice that, the viscosity μ starts to appear in this pressure jump equation. Compare to Eq. 2.56 derived for the inviscid flow, where μ was not considered.

As the next step, the energy conservation shall be considered here. As shown in Eq. 2.41 of section 2.1.4, Q_f has the following form under Fourier's law for thermal conduction:

$$Q_f = -\frac{8L_f k (T_2 - T_1)}{\rho_1 D^2 u_1} \quad (4.35)$$

Now we insert \mathcal{Q}_f and W_f (friction work per unit mass flow rate) into the energy conservation equation, which can be formulated as energy input = energy output:

$$\dot{m}\left(U_1 + \frac{P_1}{\rho_1} + \frac{u_1^2}{2}\right) + \dot{m}W_f = \dot{m}\left(U_2 + \frac{P_2}{\rho_2} + \frac{u_2^2}{2}\right) - \dot{m}\mathcal{Q}_f \quad (4.36)$$

The total work done by the wall friction to the control volume is zero. Because work = force times distance, where the distance is zero under the assumption of no-slip condition. When $W_f = 0$, the energy equation becomes:

$$\boxed{\Rightarrow \left(h_1 + \frac{u_1^2}{2}\right) = \left(h_2 + \frac{u_2^2}{2}\right) - \mathcal{Q}_f} \quad (4.37)$$

Now we insert the enthalpy $h = c_p T$ into the Eq. 4.37. After applying the sound velocity equation $u_a = \sqrt{\gamma RT} = \sqrt{\gamma P/\rho}$ and the ideal gas law, we can again derive the shock induced pressure jump, but this time from the energy conservation equation:

$$\begin{aligned} \frac{P_2}{P_1} = \left(\frac{\rho_1}{\rho_2}\right)^{-1} \frac{D^2 u_1 c_p}{(D^2 u_1 c_p + 8L_f k/\rho_1)} \left(1 + \frac{M_1^2(\gamma - 1)}{2} \left[1 - \left(\frac{\rho_1}{\rho_2}\right)^2\right]\right) \\ + \frac{8L_f k}{\rho_1 D^2 u_1 c_p + 8L_f k} \cdot \left(\frac{\rho_1}{\rho_2}\right)^{-1} \end{aligned} \quad (4.38)$$

Equate Eq. 4.34 and Eq. 4.38, we can achieve the density ratio as a function of the shock wave Mach number. It gives the corrected Rankine-Hugoniot relation, which takes wall friction and heat conduction into account:

$$\boxed{\frac{\rho_2}{\rho_1} = \frac{M_1 16kL_f(8\gamma L_f \mu + D^2 M_1 u_a \gamma \rho_1) + M_1^2 c_p D^2 u_a \rho_1 (16\gamma L_f \mu + D^2 M_1 u_a \rho_1 (1 + \gamma))}{D^2 u_a \rho_1 \cdot (16kL_f + c_p D^2 M_1 u_a \rho_1 (2 + M_1^2(\gamma - 1)))}} \quad (4.39)$$

Eq. 4.39 presents the (preliminary) corrected RH relation under the following assumptions 1. planar shock wave. 2. Newtonian fluid. 3. laminar flow. 4. negligible mass sink effect in the boundary layer. The assumptions are still many, but at least the dissipative effects are considered. This equation may be applied for (1) a blast wave such as the plasma shock and (2) a conventional or quasi conventional shock wave driven by a high pressure gas.

In case of a blast wave, there is $L_f = \Delta r$, which is the thickness of the mass layer behind the blast wave [76]:

$$\begin{aligned} xD^2 \rho_1 = \rho_2 D^2 \Delta r \\ \Rightarrow \Delta r = x \frac{\rho_1}{\rho_2} \approx x \frac{\gamma - 1}{\gamma + 1} \end{aligned} \quad (4.40)$$

In case of a (quasi) conventional shock, insert $L_f = L$, which is the length between the shock wave and the contact surface.

We expect, when there is no wall friction and no heat transfer, the corrected RH shall be the same as the ideal RH. As a test, we can simply insert $\mu = 0$, $k = 0$ and $L_f = 0$ into Eq. 4.39. It leads to:

$$\frac{\rho_2}{\rho_1} = \frac{0 + M_1^2 c_p D^2 u_a \rho_1 (0 + D^2 M_1 u_a \rho_1 (1 + \gamma))}{D^2 u_a \rho_1 \cdot (0 + c_p D^2 M_1 u_a \rho_1 (2 + M_1^2 (\gamma - 1)))} = \frac{(\gamma + 1) M_1^2}{2 + (\gamma - 1) M_1^2} \quad (4.41)$$

It shows that the corrected RH is indeed consistent with the ideal RH (Eq. 2.65).

Eq. 4.39 has a rather complicated form, no wonder why the classical physicists would like to neglect the wall friction and heat transfer. The following section will examine the plausibility of the corrected RH both by Matlab simulation and comparison with experiments.

4.9 Verification of the corrected Rankine-Hugoniot

Comparison with simulation

In order to check the plausibility of the corrected Rankine-Hugoniot relation in Eq. 4.39, simulations are made for the laser plasma induced micro shock wave (LIMS). The initial conditions for the simulation are the parameters a and b of the allometric fit of the shock wave trajectory. Earlier sections have shown that this fit can well describe the experimental values. To start the simulation, only the values of a and b must be given firstly. The allometric fit is defined as:

$$x(t) = a \cdot t^b \quad (4.42)$$

The shock wave Mach number M_1 is thus:

$$M_1 = u_s(t)/u_a = \dot{x}(t)/u_a = abt^{b-1}/u_a = x(t)b/(tu_a) \quad (4.43)$$

In the following simulations, the fit parameters a and b of the trajectory are taken from the corresponding experiments [17].

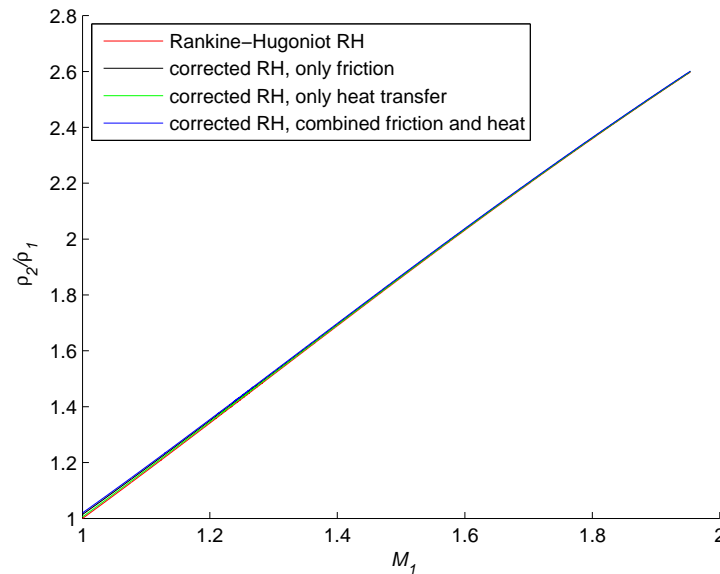


Figure 4.28: Matlab simulation of the density jump for LIMS in the 200 μm capillary.

In Fig. 4.28, 4.29 and 4.30, the simulated curves using the corrected RH relation are compared with the curves of the original (or say, ideal) Rankine-Hugoniot relation. In the case of a bigger capillary, especially the 200 μm capillary, the corrected RH curve and the ideal RH curve have little difference. In the case of the 100 μm capillary, this difference becomes noticeable. The difference becomes obvious (above 5% difference for $M_1 < 1.2$) by the 50 μm capillary. This fulfills our expectation, because the wall

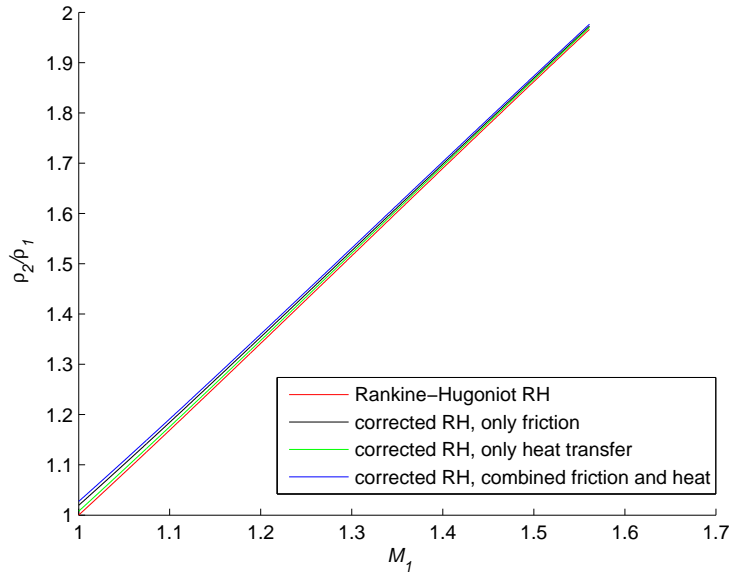


Figure 4.29: Matlab simulation of the density jump for LIMS in the 100 μm capillary.

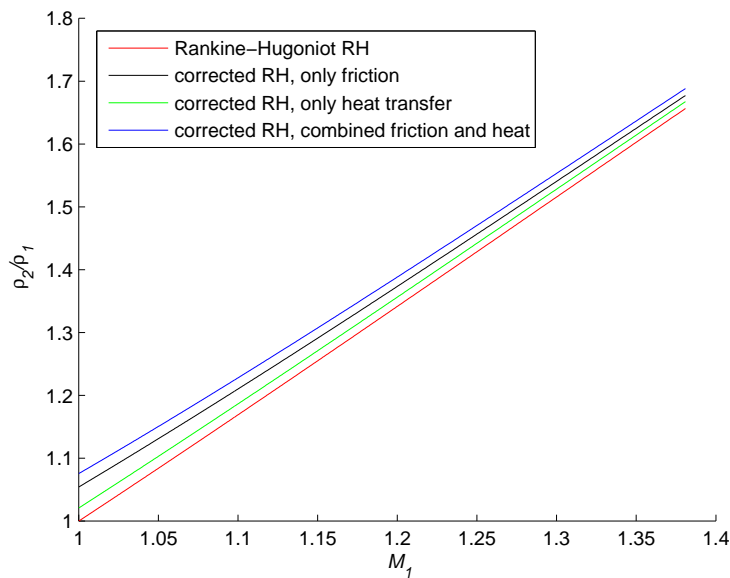


Figure 4.30: Matlab simulation of the density jump for LIMS in the 50 μm capillary.

friction and heat transfer shall play a bigger role by even smaller capillaries.

Furthermore, in all three simulation figures, the corrected RH (only) with friction term lies higher than the corrected RH (only) with heat transfer term. Observe Fig. 4.30, the curve ‘corrected RH, only friction’ lies higher than ‘corrected RH, only heat’, thus much closer to ‘corrected RH, combined friction and heat’. Because, as stated before, the wall friction scales with $1/D$ and the heat transfer scales with $1/D^2$. So, the wall friction effect is more significant than wall heat transfer, but the heat transfer scales faster with the diameter than friction does.

Comparison with experiments

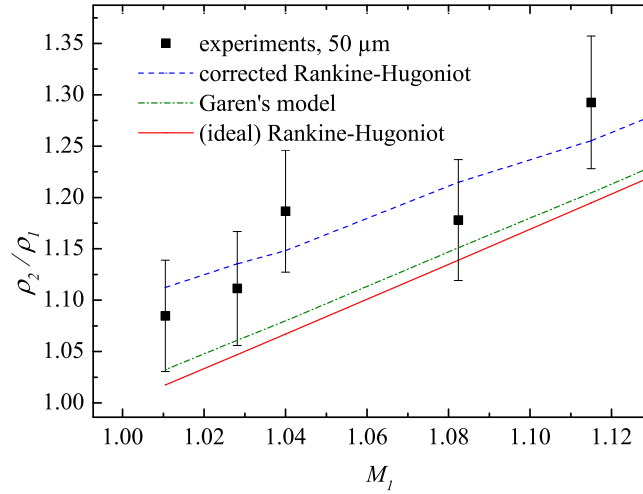


Figure 4.31: Density jump across the plasma shock wave as a function of the shock Mach number in the 50 μm capillary.

In Fig. 4.31, the ideal RH (Eq. 2.65), Garen's model [40] and the corrected RH from me (Eq. 4.39 combined with 4.40) are plotted together with experimental results for the 50 μm capillary. It shows that, the corrected RH from me fits the experiment better than the ideal RH. Furthermore, the curve of the corrected RH has the tendency to lay higher than the ideal RH at smaller M_1 . This tendency generally agrees (inside the error bars which are no more than 5 %) with the simulation in Fig. 4.30. Of course, the assumptions (stated in the last section) applied in the corrected RH relation set the limitations of its usage. It is important to notice that Garen's model also lays higher than the ideal RH, although it might underestimate the wall friction and heat conduction. Here is Garen's model:

$$\frac{\rho_2}{\rho_1} = \frac{(\gamma_1 + 1)M_1^2 + 2\gamma_1 M_1 / (Pr \cdot Sc) + (1/Sc)^2 2\gamma_1 / Pr}{(\gamma_1 - 1)M_1^2 + (1/Sc)2 / (M_1 Pr) + 2} \quad (4.44)$$

with Prandtl number $Pr = c_P \mu / k$, i.e. viscous diffusion rate divided by thermal diffusion rate.

To be scientifically correct, more experiments are needed in the future for comparison. Specially interesting are the capillaries smaller than 50 μm in diameter. In those experiments, the corrected and the ideal RH are expected to demonstrate more significant difference.

From the viewpoint of the Knudsen number Kn (stated in section 2.2.4), the corresponding Kn for shock in the 50 μm capillary is slightly more than $1 \cdot 10^{-3}$, which is at the beginning of the slip-flow regime as indicated in Fig. 2.10. The corresponding Kn of the shock in the 100 μm or 200 μm capillary is, however, around 10^{-4} laying in

the no-slip regime. This viewpoint may also roughly explain why the ideal RH doesn't apply for the 50 μm case, but it applies for the 100 μm or 200 μm case.

Chapter 5

Results of micro shock flow

This chapter presents the results of the micro shock flow generated by the magnetic valve. A micro shock flow indicates a whole micro shock flow system including shock wave, boundary layer, contact surface and the expansion fan (sketched in Fig. 5.1). A plasma induced shock wave only has a contact surface at the onset stage, but not in the experiment range in far field. Therefore, the plasma shock waves are not considered in this chapter.

The main setup applied in this chapter is the valve setup presented in section 3.4. Except section 5.8, which uses the setup in section 3.2 for control purpose.

The major findings of this chapter are published in [77]. Compared to the paper, additional details (sections 5.8, 5.1 and 5.2) are given here in the thesis .

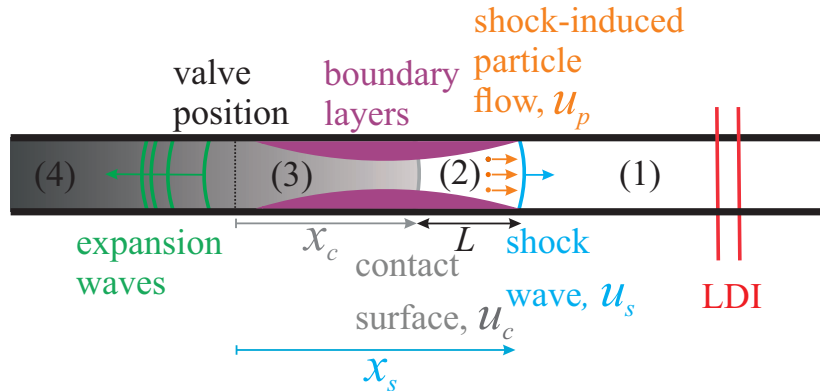


Figure 5.1: A snap-shot like illustration of a micro shock flow in a capillary. Region (1) is in front of the shock, region (2) is between shock and contact surface, region (3) is between contact surface and expansion waves, region (4) is the high pressure driver. Default setting is $P_4 = 8$ bar He, $P_1 = 1$ bar air at normal conditions, otherwise special comments are given.

Fig. 5.1 shows that the valve generated micro shock flow can be divided into 4 regions (similar to a conventional shock tube). Every region corresponds to certain state variables such as pressure, flow velocity, density temperature etc. In this work, the

state variables are indicated by subscripted indices according to the region (e.g. P_4 is the pressure of the region (4)).

The main diagnostic is the LDI, while the Schlieren photography serves as a control (only in section 5.8). The variables to be experimentally determined and presented in this chapter are indicated in Fig. 5.1, i.e. shock wave propagation distance x_s , contact surface propagation distance x_c , shock wave velocity u_s , contact surface velocity u_c , post-shock particles flow velocity u_p and post-shock flow density ρ_2 . The notation x without a subscript simply means propagation distance.

5.1 Micro shock wave formation mechanism

This section investigates the formation mechanism of the shock wave. It is well known that a shock wave is being build up by following compression waves in the early phase. But how long is this formation phase in our experiments? This section shall clarify this question. Fig. 5.2 shows the raw data measured by the ‘two beams in’ arrangement of the LDI (sketched in Fig. 3.6). The time $t = 0$ corresponds to the start of the valve opening (served as trigger signal). After the rise time $t_r = (170 \pm 10) \mu\text{s}$, the valve fully opens up. From $x = 140 \text{ mm}$ (or $t > 600 \mu\text{s}$) till 260 mm , the density jump (represented by the normalized photo voltage jump) of the shock wave experiences the linear attenuation process, which is indicated by the dash line in Fig. 5.2. The point $x = 270 \text{ mm}$ is not included in the dash line, because at the point the shock wave has already converted to a sound wave, thus no more ‘shock’ attenuation.

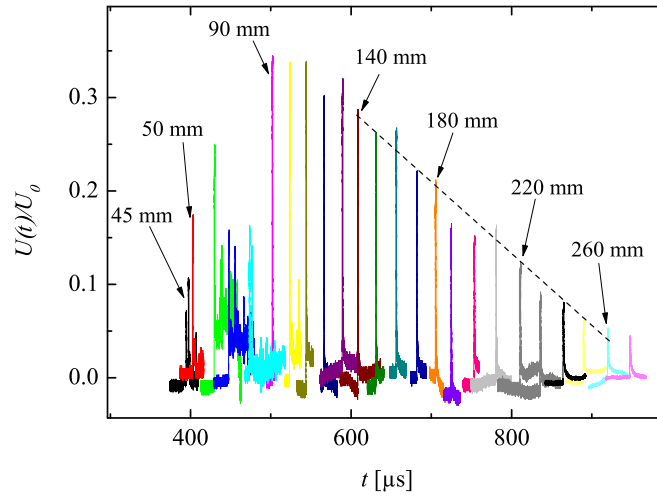


Figure 5.2: Shock wave measurements in the $200 \mu\text{m}$ capillary at different propagation distances x . ‘two beams in’ arrangement of the LDI. $P_4 = 8 \text{ bar He}$, $P_1 = 1 \text{ bar air}$.

The range $0 < t < 500 \mu\text{s}$ appears to be a formation phase of the shock wave. In this phase, the density jump varied strongly with propagation time. The uncertainties are surveyed by taking a closer look at each density profile in the following.

Fig. 5.3 is a zoomed-in view of Fig. 5.2 for $x = 45 \text{ mm}$ (i.e. $225 \text{ times } D$). Partial shocks or called compression waves are visible and they run up successively with higher speed. A following compression wave is faster than its front-runner, for the reason that the front-runner creates better conditions, e.g. higher temperature for the follower. The higher temperature behind each compression wave is a result of the compression. Some of the following compression waves eventually catch up with the front-runner and then combine as a shock front with sharp density/voltage jump at the point $x = 50 \text{ mm}$ (Fig. 5.4). Note that even at $x = 50 \text{ mm}$, some rest of the trailing compression

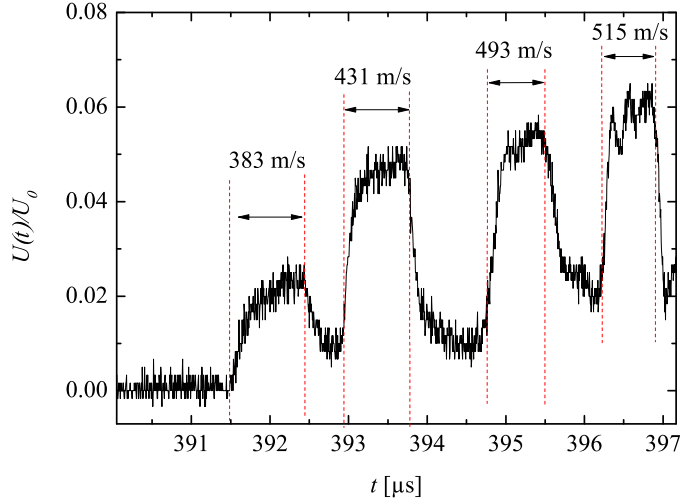


Figure 5.3: Compression waves (partial shock waves) in the 200 μm capillary at $x = 45$ mm. ‘two beams in’. $P_4 = 8$ bar He, $P_1 = 1$ bar air.

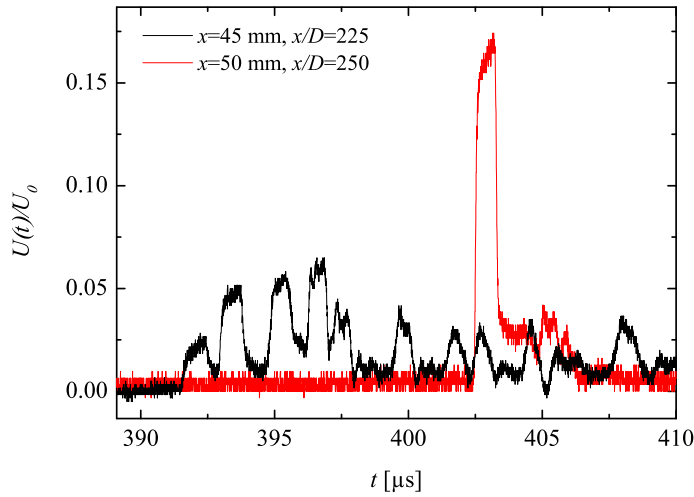


Figure 5.4: Micro shock waves in the 200 μm capillary at $x = 45$ mm and $x = 50$ mm. ‘two beams in’. $P_4 = 8$ bar He, $P_1 = 1$ bar air.

waves are still visible. The compression waves are already influenced by the capillary wall friction, which causes the boundary layer growth (indicated by the subtle density increase after the shock passage). The valve rise-time is expected to affect the length of the formation process. Here we use a characteristic length x^* as approximation, which is the sound velocity u_a times the valve rising time t_r :

$$x^* = u_a t_r \quad (5.1)$$

For $t_r = 180 \mu\text{s}$, there is $x^* = 61.2$ mm. This means, the formation process needs

a propagation length of at least 61.2 mm. This is approximately the case, because when x below 60 mm, the compression waves are clearly visible. For $x \geq 90$ mm, the trailing compression waves are not to be seen at all, thus the formation phase shall then be completed with certainty. Besides the shock formation due to trailing compression waves, there is disturbances caused by the small mismatch of the valve orifice (500 μm) and the capillary diameter (200 μm). Due to the diameter mismatch, vortices can be generated at the capillary entrance. Therefore, the shock wave is not fully developed at smaller x . Similar situation also occurs in the works [11] and [15], where the mismatch is much more significant, since they connect a macro shock tube with a micro or mini tube. All together, the range $x \geq 90$ mm is experimentally determined to be a suitable range for further experiments in the 200 μm capillary.

5.2 Initial pressure and dimensional effects

This section discusses about the scaling effects related to different initial pressure and different diameter.

In Fig. 5.5, the micro shock velocity is measured by the time-of-flight method using the ‘two beams in’ arrangement of LDI.

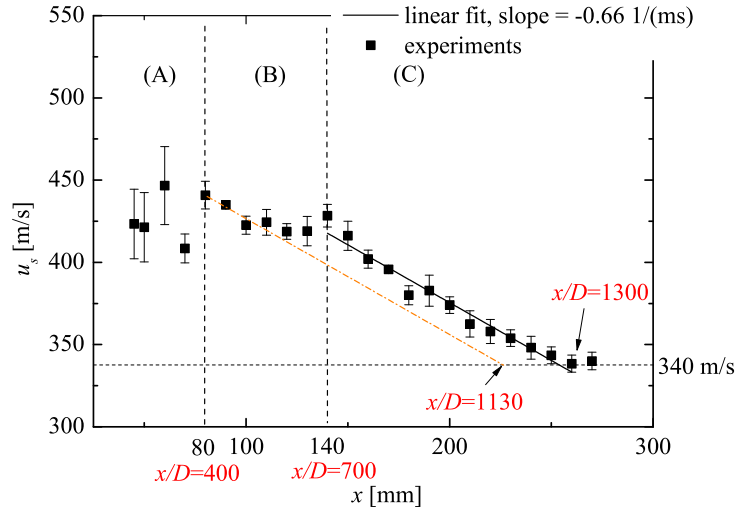


Figure 5.5: Micro shock propagation in the 200 μm capillary. The shock velocity u_s is plotted against the distance x between the valve and the detection spot. Normalized values are displayed in red for special positions. $P_4 = 8$ bar He, $P_1 = 1000$ mbar air. Measured by the ‘two beams in’ arrangement.

The figure shows three different phases: (A) shock formation; (B) changing attenuation; (C) quasi linear attenuation.

When the pressure of the driven gas P_1 is set to a lower value, the flow phases are strongly affected. Fig. 5.6 shows that, when $P_1 = 500$ mbar, only the formation phase (labeled as phase A) and linear attenuation (labeled as phase C) are measurable. One step further, when P_1 is lowered to 200 mbar, only phase (C) is visible as shown in Fig. 5.7. The formation phase shall theoretically always exist, but the experiments show that it becomes shorter with lower P_1 . The corresponding formation length is even shorter than 45 mm, which is the optomechanical limit of our setup.

As the next step, the dimensional effects on shock attenuation are investigated.

It can be seen in Fig. 5.8 that, the shock wave in the 200 μm capillary attenuates clearly stronger than in the 300 μm capillary. Note that we compare only the linear attenuation range. The stronger attenuation is caused by larger wall friction and heat conduction due to the higher area-to-volume ratio.

The attenuation slopes of the shock attenuation influenced by the scaling effects are summarized in Tab. 5.1.

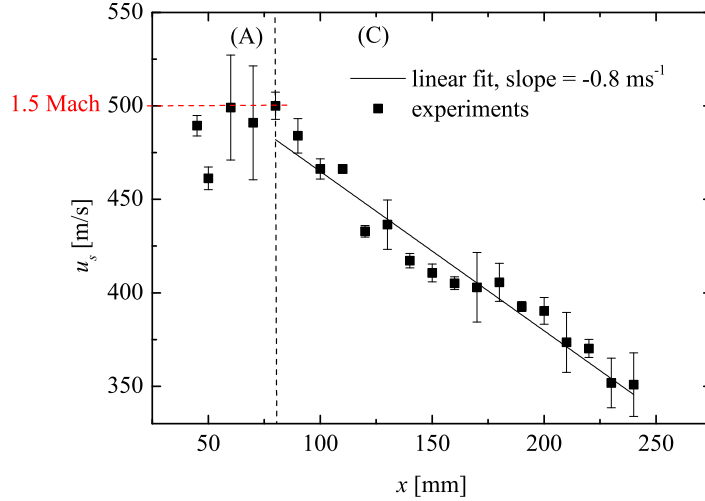


Figure 5.6: Micro shock propagation in the 200 μm capillary. ‘two beams in’. $P_4 = 8$ bar He, $P_1 = 500$ mbar air.

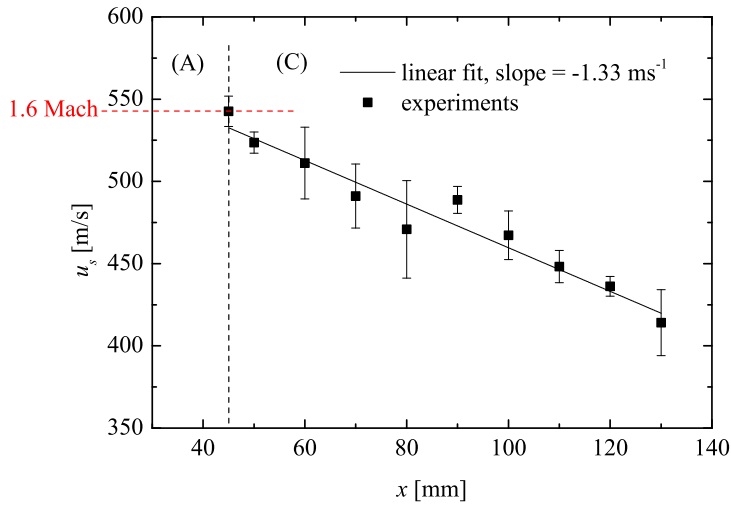


Figure 5.7: Micro shock propagation in the 200 μm capillary. ‘two beams in’. $P_4 = 8$ bar He, $P_1 = 200$ mbar air.

	slope in ms^{-1} , 200 μm capillary	slope in ms^{-1} , 300 μm capillary
$P_1 = 1000$ mbar	-0.66 ± 0.05	-0.38 ± 0.05
$P_1 = 500$ mbar	-0.80 ± 0.05	–
$P_1 = 200$ mbar	-1.33 ± 0.05	–

Table 5.1: Slopes of the shock attenuation in the 200 μm and 300 μm capillaries. Data retrieved from Fig. 5.5, 5.6, 5.7 and 5.8. $P_4 = 8$ bar He, variable P_1 of air.

In Tab. 5.1 shows that lower initial pressure P_1 of the driven gas corresponds to steeper attenuation slope, which means stronger attenuation. Theoretically, the higher is the pressure ratio P_4/P_1 , the higher shall be the initial shock Mach number (or velocity)

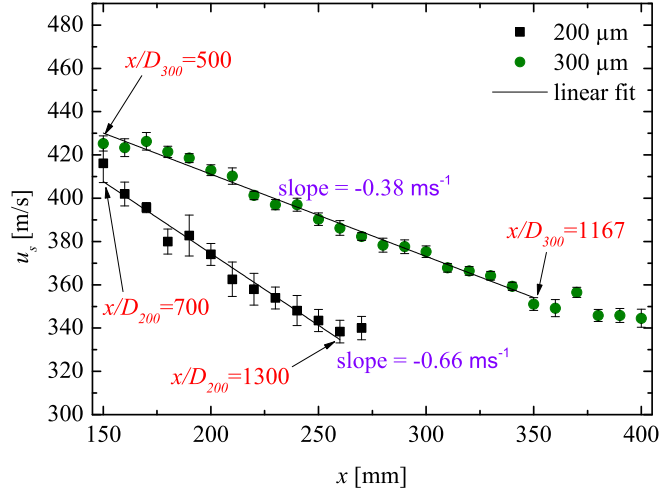


Figure 5.8: Micro shock propagation in the 200 μm and 300 μm capillaries. The range $x > 140$ mm is chosen for comparison, because both shock waves have linear attenuation here ('far field'). 'two beams in'. $P_4 = 8$ bar He, $P_1 = 1$ bar air.

	$M_{1,i}$, 200 μm capillary	$M_{1,i}$, 300 μm capillary
$P_1 = 1000$ mbar	1.3 ± 0.1	1.3 ± 0.1
$P_1 = 500$ mbar	1.5 ± 0.1	–
$P_1 = 200$ mbar	1.6 ± 0.1	–

Table 5.2: Initial shock Mach number $M_{1,i}$. Data retrieved from Fig. 5.5, 5.6, 5.7 and 5.8. $P_4 = 8$ bar He, variable P_1 of air.

[32]. This is indeed the case for the 200 μm capillary with different P_1 (thus different P_4/P_1 because of constant P_4) shown in Tab. 5.2.

Moreover, at the very beginning of the shock generation, the friction doesn't play a role yet. Therefore, the initial shock Mach number $M_{1,i}$ shall only be determined by P_4/P_1 , and independent of the capillary dimension D . Tab. 5.2 shows that this expectation is also fulfilled, since both the 200 μm and 300 μm capillaries have the same $M_{1,i} = 1.3$ for the same P_4/P_1 .

5.3 Driver pressure variation

This section is published in [53]. This section investigates the relation between the driver pressure and the shock velocity (or Mach number). For a macroscopic shock tube operating at the same conditions as ours, its performance can be well estimated through the so-called shock tube relation.

Due to technical reasons in this project (mainly due to the pressure regulator on the gas bottle), the nitrogen as driver can be regulated in a broader pressure range than by helium. Therefore, nitrogen is used as driver in this section. The Nitrogen driver is set in the range $8 \text{ bar} < P_4 < 20 \text{ bar}$.

As written in the text book of Anderson [32], the inviscid theory gives an ideal relation (ideal model) between P_4/P_1 and P_2/P_1 . Furthermore P_2/P_1 correlates with shock Mach number M_1 through the ideal Rankine-Hugoniot relation. Therefore, the relation between the driver/driven pressure ratio P_4/P_1 and shock Mach number M_1 can be displayed as:

$$\left(\frac{P_4}{P_1}\right)_{ideal} = \left[1 + \frac{2\gamma_1}{1 + \gamma_1}(M_1^2 - 1)\right] \left\{ 1 - \frac{(\gamma_4 - 1)\left(\frac{u_{a1}}{u_{a4}}\right)\left(\frac{P_2}{P_1} - 1\right)}{\sqrt{2\gamma_1[2\gamma_1 + (\gamma_1 + 1)\left(\frac{P_2}{P_1} - 1\right)]}} \right\}^{-2\gamma_4(\gamma_4 - 1)} \quad (5.2)$$

Considering the viscous effects, the steady expansion between the shock wave and the contact surface and the unsteady expansion in the driver gas, Duff [22] proposed a simple one-dimensional model:

$$\left(\frac{P_4}{P_1}\right)_{Duff} = \left\{ 1 + \frac{M_1^2 + \beta - 1}{(\beta - 1)[M_1^2(\beta + 1) - 1]} \right\}^{(\beta + 1)/2} \left(\frac{P_4}{P_1}\right)_{ideal} \quad (5.3)$$

The experiment is carried out in the $500 \mu\text{m}$ capillary at the fixed position $x/D = 680$. This position is chosen for comparison with other measurements in [53]. Besides, this position is not too small, so that it doesn't lay inside the shock formation length. And, it is not too big, so that the shock doesn't attenuate much. The experimental data are compared with the models from Eqs. 5.2 and 5.3 in Fig. 5.9.

Fig. 5.9 shows that the experiment doesn't agree with neither the ideal model nor Duff's model. This deviation may due to the significant wall friction and heat conduction. Compared to the ideal model, Duff's model is one small step closer to the experimental values. However, Duff's model hasn't taken the dimensional effects, i.e. the role of the hydraulic diameter D in Eq. 5.3, into consideration. This may be the reason or one of the reasons, why Duff's model doesn't fit my experimental values. Recent years, Hadjadj's group [41] has taken the wall friction and heat conduction into their numerical studies involving the scaling factor Sc , where D is considered. They have

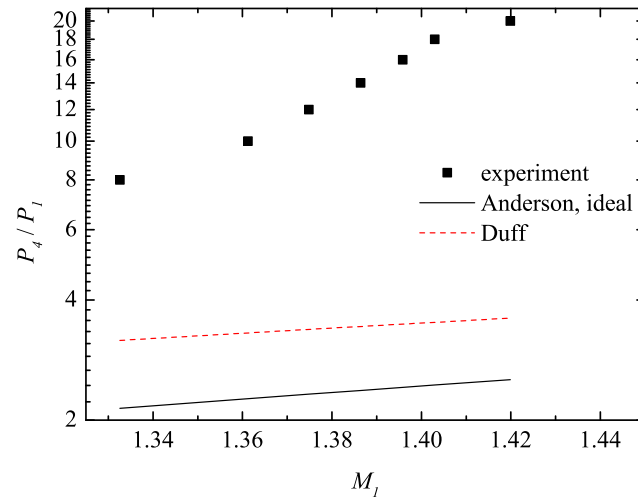


Figure 5.9: Shock wave Mach number as a function of the driver/driven pressure ratio. Measured in the 500 μm capillary at the position $x = 340$ mm (not too close to the formation phase but also not too far away). Driver gas is nitrogen with variable P_4 from 8 bar to 20 bar. Driven gas is air with $P_1 = 1$ bar.

achieved better numerical relations between P_4/P_1 and M_1 . An analytical equation is not available, thus quantitative comparison can not be made with my experiment. But qualitatively, their numerical results share the same tendency as my experiment i.e. P_4/P_1 needs to be several times higher than the ideal model to produce the same shock Mach number. The numerical studies using CFD shall be an outlook for this work.

5.4 Oscillograph traces (density histories)

The shock flow oscillograph traces, which scale with flow density through Eq. 3.16, are presented in this section. These oscillograph traces provide the information about the arrival time of the shock wave and the contact surface, respectively. Furthermore the density jump across the shock wave can be calculated via Eq. 3.19. The corresponding measurement scheme is presented in Fig. 3.17(bottom).

Fig. 5.10 shows a selection of the oscillograph traces measured at different propagation distance x . Shock wave attenuation is here qualitatively noticeable (dash-dot line). It can be seen that the optical measurement with the LDI yields well resolved oscillograph traces, in which different flow regions can be identified. Note that within the present setup, the photo voltage $U(t)$ accessible by the LDI is limited by the maximum photo voltage U_0 , which is determined before each measurement (normally between 2.6 V and 2.8 V, affected by optical adjustment). Therefore, the measurement window in amplitude is $U(t)/U_0 < 1$. The maximum measurable density can be estimated by inserting $U_0 = 2.8$ into Eq. 3.16, which gives $\max(\rho) \approx 4.8 \text{ kg/m}^3$ in case of measuring Helium gas. If flow density larger than 4.8 kg/m^3 occurs, the corresponding optical phase difference between the interferometric beams may exceed $\pi/2$. Although this may limit the measurement of the full density histories in some special cases, the district of interest, namely the measurements of the shock wave and the contact surface have proved to be unaffected at all.

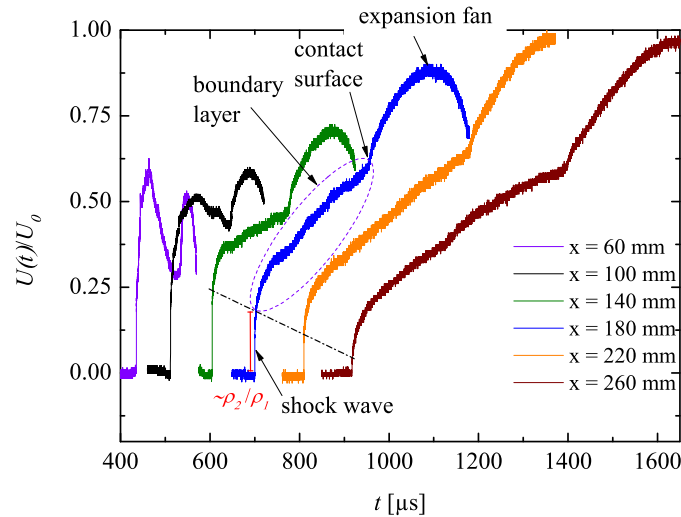


Figure 5.10: Oscillograph traces (with normalized voltage) of the shock flows in the $200 \mu\text{m}$ capillary at different propagation distance x . The dash-dot line indicates the decreasing shock-induced density jump ρ_2/ρ_1 . The normalized photo voltage $U(t)/U_0$ scales with the flow density $\rho(t)$ through Eq. 3.16. ‘One beam out’ arrangement of the LDI. $P_4 = 8 \text{ bar He}$, $P_1 = 1 \text{ bar air}$.

Fig. 5.10 shows a selection of the oscillograph traces, measured at different x (regarded as the flow propagation distance, it is also the distance between the valve and LDI). Attenuation of the shock induced density jump is qualitatively noticeable (dash-dot line). The 100 MHz sampling rate of the oscilloscope provides the time-resolution needed to allow the identification of different flow regions. Take the curve at $x = 180$ mm as an example, one can first observe a very sharp edge indicating the shock wave. The height of this edge correlates with ρ_2/ρ_1 . After the passage of the shock wave, the voltage signal (and thus density) increases slowly due to the growth of the boundary layer. Because the probe beam of LDI passes through the boundary layers and the core flow, it delivers the averaged flow density along its optical path. After further propagation, the contact surface shows up as the second edge (not as sharp as the first one). Then the density continues to increase behind the contact surface, because of the arrival of the high density driver gas combined with the further growth of the boundary layer. Finally, the expansion fan (reflected from valve bottom) arrives and decreases the flow density. Note that for curves at $x > 210$ mm, the expansion fan arrives much later, thus they are outside of the working range of LDI.

As a first result one can state that the oscillograph traces in Fig. 5.10 are qualitatively consistent with those determined within the pioneer work of Duff [22] and the later work of Garen [37]. For the density histories in the two previous works, the shock wave also corresponds to the first sharp edge, while the contact surface corresponds to the less sharp second edge. Note that, the previous works used different shock generation (diaphragm by Duff, rubber ball by Garen) and detection (electron canon by both) techniques than the current work. Furthermore, the ‘test time’ (time delay between shock wave and contact surface) in the work of Garen has the same order of magnitudes as the current work (by comparable shock Mach number, but larger shock tube with 1.8 cm diameter and lower initial pressure with 0.46 mbar). The consistence with the previous works gives additional support to the argument that the current work indeed detects the contact surface, not something else (e.g. artifacts or reflected shocks).

But there are also significant differences between the previous works and the current work, which will be discussed in details in the following sections of this chapter.

Additional oscillograph traces:

In additional to the representative oscillograph traces at chosen x positions in Fig. 5.10 (published in [77]), here in the thesis the oscillograph traces for all measured x positions (with the step of 10 mm) are presented (Fig. 5.11). Note that at every single x the measurement is actually repeated at least 5 times, but only one measurement curve for each x is displayed here for demonstration purpose (the analysis takes, of course, all five repeated measurements into consideration).

x from 45 mm to 80 mm: it corresponds to the shock formation phase. In this phase, the shock wave is being built up by trailing partial shocks or compression waves. Details

in section 5.1.

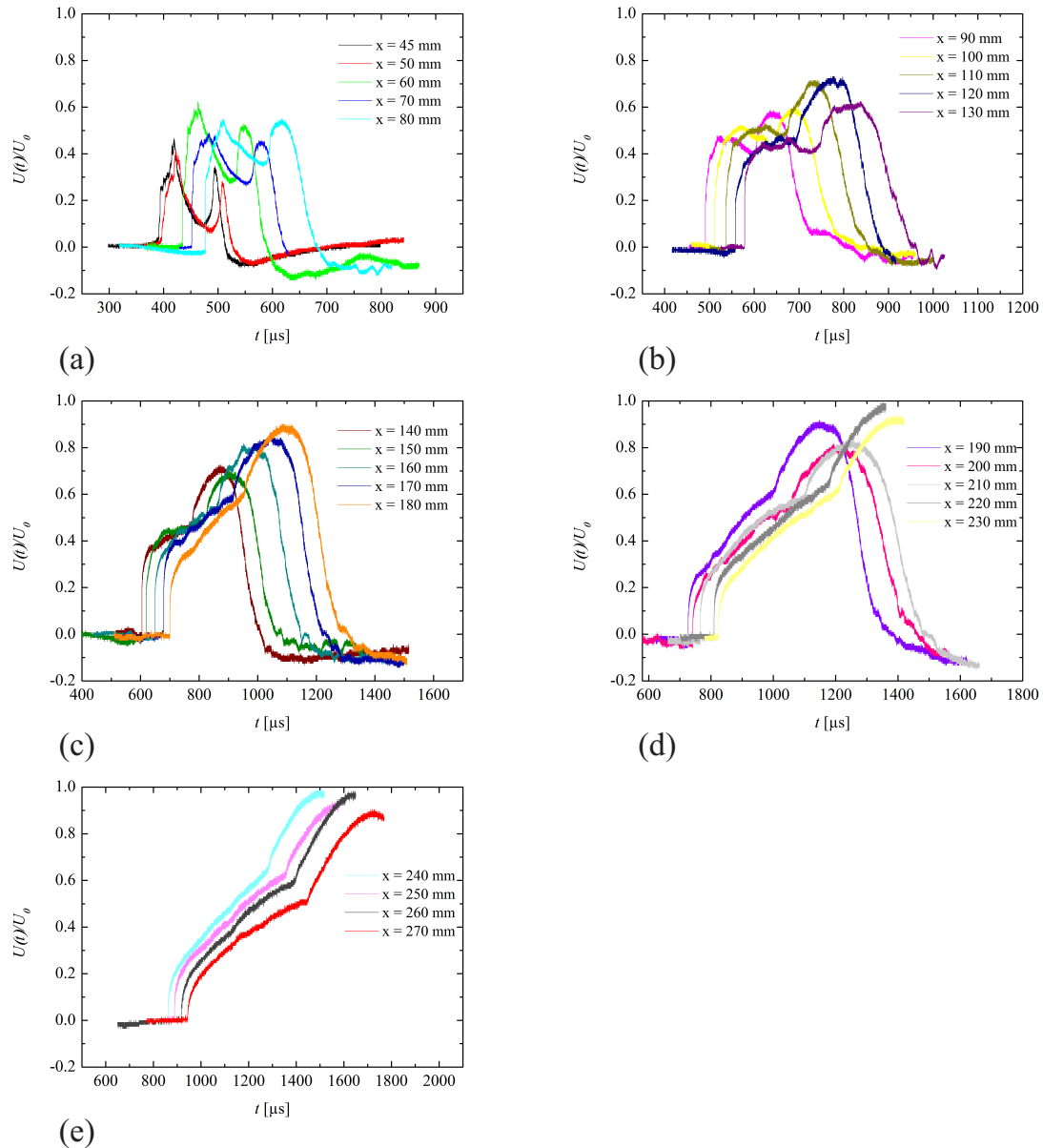


Figure 5.11: Oscillograph traces (with normalized voltage) of the shock flows in the $200\ \mu\text{m}$ capillary at different propagation distance x . ‘One beam out’ arrangement of the LDI. $P_4 = 8\ \text{bar He}$, $P_1 = 1\ \text{bar air}$.

x from 90 mm to 130 mm: turbulent post-shock flow. The boundary layer has irregularities e.g. instead of growing constantly thicker (indicated by constantly growing density jump), it goes up and down. The peak is considered as the arrival time of the expansion fan.

x from 140 mm to 270 mm: laminar post-shock flow. The boundary layer has smooth growth. Further support for the ‘laminar’ statement will be found in the later sections, where Reynolds number calculations are presented.

Discussion on boundary layer:

Fig. 5.12 and Fig. 5.13 present the shifted oscillograph traces. The oscillograph traces are shifted in a way that, the first edges (shock wave) of different curves temporally overlap.

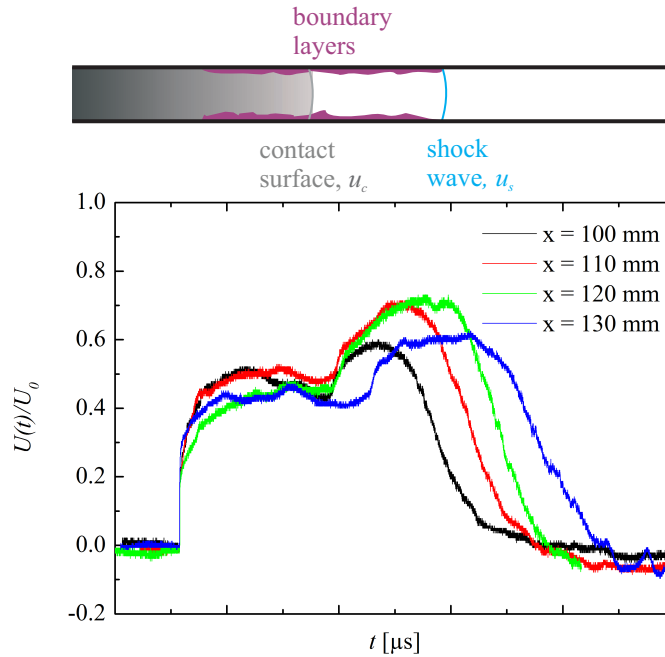


Figure 5.12: Temporally shifted shock flow oscillograph traces in the 200 μm capillary; turbulent boundary layer at $x < 140$ mm. $P_4 = 8$ bar He, $P_1 = 1$ bar air.

In Fig. 5.12, the oscillograph traces show that the boundary layers don't have a continuous growth with time. Furthermore, the boundary layers look quite chaotic and unstable. The preliminary explanation for this observation is that, these boundary layers or post-shock flows are turbulent for the positions $x < 140$ mm. The theoretically expected turbulent boundary layers are also sketched in this figure.

On the other hand, the density histories in Fig. 5.13 shows that the boundary layers grow smoothly and gradually with time (as illustrated by the sketch). There is good order (showing rare disturbance) in the boundary layer. Therefore, the post-shock flows at $x \geq 140$ mm possess the laminar characteristics.

In Fig. 5.14, the turbulent or laminar characteristics become even more evident. The representative positions $x = 110$ mm and $x = 170$ mm are chosen for the turbulent and laminar ranges, respectively. The choice of the two positions bases on the reason that, each one is far away (30 mm i.e. 150 times D away) from the critical point at $x = 140$ mm. Apparently, the five repeated measurements at $x = 110$ mm have quite different boundary layer development in the post-shock field (emphasized by the red circle). The low reproducibility corresponds to the turbulent characteristics. However, the five repeated measurements at $x = 170$ mm show very high reproducibility, which

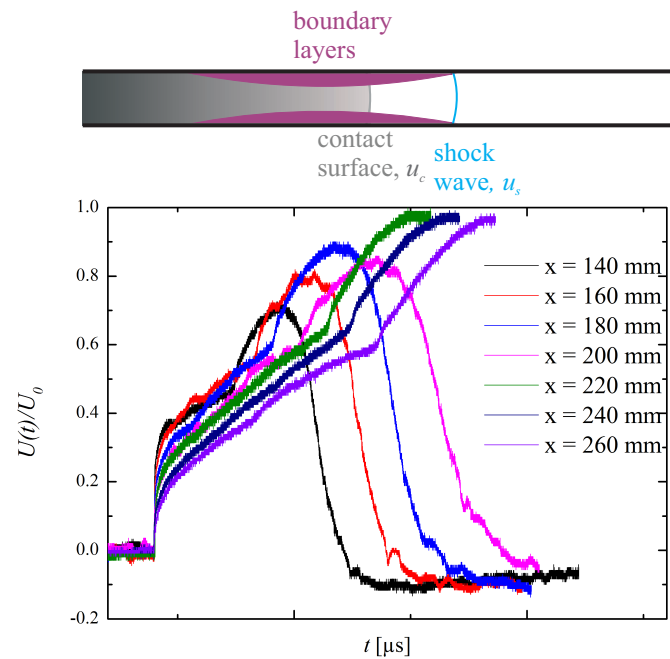


Figure 5.13: Temporally shifted shock flow oscillograph traces in the 200 μm capillary; laminar boundary layer at $x \geq 140$ mm. $P_4 = 8$ bar He, $P_1 = 1$ bar air.

corresponds to the laminar characteristics. It shall be remarked that, the reproducibility check is not just performed for these two representative positions but also all the other positions, which also confirm our statement here.

Further arguments by calculating Reynolds number is presented in section 5.6. Reynolds number will give more information on the turbulent/laminar transition.

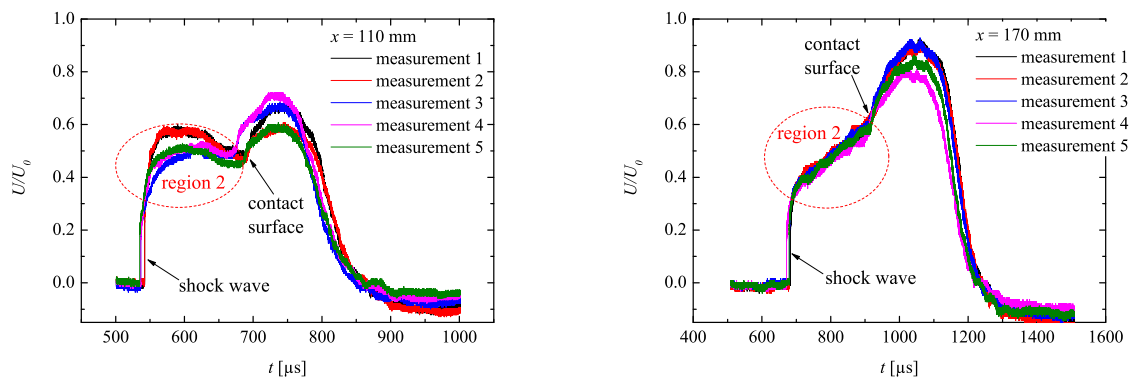


Figure 5.14: Shock flow oscillograph traces in the 200 μm capillary; Reproducibility check by five times repeated measurements; Left: measurements at $x = 110$ mm; Right: measurements at $x = 170$ mm. $P_4 = 8$ bar He, $P_1 = 1$ bar air.

5.5 Micro shock flow propagation

This section investigates the micro shock flow propagation.

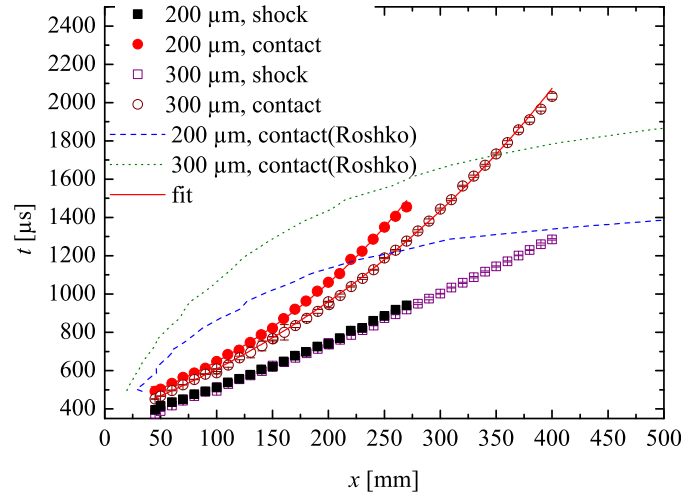


Figure 5.15: The flow trajectories in the 200 μm and 300 μm diameter capillaries. Error bars derived from standard deviation are smaller than the symbols here. Theoretical prediction from Roshko. $P_4 = 8$ bar He, $P_1 = 1$ bar air. The fit function is double exponential, i.e. $x_{c,fit}(t) = A_1 \exp(-t/B_1) + A_2 \exp(-t/B_2) + y_0$

Fig. 5.15 shows the trajectories of the flow in the 200 μm and 300 μm capillaries, correspondingly:

- 1) Shock wave. The shock waves trajectories in both capillaries only differ very slightly. Nevertheless, the slightly stronger bending of the 200 μm curve indicates that the shock wave in a smaller capillary experiences larger friction. The bending of the trajectories can be made clearer by differentiating the curve i.e. use the ‘two beams in’ arrangement of LDI to measure the local shock velocity. This will be shown later in Fig. 5.17.
- 2) Contact surface. The curve of the 200 μm capillary is significantly above that of the 300 μm capillary. This means that the contact surface is moving faster in the larger tube.

The combination of point 1) and 2) shows that the downscaling has a significantly stronger impact on the contact surface than on the shock wave. The model from Roshko [34] doesn’t agree with our measurements. In [34], the assumption of thin boundary layer and $u_p = u_c$ are mainly applied. In the micro shock flow, the boundary layer can be so thick that it fills more than half of the capillary cross-section (approximated by using Blasius equation in [74]). Moreover, u_p and u_c are not necessarily the same, because they correspond to two mechanisms: The post-shock particles closely behind the shock wave are dragged into motion by the shock wave. On the other side, the contact surface is not ‘dragged’ by the shock wave, but rather ‘pushed’ by the driver

gas from behind. Therefore, Roshko's model doesn't apply for micro shock flows.

When the calculation using directly measured data introduces too large errors, it is quite common to represent the experimental data by an appropriate fit function prior to further processing (also to smooth the curve). Following this procedure, exponential fits are applied for the contact surfaces in Fig. 5.15. The corresponding fit function is (the horizontal and vertical axes are flipped for calculation convenience):

$$x_{c,fit}(t) = A_1 \exp(-t/B_1) + A_2 \exp(-t/B_2) + y_0 \quad (5.4)$$

A_1 , A_2 , B_1 , B_2 and y_0 are fit parameters. The subscript 's' and 'c' indicate shock wave and contact surface, respectively. For the 200 μm capillary, $A_1 = 205.02$, $A_2 = 205.02$, $B_1 = -207.79$, $B_2 = -207.79$ and $y_0 = -16.08$. For the 300 μm capillary, $A_1 = 373.17$, $A_2 = 373.17$, $B_1 = -333.93$, $B_2 = -333.93$ and $y_0 = -398.14$. The fit functions are then applied for simple algebraic calculations in the following. L can thus be determined as $L(x_s) = x_s(t) - x_{c,fit}(t)$ (plotted in Fig. 5.16), where $x_s(t)$ are the directly measured data pairs from Fig. 5.15. Therefore the curves in Fig. 5.16 are plotted as discrete points instead of lines.

In the macro shock flow (experimental and theoretical) research [22, 34, 78], the contact surface and the shock wave eventually have the same speed leading to constant L (e.g. after the shock wave propagation of 230 times D in [22]). However, in the present work, the contact surface departs monotonically from the shock wave. This is still the case after the propagation distance of 1300 times D . Later in this section, it will show that the shock velocity is slowed down to sound speed at the position 1300 times D . Again, the thin boundary layer assumption in previous works may be the cause of this disagreement.

The actual results may also be compared to the investigations in [9], in particular to the scaling factor $Sc = Re \cdot D/(4L)$. Although in principle, down-scaling has been successfully performed by applying this factor in different works such as [13], [15] and [41], up to now the main problem is still the missing knowledge of L (also considered as the friction length, but this could not be measured in [9]). It was only possible to use the shock propagation length x_s as a very rough approximation for L in those works. The current work, however, determines L and thus truly allows the calculation of the scaling factor.

As an example, for $D = 200 \mu\text{m}$, the Reynolds number in front of the shock $Re = \rho_1 u_a D / \mu \approx 4300$ (with the atmospheric air density $\rho_1 \approx 1.205 \text{ kg/m}^3$, dynamic viscosity $\mu \approx 1.82 \cdot 10^{-5} \text{ kg/(m}\cdot\text{s)}$, sound velocity $u_a = 343 \text{ m/s}$) and $41 \text{ mm} \leq L \leq 89 \text{ mm}$ (corresponds to $80 \text{ mm} \leq x \leq 260 \text{ mm}$, phase (B) and (C) in Fig. 5.17), the calculation yields $2.5 \leq Sc \leq 5.5$, which is part of the range discussed in [9]. This Sc range is expected to show dissipative effects due to wall friction and heat conduction.

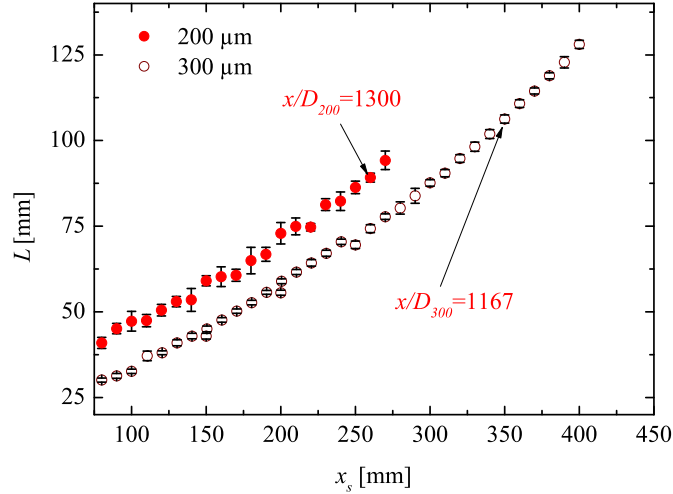


Figure 5.16: Shock-contact distance L as a function of shock location x_s . Derived from shock wave and contact surface trajectories in Fig. 5.15 via the relation $L(x_s) = x_s(t) - x_{c,fit}(t)$. $P_4 = 8$ bar He, $P_1 = 1$ bar air.

Fig. 5.17 shows the flow velocities. $u_s(x)$ is directly measured using the ‘two beams in’ arrangement of LDI. The velocity of the contact surface $u_c(x)$ cannot be determined by that arrangement, because once the shock wave passes the second LDI beam, LDI doesn’t have a clear reference beam anymore. Therefore, $u_c(x)$ is calculated by differentiating the fit function $x_{c,fit}$ displayed in Eq. 5.4.

The particle velocity u_p induced by the shock (immediately behind the shock front, see Fig. 5.1) can be derived from $u_p = u_s(1 - \rho_1/\rho_2)$ [32] by inserting the experimentally determined values u_s and ρ_2/ρ_1 . Here it shows $u_p \neq u_c$. The reason is that this u_p corresponds to the particles closely behind the shock wave, not the particles close to the contact surface, where both velocities are equal according to conventional theories. This results shows that u_p has a spatial distribution.

For the case of a macroscopic shock tube operating at the same conditions (gas pairs and pressure ratio) as the microscopic tubes used here, the theoretical value of the initial shock Mach number is 1.9, which can be derived from the well-established shock tube relation [32] and the Rankine-Hugoniot relations. This theoretical value clearly doesn’t agree with our micro scale experiments (max. initial Mach number 1.3) due to the significant scaling effects already happening during the shock formation phase. The dissipative effects on the initial shock Mach number are also reported in our previous work [40].

It can be seen in Fig. 5.17 that the shock waves eventually turn into a sound wave. The velocity of the contact surfaces appears to be monotonically decreasing. u_c may eventually reach a value of zero in the absence of the shock wave, if a long enough capillary was available. Again, Fig. 5.17 confirms that the shock wave and the contact

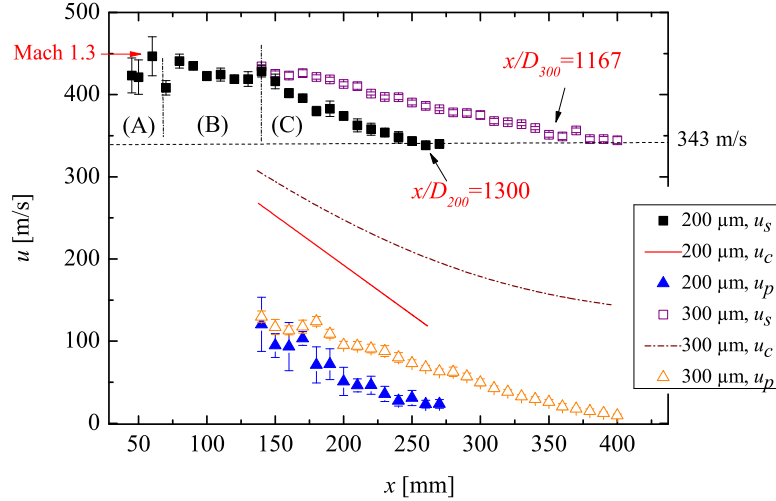


Figure 5.17: Shock wave velocity u_s (direct measurement, ‘two beams in’), contact surface velocity u_c (derived from fit) and post-shock particles velocity u_p (indirect measurement) as functions of propagation distance x . $P_4 = 8$ bar He, $P_1 = 1$ bar air.

surface depart from each other, since u_c is always lower than u_s . Furthermore, u_s and u_c decelerate much faster in the 200 μm capillary than in the 300 μm capillary. Therefore, Fig. 5.17 is also an experimental confirmation of the increased friction for smaller capillaries. Indeed additional measurements (not shown here) with $D = 500$ and 700 μm capillaries, respectively, clearly show that increased friction (due to the increased area-to-volume ratio) can be observed for decreasing D .

For the shock wave in the 200 μm capillary, u_s has three different phases: (A) shock formation (because trailing compression waves with large uncertainties are detected, displayed in section 5.1); (B) changing shock attenuation followed by acceleration till the transition to the next phase; (C) quasi linear attenuation. The Reynolds number Re_2 of the particles flow immediately behind the shock (i.e. limited to the thin region where the boundary layer hasn’t developed yet; as sketched in Fig. 5.1) can be calculated according to [8, 40] as $Re_2 = u_p D \rho_2 / \mu$. The calculations of Re_2 show that the transition point between phase (B) and (C) correlates with the turbulent/laminar transition, because $Re_2 > 2300$ in (B), while $Re_2 < 2300$ in (C). More details are provided in section 5.6.

5.6 Turbulent/Laminar transition of micro shock

This section takes a closer look into the three different phases of u_s in Fig. 5.17 for the 200 μm capillary. The figure show three different phases: (A) shock formation; (B) changing attenuation; (C) linear attenuation.

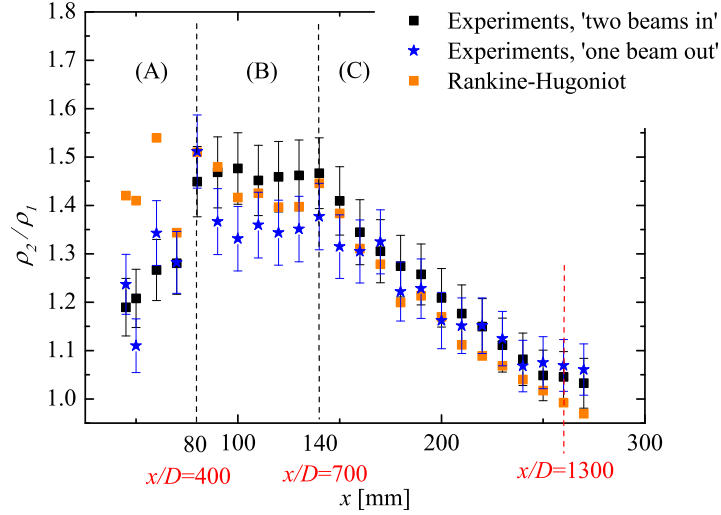


Figure 5.18: Density jump ρ_2/ρ_1 across the micro shock as a function of propagation distance x in the 200 μm capillary. $\rho_1 = 1.205 \text{ kg/m}^3$ is atmospheric air density. $P_4 = 8$ bar He, $P_1 = 1$ bar air.

In Fig. 5.18 the three phases are again clearly distinguishable. Note that the density measurements are independent from the velocity measurements. All four curves in Fig. 5.5 and 5.18 are consistent with the same phases (A), (B) and (C).

The Rankine-Hugoniot [32] relation (ideal) is also used to calculate ρ_2/ρ_1 from the experimentally measured $u_s(x)$. The experiments agree with the ideal RH-theory within the 5 % error. This again shows high reproducibility of the valve and high reliability of the LDI, which obtains the same result from two different arrangements, i.e. ‘two beams in’ and ‘one beam out’. Furthermore, it is discussed in section 4.9 in the frame of the plasma shock, that the ideal RH still applies for the 200 μm hydraulic diameter. Evidently, the ideal RH also applies for the valve generated shock in the capillary with 200 μm hydraulic diameter. What’s more interesting is that, apparently the curved shock front displayed in Fig. 3.9 isn’t a problem for the density measurement (at least not for 200 μm), as long as the data reading is performed correctly.

The particle velocity u_p induced by the shock (immediately behind the shock front) is [32]:

$$u_p = u_s \left(1 - \frac{\rho_1}{\rho_2}\right) \quad (5.5)$$

Inserting the experimentally measured values of u_s and ρ_1/ρ_2 for the corresponding x into Eq. 5.5, one can determine $u_p(x)$.

The Reynolds number Re_2 of the shock-induced particles flow in the mainstream is [8, 40]:

$$Re_2 = \frac{u_p D \rho_2}{\mu} = u_s \left(1 - \frac{\rho_1}{\rho_2}\right) \frac{D \rho_2}{\mu} \quad (5.6)$$

μ is the dynamic viscosity. For small to moderate Mach numbers, μ is $1.85 \cdot 10^{-5}$ kg/(m·s) and remains approximately constant (for ambient air at normal conditions) [73]. Note that, Eq. 5.6 yields an approximated value for the flow region closely behind the shock front, where the boundary layer hasn't developed much, yet.

By inserting the previously measured shock velocity $u_s(x)$ and density ρ_2 into Eq. 5.6, one can thus determine $Re_2(x)$, which is plotted in Fig. 5.19.

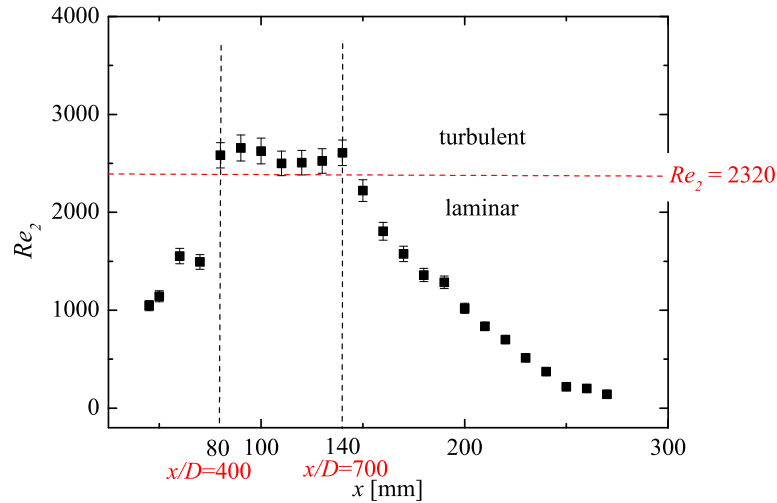


Figure 5.19: The development of the Reynolds number behind shock Re_2 in the 200 μm capillary. $P_4 = 8$ bar He, $P_1 = 1$ bar air.

Fig. 5.19 clearly shows a turning point at $x = 140$ mm (or 700 times D) is observed, which correlates with the turbulent/laminar transition. To analyse this observation, a simple estimation of the wall friction effect can be done via applying the Darcy friction factor λ .

For laminar flow, one may apply the relation between Re_2 and λ [79]:

$$\lambda = \frac{64}{Re_2} \quad (5.7)$$

For turbulent flow, one can use the Blasius correlation as approximation [79]:

$$\lambda = \frac{0.3164}{Re_2^{1/4}} \quad (5.8)$$

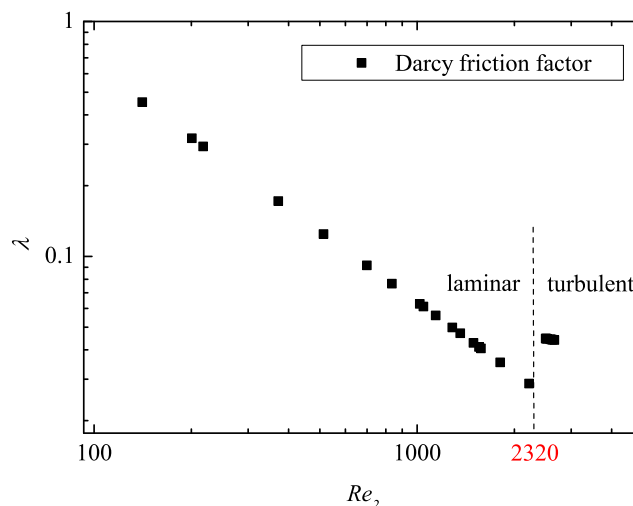


Figure 5.20: The development of the Darcy friction factor λ of the post-shock flow in the 200 μm capillary. $P_4 = 8$ bar He, $P_1 = 1$ bar air.

Fig. 5.20 is calculated using Eq. 5.7 and 5.8 by inserting the previously determined $Re_2(x)$ from Fig. 5.19, correspondingly. It can be seen that, λ has a sudden change at the turbulent/laminar transition point. This leads to the sudden friction reduction and thus the acceleration of shock at the transition point.

It may be noted that, if this transition point didn't exist, there would be a simple linear shock attenuation along the orange dot-dash line as indicated in Fig. 5.5. The shock velocity would be much sooner reduced to sound speed after a propagation length of 1130 times diameter in theory, which is almost 200 times diameter less than the experimental curve. This finding may be of great importance for medical usage of shock wave for vaccine/drug delivery, where the shock propagation length is a deciding parameter.

5.7 ‘Leaky piston’ model and correction suggestion

For shock wave research, the time delay between the shock wave and the contact surface arriving at a certain position is a very important parameter. This time delay is called test time or hot flow duration τ_{hot} (sketched in Fig. 5.21). During this time τ_{hot} in a conventional shock tube, this hot flow is quasi uniform and has constant high temperature T_2 , high pressure P_2 and high density ρ_2 . More importantly, these flow properties are very swiftly switched on upon the arrival of the shock wave. Therefore, a shock tube is a great instrument which can provide a well-defined hot environment for many different research fields including chemistry and aerospace technology.

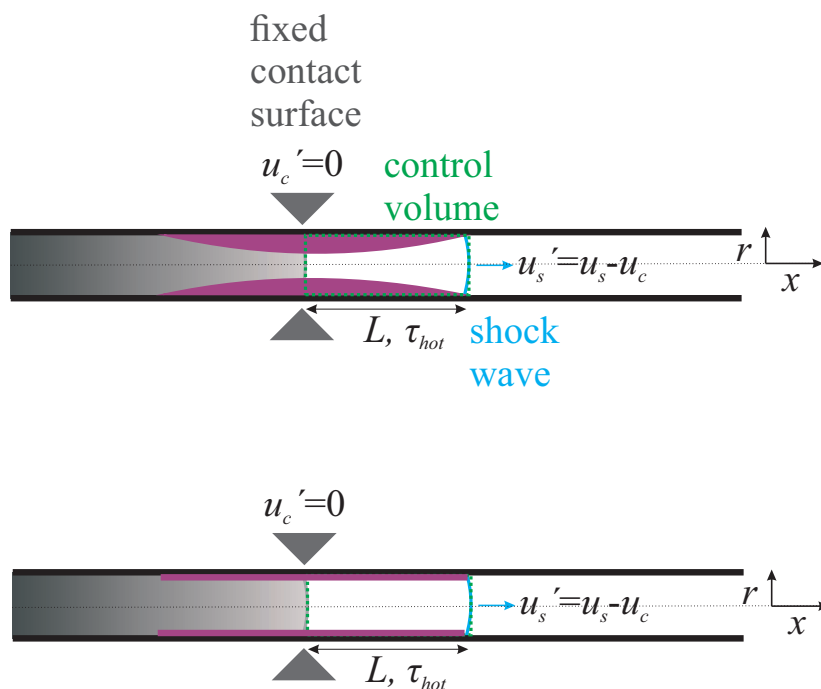


Figure 5.21: Sketch of a shock flow in a tube in a contact-fixed reference system. Top: a shock flow with boundary layer development. Bottom: a shock flow with thin boundary layer assumption.

The aerospace scientists and engineers, who study the spaceship reentry, often investigate a down-sized spaceship in a conventional shock tunnel (a large shock tube). But the test time in the shock tunnel is not unlimited long, because the test time starts with the arrival of the shock wave and ends with the arrival of the contact surface (the start of the cold flow). This means those scientists cannot make an arbitrary long test. A typical value of the test time is about 1 ms [80]. Naturally, one has to ask how long is this τ_{hot} exactly? How can it be affected by the design of the shock tunnel? These questions are firstly investigated by Russel Duff in the pioneer work [22], and then answered by the famous ‘leaky piston’ model developed by Anatol Roshko in Caltech [34].

This section starts with a short explanation of the ‘leaky piston’ model. The problems

and potential corrections of this model for micro shock flow is presented as the second step.

Review of the 'leaky piston' model:

According to Roshko, the net mass flow rate \dot{m} into the control volume indicated in Fig. 5.21 (bottom) is:

$$\dot{m} = \dot{m}_s - \dot{m}_c \quad (5.9)$$

with the mass flow rate across the shock wave \dot{m}_s and across the contact surface \dot{m}_c , respectively.

\dot{m} can also be calculated as:

$$\dot{m} = \rho_2 \dot{L} \frac{\pi D^2}{4} \quad (5.10)$$

Consistent with other parts of the thesis, the subscript '1' indicates the region ahead the shock wave, '2' behind the shock wave.

\dot{m}_s can be calculated as:

$$\dot{m}_s = \rho_2 (u_s - u_c) \frac{\pi D^2}{4} = \rho_2 (u_s - u_p) \frac{\pi D^2}{4} \quad (5.11)$$

In the equation above, Roshko has applied the classical (or conventional) assumption that the post-field particles velocity is equal to the contact surface velocity. This assumption means:

$$u_p = u_c \quad (5.12)$$

The classical thin boundary layer assumption is applied by Roshko, so that:

$$\dot{m}_c = \rho_w u_p \pi D \delta \quad (5.13)$$

with boundary layer thickness δ . The subscript 'w' indicates the wall of the tube, e.g. ρ_w is the flow density at the wall. δ can be calculated as:

$$\delta = \beta \sqrt{\frac{\mu_w L}{\rho_w u_p}} \quad (5.14)$$

β is a parameter introduced by Roshko. It depends conditions outside of the boundary layer.

From Eq. 5.9 to 5.14, the time derivative of the shock-contact distance L can be

obtained:

$$\frac{dL}{dt} = \frac{u_p}{\rho_2/\rho_1 - 1} - 4\beta \frac{\rho_w u_p}{\rho_2 D} \sqrt{\frac{\mu_w L}{\rho_w u_p}} \quad (5.15)$$

The right-hand side of the equation above is set to zero, so that the maximum value L_{max} can be determined:

$$L_{max} = \frac{1}{16\beta^2} \left(\frac{\rho_2}{\rho_w}\right)^2 \left(\frac{D}{\rho_2/\rho_1 - 1}\right)^2 \frac{\rho_w u_p}{\mu_w} \quad (5.16)$$

Eq. 5.15 can be rewritten using L_{max} :

$$\frac{dL}{dt} = \frac{u_p}{\rho_2/\rho_1 - 1} \left[1 - \left(\frac{L}{L_{max}}\right)^2\right] \quad (5.17)$$

$$\Rightarrow \frac{d(L/L_{max})}{d(u_p t / ((\rho_2/\rho_1 - 1)L_{max}))} = \frac{u_p}{\rho_2/\rho_1 - 1} \left[1 - \left(\frac{L}{L_{max}}\right)^2\right] \quad (5.18)$$

Roshko defined the normalized hot flow duration as T_{hot} , while the normalized spatial coordinate as X (in flow direction):

$$X = \frac{\rho_1 x}{\rho_2 L_{max}} \quad (5.19)$$

$$T_{hot} = \frac{\tau_{hot}}{\tau_{hot,max}} = \frac{L}{L_{max}} \quad (5.20)$$

Insert Eq. 5.19 and 5.20 into Eq. 5.18. After simple algebraic calculations, Roshko obtained the ‘leaky piston’ model which is displayed as a relation between X and T_{hot} :

$$\boxed{\frac{X}{2} = -\ln(1 - \sqrt{T_{hot}}) - \sqrt{T_{hot}}} \quad (5.21)$$

Note that Hooker [78] and Mirels [35] have made modifications to the ‘leaky piston’ model, but diverse assumptions are also applied. Especially the thin boundary layer assumption is still kept in the two modifications. In the end, Hooker and Mirels have achieved a better match between the modified models and the experiments in macroscopic shock tubes. However, the modified models from Hooker and Mirels don’t agree with the micro shock flow measured in this project (they have totally different tendency).

Reformulation of the 'leaky piston' model and comparison with current experiments

In this part, I reformulate the 'leaky piston' model from Eq. 5.21 to the form $L(x_s)$, so that it can be practically compared with experimental values. The form $L(x_s)$ is more practical, because the dimensional parameters x_s and L (not the dimensionless X and T_{hot}) are measured in the experiments.

First of all, the ideal model is explained. As Roshko wrote, for an ideal tube, there is no leakage term in his similarity solution for $X(T_{hot})$. An ideal shock tube has the relation:

$$T_{hot,i} = X \quad (5.22)$$

$T_{hot,i}$ is the ideal hot flow duration. Subscript 'i' stands for 'ideal'.

As defined in [34]:

$$T_{hot} = \frac{L}{L_{max}} \quad (5.23)$$

This gives another expression for $T_{hot,i}$:

$$T_{hot,i} = \frac{L_i}{L_{max}} \quad (5.24)$$

Furthermore, X is defined by Roshko as:

$$X = \frac{\rho_1 x_s}{\rho_2 L_{max}} \quad (5.25)$$

The combination of Eq. 5.22, 5.24 and 5.25 gives:

$$\frac{\rho_1 x_s}{\rho_2 L_{max}} = \frac{L_i}{L_{max}} \quad (5.26)$$

which leads to

$$L_i = \frac{\rho_1 x_s}{\rho_2} \quad (5.27)$$

Applying the Rankine-Hugoniot relation into the equation above, it gives the relation $L_i(x_s, M_s)$ for an ideal shock tube. Here is the corresponding ideal model:

$$\boxed{L_i = \frac{\rho_1 x_s}{\rho_2} = \frac{2 + (\gamma - 1)M_s^2}{(\gamma + 1)M_s^2} x_s} \quad (5.28)$$

Insert Eq. 5.25 and Eq. 5.23 into Eq. 5.21:

$$\frac{\rho_1 x_s}{2\rho_2 L_{max}} = -\ln\left(1 - \sqrt{\frac{L}{L_{max}}}\right) - \sqrt{\frac{L}{L_{max}}} \quad (5.29)$$

$$\Rightarrow x_s = \frac{2\rho_2 L_{max}}{\rho_1} \left[-\ln\left(1 - \sqrt{\frac{L}{L_{max}}}\right) - \sqrt{\frac{L}{L_{max}}} \right] \quad (5.30)$$

Eq. 5.30 is the ‘leaky piston’ model written in the form of $x_s(L)$. This equation tells that from the known L_{max} and L , the ‘leaky piston’ model predicts a value for the corresponding x_s .

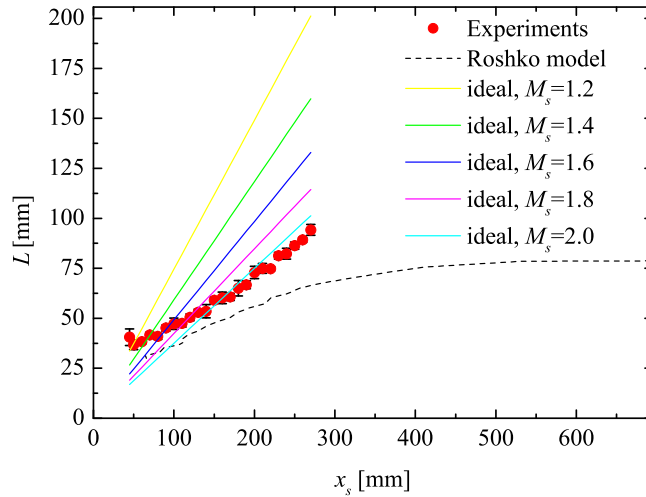


Figure 5.22: Shock-contact distance as a function of shock position. The experimental data are derived from the wave diagram in Fig. 5.15.

In Fig. 5.22, the shock-contact distance L (or L_i) is plotted against the shock position x_s . In this figure, the ideal model is calculated using Eq. 5.28, while the ‘leaky piston’ model is calculated by Eq. 5.30. The experimentally determined data pairs (x_s, L) are also plotted with those theoretical values.

The experimental values are much higher than the ‘leaky piston’ model. This may suggest that the contact surface never catches up with the shock wave, so that L keeps increasing. The ‘leaky piston’ model says, because the shocked gas (from region 2) leaks through the contact surface, the contact surface accelerates while the shock wave decelerates. However, in micro tubes as in our experiments, the driver gas experiences very large viscous effect which balances the leaked shocked gas, so that the contact surface may not be able to accelerate at all. At very large x_s outside of our experimental range, the contact surface shall be decelerated to zero velocity (because the driver gas is a mass flow), while the shock wave slows down to sound velocity. It is expected that L will just keep increasing.

A further comparison between the ‘leaky piston’ model and our experiments is presented here. The experimental data from Duff, Hooker and Roshko are also displayed. In the end, correction suggestions to the model are made.

First of all, $\tau_{hot} = t_c - t_s$ is retrieved from Fig. 5.15 and displayed in Fig. 5.23.

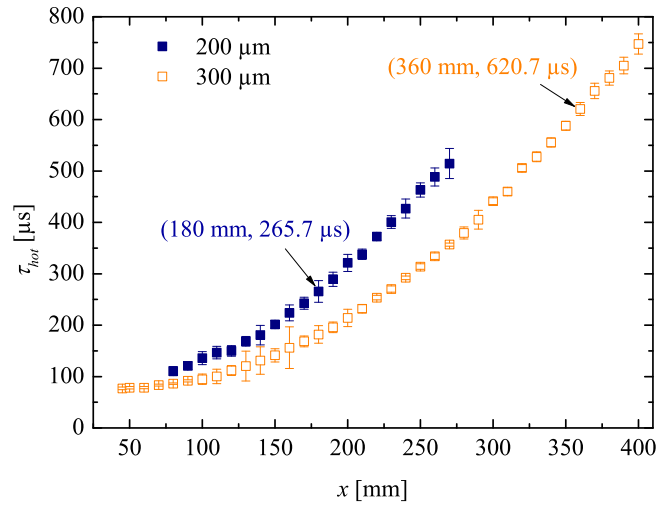


Figure 5.23: Hot flow duration τ_{hot} as a function of position x . $P_4 = 8$ bar He, $P_1 = 1$ bar air.

The values of x from Fig. 5.23 are normalized as X using Eq. 5.19, while the corresponding experimental values of τ_{hot} are normalized as T_{hot} using Eq. 5.20. And then, the normalized values are plotted in Fig. 5.24 together with the ‘leaky piston’ model from Eq. 5.21.

Fig. 5.24 further confirms that although the ‘leaky piston’ model works well for the macro shock flows (inserted figure [35]), it doesn’t agree with the micro shock flow. Moreover, the ‘leaky piston’ model for the 200 μ m and 300 μ m capillaries have the same curve. This is expected, because the scaling effects are not considered in the ‘leaky piston’ model. Meanwhile, the experimental values of the two capillaries show noticeable difference in the range $X < 2$.

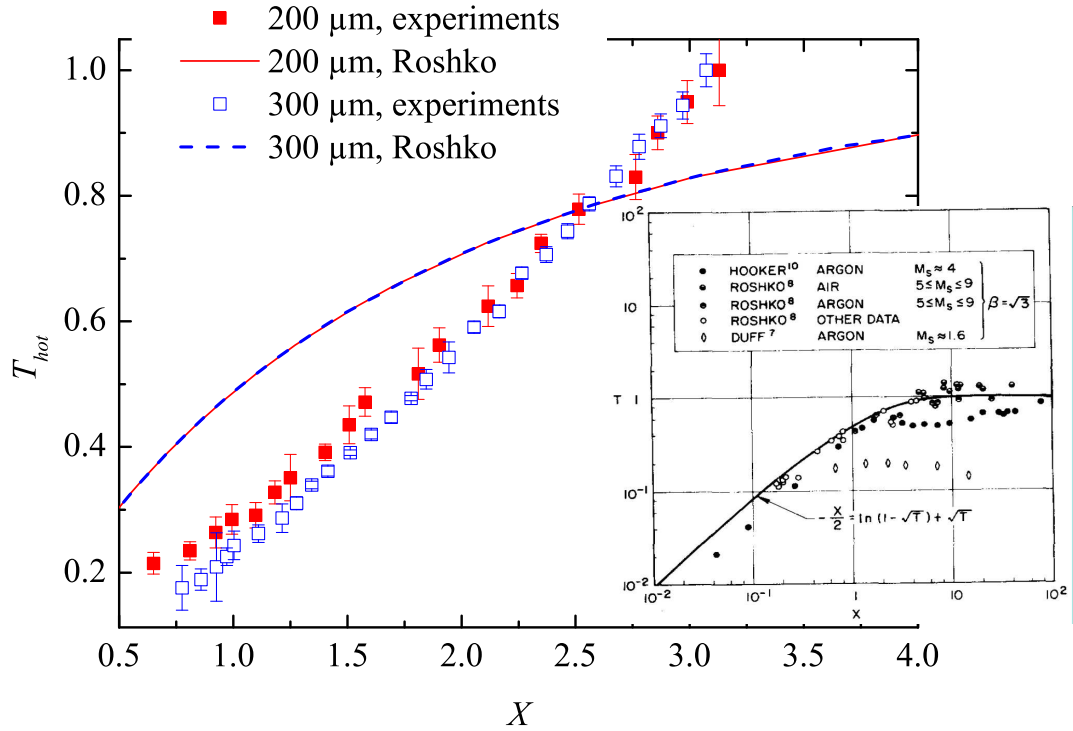


Figure 5.24: The dimensionless hot flow duration T_{hot} plotted against the dimensionless distance of the shock wave from the valve X . The build-in figure is conventional macroscopic shock tubes results taken from [35] (T_{hot} is notated as T here; tube 7.62 cm diameter) as a comparison.

Correction suggestion:

The potential goal here is to make a correction to the ‘leaky piston’ model, so that it can be applied to both the macro and micro shock tubes. Of course, the model suitable for the micro flow may be an ‘overkill’ for the macro flow, because the micro-scale related phenomena (e.g. wall friction and heat conduction) may be negligibly small for the macro flow.

To explain the discrepancy between the ‘leaky piston’ model and experimental values of the micro shock flows, we firstly examine the thin boundary layer assumption applied in the model. As indicated in Fig. 5.21(Top), for each position x , the boundary layer has the maximum thickness at the contact surface. This is due to the reason that the cold flow behind the contact surface interrupts and suppresses the boundary layer [35]. δ_{max} can be approximated by inserting the corresponding τ_{hot} from Fig. 5.23 into Eq. 4.17:

$$\delta_{max} = 1.1\sqrt{2\nu\tau_{hot}} \quad (5.31)$$

Fig. 5.25 shows that the maximum boundary layer in the 200 μm capillary can fill the

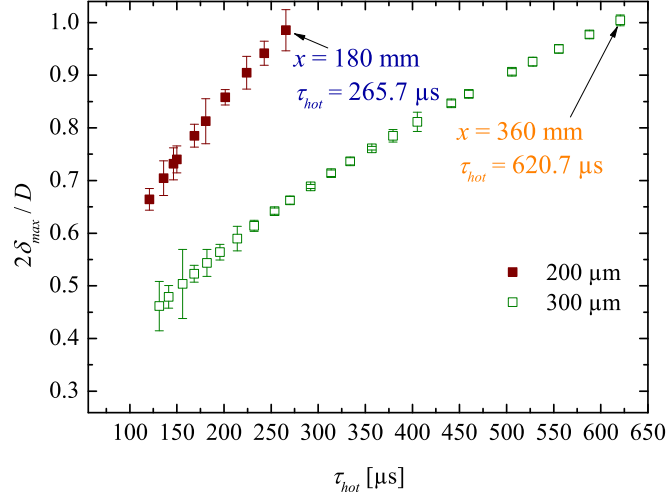


Figure 5.25: Relative maximum boundary layer thickness $2\delta/D_{max}$ in the capillary as a function of the hot flow duration τ_{hot} . $P_4 = 8$ bar He, $P_1 = 1$ bar air.

whole capillary at the position $x = 180$ mm (here $2\delta/D_{max} = 1$). While for the 300 μm capillary, the boundary layer can fill the whole capillary at $x = 360$ mm.

The thin boundary layer assumption is thus not suitable for micro shock flow. Without this assumption, the mass flow rate across the contact surface is:

$$\dot{m}_c = \int_{r_{BL}}^{D/2} \rho(r)u(r)rdr \quad (5.32)$$

with r_{BL} as the distance between the tube axis to the upper border of the boundary layer.

Now, we examine the assumption $u_p = u_c$ which has been applied in the model. These two velocities actually correspond to two mechanisms. The post-shock particles closely behind the shock wave are dragged into motion by the shock wave. On the other side, the contact surface velocity corresponds to the expanding driver gas front. The contact surface is not ‘dragged’ by the shock wave. Instead, it is ‘pushed’ by the driver gas from behind. Fig. 5.17 has already shown that $u_p \neq u_c$.

Therefore, u_p cannot be assumed to be the same as u_c for micro shock flows. u_p and u_c don’t have to, but can share the same value in some special situations e.g. in a large macroscopic shock tube (e.g. in [32]).

The mass flow rate across the shock wave is then:

$$\dot{m}_s = \rho_2(u_s - u_c) \frac{\pi D^2}{4} \quad (5.33)$$

The ‘leaky piston’ model has to use more realistic conditions, in order to describe micro shock flows. Therefore, Eq. 5.33 and 5.32 shall replace Eq. 5.11 and 5.13, respectively.

The same calculations procedure can then be performed again with these two new equations. As a potential solution, the new relation of X as a function of T_{hot} may be derived from solving the equations 5.9, 5.10, 5.14, 5.32 and 5.33. However, an **analytic** solution is unlikely to be achieved due to the complicated nature of the micro shock flow.

This work experimentally confronts the validity of the ‘leaky piston’ model at micro scale, makes correction suggestion and shall encourage CFD scientists to work on the **numeric** solution. At the moment that I write this sentence in Dec. 2017, our cooperation partner David Zeitoun is already working on the Navier-Stokes computation for our experimental conditions. His preliminary numeric results have roughly the same tendency as our experimental values, i.e. also confront the ‘leaky piston’ model. A common paper is expected to be submitted.

In the end, it shall be noted that in our micro experiments, the hot flow duration is investigated in a shock tube with the length of $x/D > 1000$, which hasn’t been investigated in conventional macro shock tubes. A typical length of a macro shock tube is merely above one hundred times the diameter, e.g. the high enthalpy shock tunnel of the German aerospace center (DLR) in Göttingen has the length $x/D \approx 113$ [81], while the T5 shock tunnel at Caltech has $x/D \approx 133$ [80].

The micro shock experiments in this thesis offer a message that when a shock tube is constructed sufficiently long, the test time (hot flow duration) may not be saturated. This asymptotic evolution of the test time in macro tubes might also eventually disappear, if the tube is long enough, i.e. significant boundary layer development. As described at the very beginning of this section, longer test time is desirable for shock-related researches including the aerospace technology. Navier-Stokes computation (the code of Zeitoun) for macro shock tubes with the length $x/D > 1000$ may be the interesting first step of work, if some one wants to transfer the findings in micro tubes to macro tubes.

5.8 Schlieren photos

The Schlieren measurements in this section serves as a small control experiment for the LDI measurements. Here some Schlieren photos for the shock waves induced by the magnetic valve are presented. For both the Schlieren and LDI measurements presented in this section, the shock waves are generated using under the same conditions i.e. the driver gas is $P_4 = 20$ bar N_2 , while the driven gas is $P_1 = 1$ bar ambient air. This combination of gases is chosen to generate strong enough shock wave.

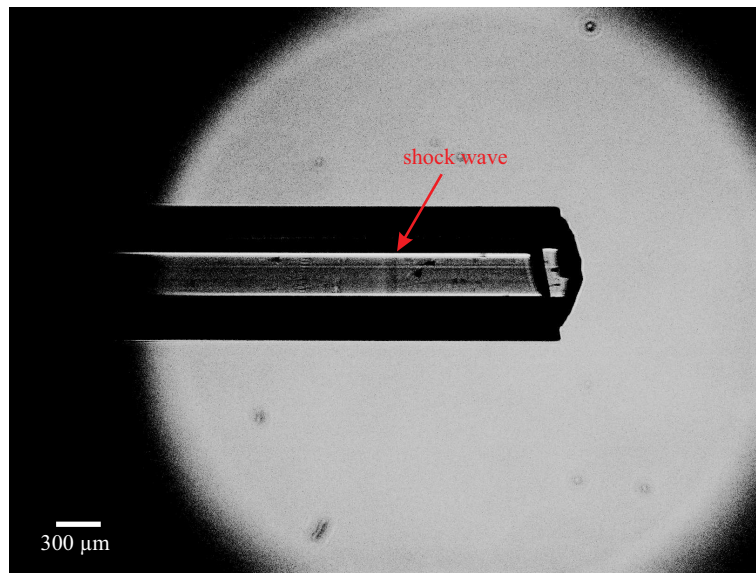


Figure 5.26: Schlieren image of a shock wave in a $300 \mu\text{m}$ capillary near the exit; $P_4 = 20$ bar N_2 , $P_1 = 1$ bar air. Valve is at the left side (not shown in the photograph)

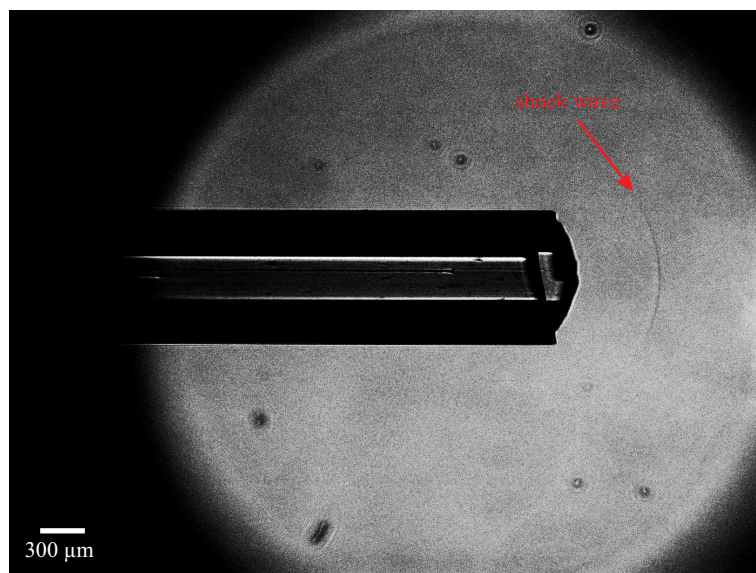


Figure 5.27: Schlieren image of a shock wave shortly after exiting a $300 \mu\text{m}$ capillary; $P_4 = 20$ bar N_2 , $P_1 = 1$ bar air.

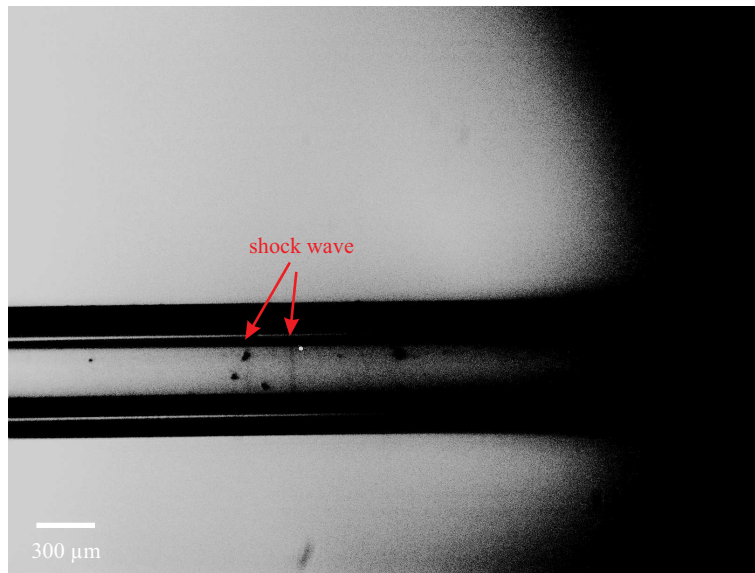


Figure 5.28: Schlieren image of a shock wave at the exit of a $300\ \mu\text{m}$ capillary; double exposures with time difference of $500\ \text{ns}$; $P_4 = 20\ \text{bar N}_2$, $P_1 = 1\ \text{bar air}$.

	LDI	Schlieren
$t\ [\mu\text{s}]$ near the capillary exit	539 ± 2	537 ± 2
$t\ [\mu\text{s}]$ outside the capillary exit	549 ± 2	547 ± 2

Table 5.3: Shock wave arrival time t determined using the Schlieren optics and the LDI for the same positions. Each measurement is reproduced 10 times. $P_4 = 20\ \text{bar N}_2$, $P_1 = 1\ \text{bar air}$.

Fig. 5.26 shows an important qualitative result: the magnetic valve generated shock wave inside capillary seems to be ‘thicker’ than outside (Fig. 5.27). But this is just illusion due to the photograph. Fig. 5.26 is actually a proof that the shock wave has higher curvature inside the capillary than outside. Because when the shock wave is highly curved, it may have thicker projection as sketched in Fig. 5.29. The real thickness of the shock wave inside the capillary is, however, smaller than outside. The shock wave attenuates along its propagation, thus it is faster in the earlier propagation phase inside the capillary. Furthermore, higher shock velocity corresponds to thinner shock thickness [82]. As a comment, the shock thickness is approximately $150\ \text{nm}$ [82] for a shock wave with Mach 2 in ambient air.

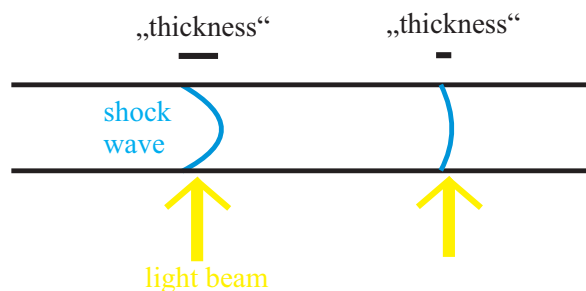


Figure 5.29: Illustration of the shine ‘thickness’ due to shock front curvature.

The correlation between the shock front's curvature and wall friction is already investigated in the work of De Boer [71]. According to [71], the high curvature shown here suggests high wall friction. The Schlieren photos thus also confirms our expectation from the very beginning of the thesis that the shock wave in a micro capillary experiences significantly wall friction.

From the technical perspective, Tab. 5.3 confirms that the LDI and the Schlieren measurements of shock trajectory (namely t) are in agreement. Note that the Schlieren measurement of t is just a small control, which is not supposed to be a complete experiment replacing the LDI measurements.

Chapter 6

Summary and outlook

The key issue of the thesis is the micro shock waves. The clear takeaway is that micro shock wave is different than macro shock wave, which is due to diffusive transport phenomena caused by the wall friction and heat conduction.

This thesis can be summarized as:

1. The novel method Laser-plasma Induced Micro Shocks (LIMS) is introduced. LIMS bases on the generation of a laser plasma on a thin metal film at the rear side of a transparent plate. The plasma further drives a shock wave in an ambient fluid. The shock wave propagates further in a capillary with a diameter in the range of dozens of μm . This novel method provides the possibility for shock wave (direct) generation at micro scale, which is nearly impossible for conventional techniques. LIMS has even the potential to be extended to (a few hundreds) nanometer scale.

Shock wave propagation in quasi point-like and quasi planar geometry are tested. As expected, the quasi planar geometry is the most suitable, i.e. propagates the longest distance. In the confined environment of the capillary, propagation length up to several mm becomes available, before the shock wave converts to a compression wave with sound velocity. Experimental results have been supported by hydrocode (MULTIFs) simulation and Navier-Stokes computation from cooperation partners (co-authors of our papers). The Navier-Stokes computation shows that the attenuation of LIMS is mainly caused by the expansion fan, which has also been observed in our experiments. The boundary layer development due to viscous effects further contributes to the shock attenuation.

For the hydraulic diameter of $D \geq 200 \mu\text{m}$, the (ideal) Rankine-Hugoniot relation is proved to be valid by experiments. But for $D < 200 \mu\text{m}$, specially at $D = 50 \mu\text{m}$, the Rankine-Hugoniot relation begins to show slightly noticeable difference with the experimental results. In this thesis, a preliminary version of the corrected Rankine-Hugoniot relation is proposed. The plausibility of the corrected RH relation is checked by Matlab simulation. The corrected RH also agree with the experimental results roughly better than the ideal RH.

2. The novel method involving a high-speed magnetic valve is introduced. Micro shock flow as a whole is investigated for the first time at micro scale (especially the contact surface). This is an essential result because it gives access to the shock-contact distance L enclosed in the scaling factor Sc [9], which is meanwhile well-established but never used correctly. The dimensionless analysis of micro shock using Sc can now be applied correctly, finally. Furthermore, the experimental results confront the existing theories in [22, 34, 35, 78]. Here it is found that the famous ‘leaky piston’ model (for conventional shock tubes) doesn’t apply for micro shock flows anymore. The problems of the model are identified as: A. thin boundary layer assumption B. the assumption of equal velocity for the post-shock particles and the contact surface.

To the best of my knowledge, the current work is one of the very few investigations on the micro shock wave, which is a new area of research since the 21st century. The results and some of the methodologies are unique. This thesis opens up new perspectives in studying micro shock flows, and shall encourage further developments of theoretical models and experiments. The findings here can also be important for industrial applications and medical technologies, where smaller scaled shock waves are used but never truly understood. In the field of compressible fluid mechanics, it is also true that ‘there is plenty of room at the bottom’ [83].

Appendix A

Additional results on mini shock-cavitation interaction

The results of this chapter are mainly published in [84]. This chapter is put into the appendix, because the plasma shock generation in liquid shows complicated flow patterns which may add too many parameters to the essential development of LIMS method.

The previous chapters of this thesis have presented the mini and micro shock waves in air. One can further ask that, what about the mini and micro shock waves in water? Are they different from macroscopic shock waves in water? The chapter tries to take a look at these questions. Furthermore, since approximately 70% of the human body is water, shock wave research in water can be related to medical application (e.g. lithotripsy).

This chapter presents the first experimental results of the onset of evaporation in a mini-shock tube. Different sizes of shock tubes lead to different interactions (in time and in strength) between the shock wave and the cavitation bubble. As a result, the onset of evaporation occurs differently.

It needs to be pointed out that, instead of a fs-laser as in the previous chapter, a ns-laser is applied. There are two reasons: firstly, higher energy is needed to generate a bigger plasma in mini meter scales. Secondly, the setup is rearranged based on an older setup for cavitation bubbles experiments, where the ns-laser was already fixed in the setup. It is certainly interesting to apply the fs-laser as well for these experiments. In the outlook, it will be discussed.

Spherical shock waves generated in water-filled glass tubes via laser-induced breakdown are investigated experimentally. The emitted shock wave is consecutively followed by the onset of a spherical cavitation bubble, which expands at a much smaller velocity. The transient shock wave is reflected at the inner wall of the glass tube and moves towards to the tube axis, where the collision of the reflected shock waves happens. In addition, interactions with reflected shock and rarefaction waves play an important

role with respect to the formation of a growing number of small vapor bubbles. In the 1960s Askar'yan [85] published one of the earliest articles that cover the aspect of focused laser light in liquids. Later in the 1970s and 1980s, Lauternborn [86], [87] emphasized the study of cavitation bubble dynamics and shock wave generation through laser-induced breakdown. Teslenko [88] investigated the shock wave pressure and bubble radius depending on laser pulse energy and duration. In the subsequent years till nowadays, a wealth of investigations and applications of laser-induced shock waves are emerging and expanding, especially in the medical fields e.g. ocular surgery and lithotripsy [89]. This work further contributes to the laser-induced shock waves in liquid and presents the first experiments of the onset of evaporation in a miniature shock tube.

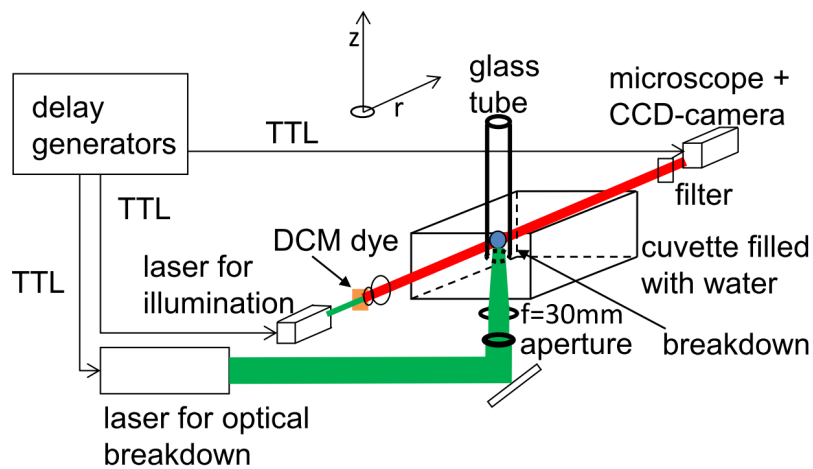


Figure A.1: Experimental setup to generate and investigate shock waves in a mini-shock tube.

The setup is to be seen in Figure A.1. An optical breakdown induced by a frequency doubled and Q-switched Nd:YAG laser (pulse duration 6 ns, pulse energy 5.6 mJ, model *Surelite I*, *Continuum*) generates shock waves in spherical geometry in water. By applying again the double-cavity Nd:YAG laser (pulse duration 6 ns, pulse energy 25 mJ, model *Solo III 15*, *New Wave*), the shock velocity is determined (explained in section 3.2). In the present work, the optical breakdown occurs in water in a glass tube (a larger tube with inner diameter $d_{in} = 6$ mm, a smaller tube with $d_{in} = 1.7$ mm), which is placed in a glass cuvette filled with water. External pressure of several mbar via a water tank pressure reservoir is applied into the tube to control the position of the water surface. The propagation and reflection of the shock waves as well as the evaporation process is investigated.

Figure A.2 shows the position of the optical breakdown (a), the initial spherical shock wave 200 ns later (b) and 900 ns later (c), respectively. Figure A.2(d) shows the maximum enlargement of the cavitation bubble. A similar process is seen when the breakdown occurs in a water-filled cuvette instead of a tube. From onset to bubble

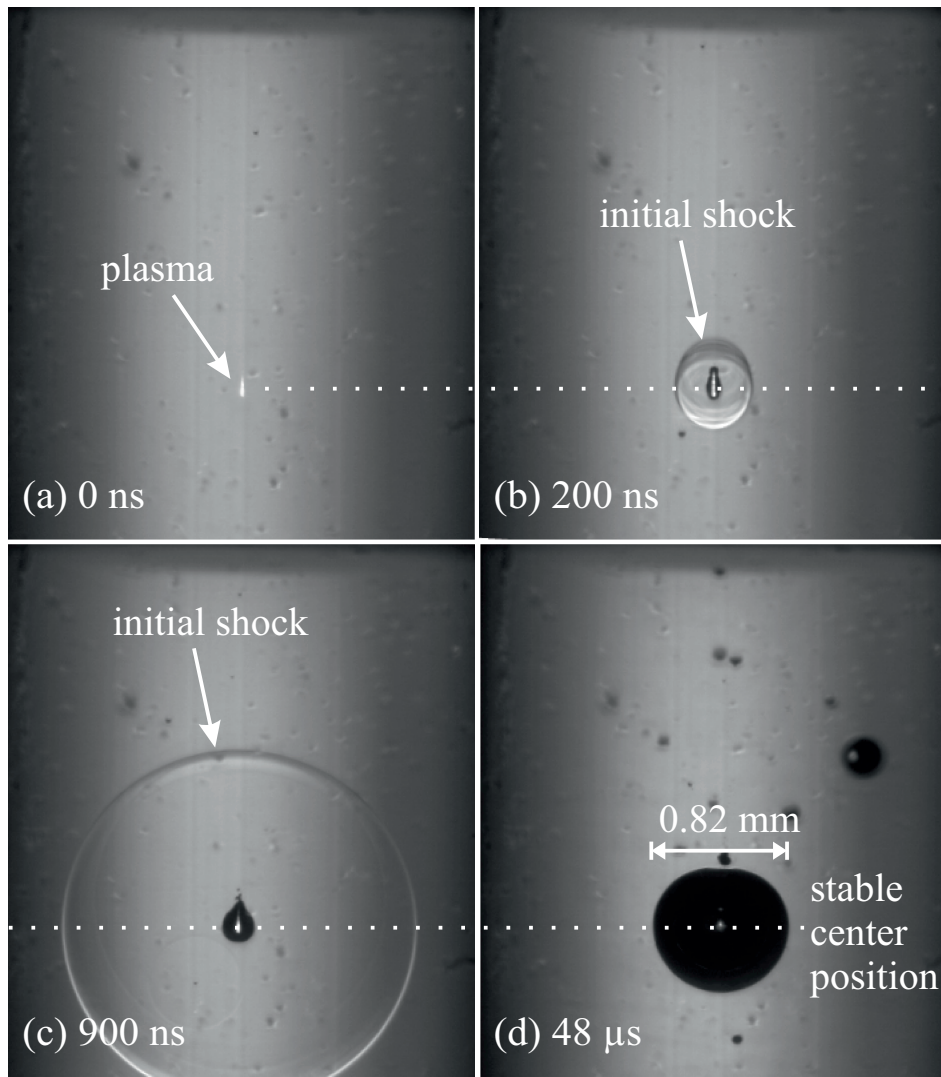


Figure A.2: Laser-induced breakdown with subsequent shock wave and cavitation bubble formation in a water-filled glass tube with $d_{in} = 6$ mm. The scale indicated in (d) applies for all photos.

maximum, neither the tube wall nor the water surface take influence on the bubble dynamics in this case. Since the maximum bubble diameter is smaller than the tube inner diameter and the distance to water surface. The original images of the experiment are recorded with an inter frame time of $t = 100$ ns and an exposure time of $t_{exp} = 6$ ns.

Figure A.3 presents a selected part of a series of images which has an inter frame time of 100 ns and an exposure time of 6 ns. In Figure A.3(a), it can be seen that the shock waves are reflected from the inner wall and move towards the bubble. In Figure A.3(b) it is noticed that the reflected shock waves hit the bubble first, and consecutively do come into contact with each other in the middle, which leads to complicated wave structures. After reflection of the colliding shock waves, first vapor bubbles become visible in Figure A.3(c), then increase in number and diameter in Figure A.3(d)-(h).

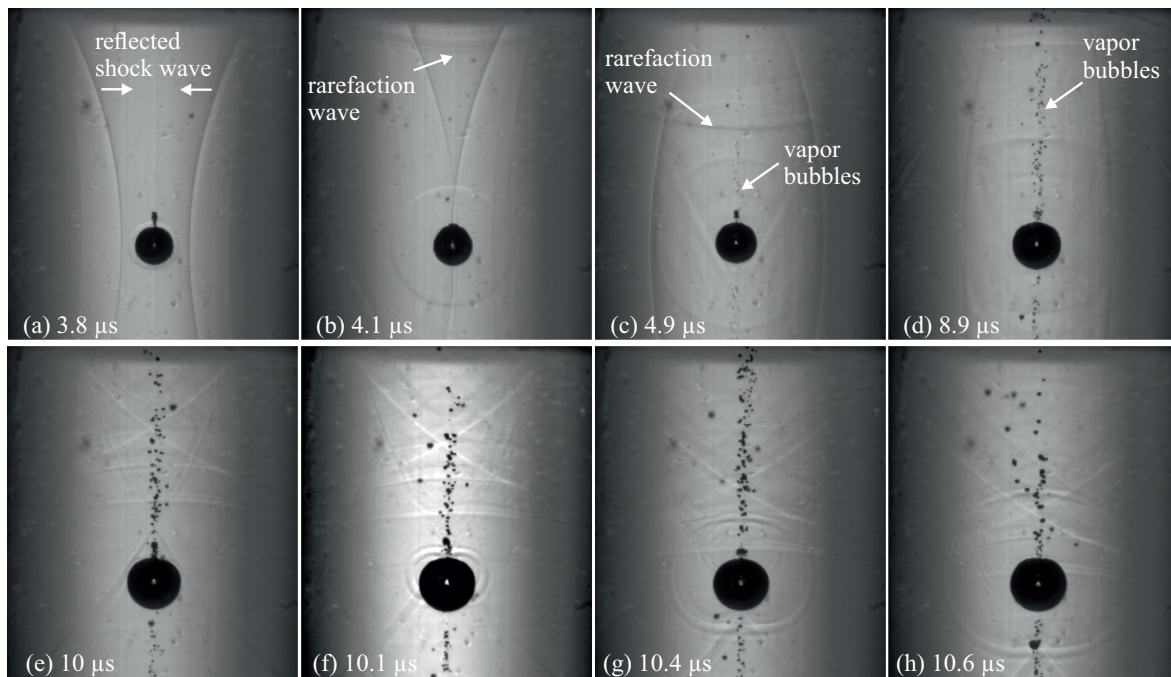


Figure A.3: Evolution of the shock wave, vapor bubbles and shock-bubble interactions in a glass tube with $d_{in} = 6$ mm.

However, in spite of these results, it is not yet clear whether the vapor bubbles emerge from the leakage of the cavitation bubble or from the evaporation in the liquid (due to the pressure reduction on the vertical axis). Therefore, further detailed investigations by the utilization of a high speed camera will be of great interest.

Figure A.4(a) shows the minimum cavitation bubble during the collapse. In Figure A.4(b) the bubble collapses accompanied by the emission of two spherical shock waves. Figure A.4(c) and (d) show that those bubbles rebound. In case that the following conditions are fulfilled, the temporal and spatial development of the cavitation bubble from its onset to its collapse in the glass tube is not much different from the results which are acquired in a cuvette: this is namely the case if the inner diameter is large enough, e.g. several times larger than the maximum cavitation bubble diameter d_{max} (in this work, approximately 8 times d_{max}); the distance between the breakdown and the water-air boundary is also large enough (in this work, distance 8 mm, i.e. approximately 10 times d_{max}).

The emitted shock wave after the collapse repeats the process described above, so that the processes of bubble formation are observed in every life circle of the bubble.

Laser-induced breakdown is also generated in smaller glass tubes with a inner diameter $d_{in} = 1.7$ mm. Similar to the larger tube with $d_{in} = 6$ mm, Figure A.5(a) shows the development of the shock waves and the rarefaction waves as well as their interaction with the cavitation bubble in the smaller tube.

In Figure A.5(a), it can also be seen that the initial shock waves are reflected from

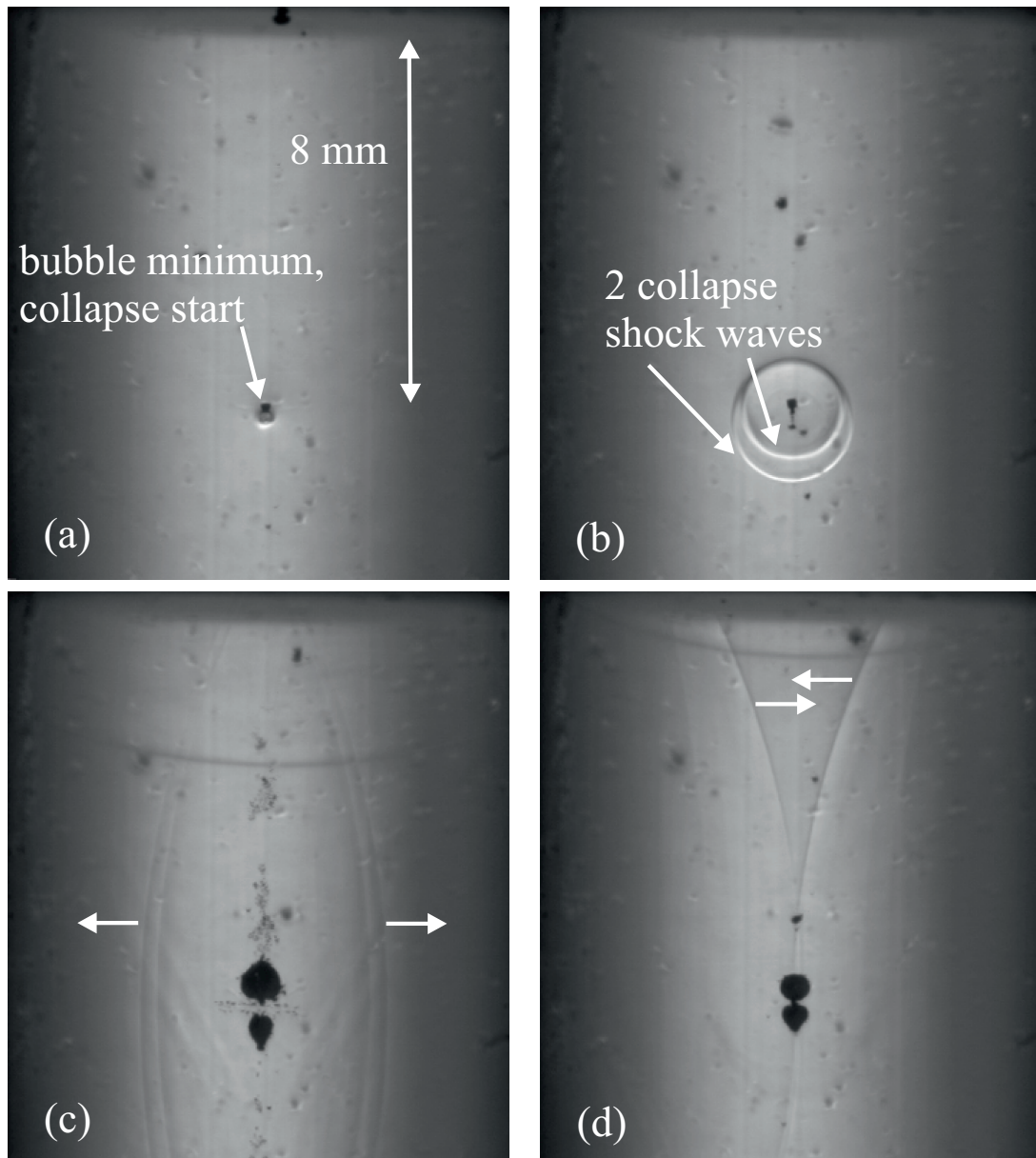


Figure A.4: Bubble collapse and emission of collapse shock waves in a glass tube with $d_{in} = 6$ mm; inter frames time is about 100 ns

the inner wall of the glass tube, right before reaching the cavitation bubble. Figure A.5(b) shows the formation of the rarefaction wave which has a shape with a spherical contour around the bubble. In Figure A.5(c), merely 290 ns after the laser-induced breakdown, the first vapor bubbles can be seen (compare to 4.9 μ s by the larger tube, see Figure A.3(c)). After 290 ns, the initially emitted spherical shock wave, which moves in the axial direction, is reflected at the water-air boundary and then continues to propagate as a rarefaction wave that causes a spontaneous evaporation in the area above the cavitation bubble. This phenomenon is clearly visible in Figure A.5(d) at the upper half of the image. Moreover, the amount and size of the vapor bubbles at the lower half of the image increase as well. This can be explained by the fact that the

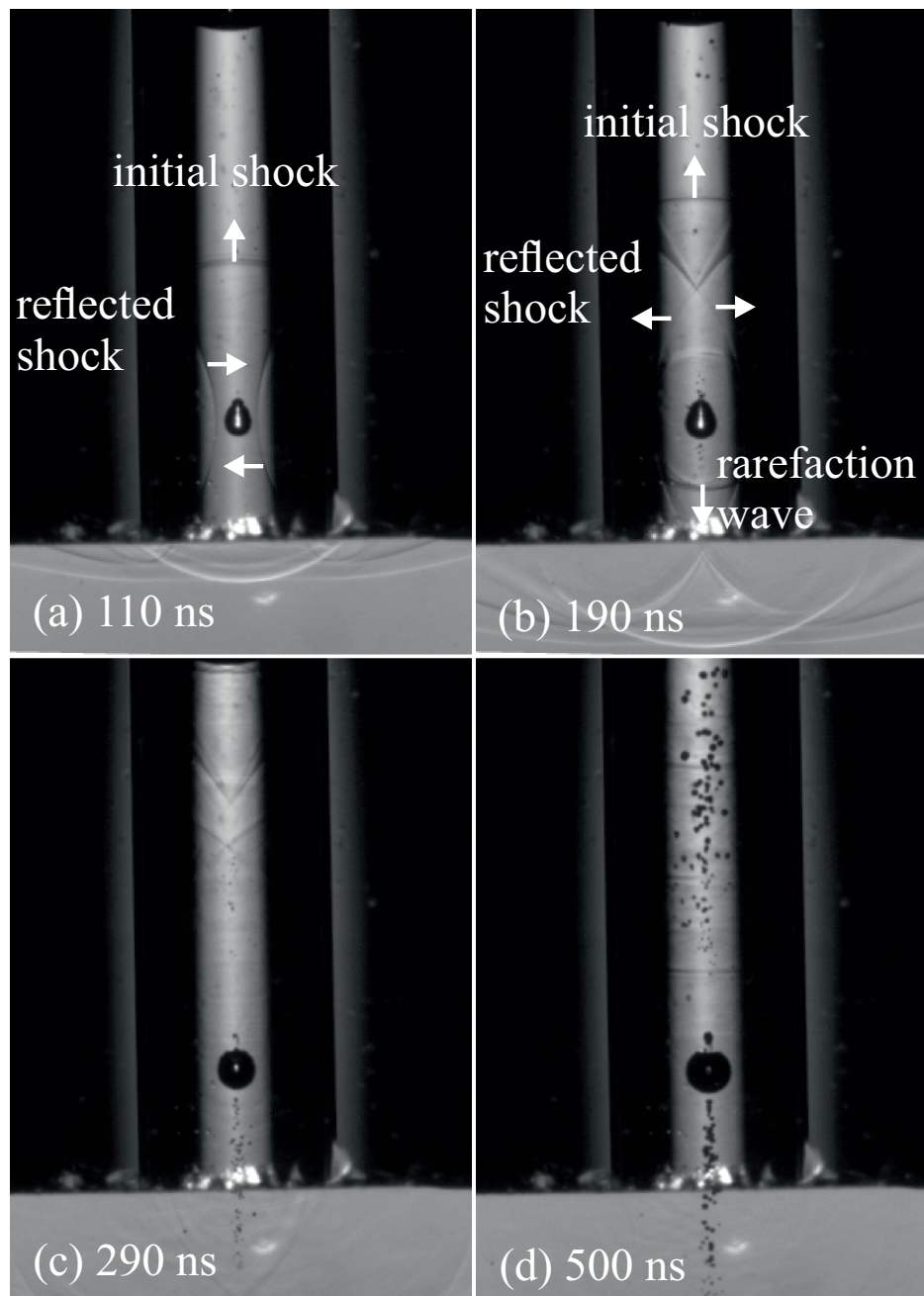


Figure A.5: Shock and rarefaction wave development and the onset of vapor bubbles, respectively, in a water-filled glass tube with $d_{in} = 1.7$ mm.

initial shock wave propagating in the axial downwards direction is also reflected as a rarefaction wave upon exiting the tube, subsequently it propagates back into the glass tube.

Since the tube has a smaller inner diameter now, the initial shock wave is reflected after a shorter propagating time, thus the reflected shock wave is stronger and the interactions are more intense. Secondly, the cavitation bubble is at an earlier developing phase, when the reflected shock wave interacts with the bubble. Different developing phase of the bubble corresponds to different pressure, temperature and density. Fig.

A.6 indicates the time points of the evaporation onset.

Thus, the evaporation is influenced by the bubble dynamics as well as the strength of the reflected shock waves, which are again affected by the dimensional restriction given by the shock tube.

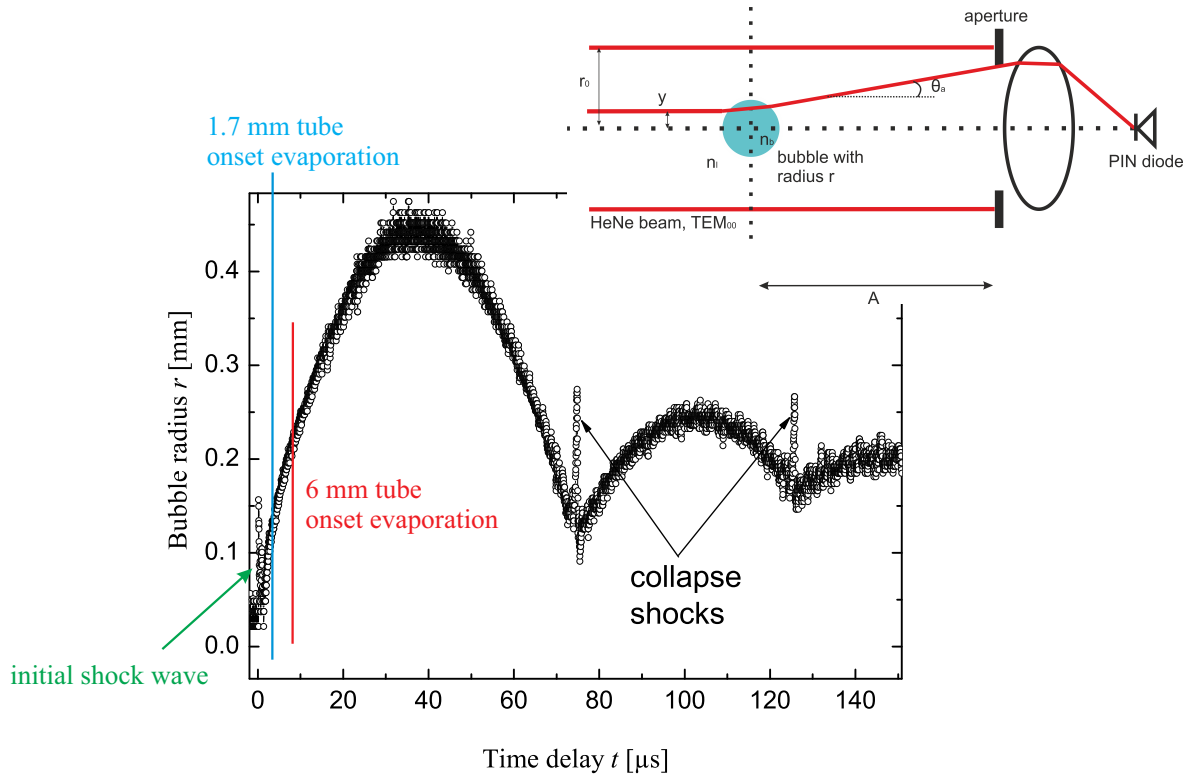


Figure A.6: Shock wave induced evaporation in the time line of the cavitation bubble development. Bubble measured by Laser Shadow Method (LSM) [90].

Laser-induced shock waves in a glass tube filled with water lead to an intense vapor bubble formation in its growth phase. The process essentially depends on the tube diameter and on the position of the optical breakdown relative to the water-air boundary. Vapor bubble formation, or say, evaporation occurs earlier in a smaller tube when compared to larger tubes. This can be a result of the more strongly reflected shock waves. The cavitation bubble collapses for the first time after approximately 140-150 μs , which generally agrees with the results published earlier from our group [90]. The question whether the cavitation bubble produces the vapor bubbles due to the interaction with the reflected shock waves from the tube wall, or due to the rarefaction wave reflected from the water-air boundary is still open. It is also conceivable that the highly curved spherical shock waves lead to pressure reduction and evaporation.

As for the outlook, a fs-laser as in the previous chapters shall be applied for these experiments, so that more comparable experiments can be made. Furthermore, it is very interesting to use even smaller shock tubes for stronger shock-bubble interactions. When it goes down to micro scales, heat conduction (scales with $1/D^2$, D is diameter)

effects play a bigger role, which can eventually further affect the evaporation.

For an extreme case that the shock tube is as small as the plasma, the initial shock wave will be almost immediately reflected from the tube wall after it starts to propagate. The cavitation bubble is however in a very early phase or not even formed, when the shock-bubble interactions occurs. What evaporation process will happen then in the micro shock tubes?

A recent paper of our group [91] has shown that, in case the water temperature is above 75 °C, shock wave is not emitted during the collapse phase of the cavitation bubble. It indicates that, the shock wave related bubble properties strongly depends on the temperature and viscosity.

So, what will happen if we repeat the mini shock wave experiments simply in water of higher temperature? Or in glycerine with higher viscosity. Will the shock induced evaporation process also be affected by different bubble properties?

For the future work, these aforementioned aspects shall be investigated.

Bibliography

- [1] T Tamba, TM Nguyen, K Takeya, T Harasaki, A Iwakawa, and A Sasoh. Counter-driver shock tube. *Shock Waves*, 25(6):667–674, 2015.
- [2] A Russell, H Zare-Behtash, and K Kontis. Joule heating flow control methods for high-speed flows. *Journal of Electrostatics*, 80:34–68, 2016.
- [3] P Moore and GE Hunt. Atlas of the solar system. *Chicago: Rand McNally, 1983.*, 1983.
- [4] AH Sulaiman, A Masters, MK Dougherty, D Burgess, M Fujimoto, and GB Hospodarsky. Quasiperpendicular high mach number shocks. *Physical review letters*, 115(12):125001, 2015.
- [5] A Wagner, M Schramm, JP Hickey, and K Hannemann. Hypersonic shock wave boundary layer interaction studies on a flat plate at elevated surface temperature. *Proc. ISIS21 Glasgow*, 2016.
- [6] EG Gamaly, L Rapp, V Roppo, S Juodkazis, and AV Rode. Generation of high energy density by fs-laser-induced confined microexplosion. *New Journal of Physics*, 15(2):025018, 2013.
- [7] J Lindl. Development of the indirect-drive approach to inertial confinement fusion and the target physics basis for ignition and gain. *Physics of plasmas*, 2(11):3933–4024, 1995.
- [8] M Sun, T Ogawa, and K Takayama. Shock propagation in narrow channels. *ISSW23, Fort Worth, TX*, 2001.
- [9] M Brouillette. Shock waves at microscales. *Shock waves*, 13(1):3–12, 2003.
- [10] G Mirshekari and M Brouillette. One-dimensional model for microscale shock tube flow. *Shock Waves*, 19(1):25–38, 2009.
- [11] G Mirshekari and M Brouillette. Microscale shock tube. *Journal of Microelectromechanical Systems*, 21(3):739–748, 2012.

- [12] G Mirshekari, Martin Brouillette, Jerome Giordano, C Hébert, J-D Parisse, and Pierre Perrier. Shock waves in microchannels. *Journal of Fluid Mechanics*, 724: 259–283, 2013.
- [13] DE Zeitoun and Y Burtschell. Navier–stokes computations in micro shock tubes. *Shock Waves*, 15(3-4):241–246, 2006.
- [14] DE Zeitoun. Correlations of shock mach number attenuation in small size diameter tubes. *Physics of Fluids*, 27(1):011701, 2015.
- [15] JM Austin and DJ Bodony. Wave propagation in gaseous small-scale channel flows. *Shock Waves*, 21(6):547, 2011.
- [16] A Deshpande and B Puranik. A numerical investigation of shock propagation in three-dimensional microducts. *Shock Waves*, 27(4):565–582, 2017.
- [17] U Teubner, Y Kai, T Schlegel, DE Zeitoun, and W Garen. Laser-plasma induced shock waves in micro shock tubes. *New Journal of Physics*, 19(10):103016, 2017.
- [18] KPJ Reddy and N Sharath. The motion of a 2 mm tantalum block induced by underwater explosion. *Current Science*, 104(2):172–176, 2013.
- [19] G Jagadeesh, GD Prakash, SG Rakesh, US Allam, MG Krishna, SM Eswarappa, and D Chakravorty. Needleless vaccine delivery using micro-shock waves. *Clinical and Vaccine Immunology*, 18(4):539–545, 2011.
- [20] T Koita, T Gonai, M Sun, S Owada, and T Nakamura. Manually operated piston-driven shock tube. *Proc. ISSW30 Tel Aviv*, 2015.
- [21] G Vézina, H Fortier-Topping, F Bolduc-Teasdale, D Rancourt, M Picard, JB Plante, M Brouillette, and L Fréchette. Design and experimental validation of a supersonic concentric micro gas turbine. *Journal of Turbomachinery*, 138(2): 021007, 2016.
- [22] RE Duff. Shock-tube performance at low initial pressure. *Physics of Fluids (1958-1988)*, 2(2):207–216, 1959.
- [23] SG Jennings. The mean free path in air. *Journal of Aerosol Science*, 19(2):159–166, 1988.
- [24] A Deshpande and B Puranik. Effect of viscosity and wall heat conduction on shock attenuation in narrow channels. *Shock Waves*, 26(4):465–475, 2016.
- [25] Joseph Needham, Ling Wang, and Gwei Djen Lu. *Science and civilisation in China*, volume 5. Cambridge University Press Cambridge, 1963.

- [26] H Reichenbach. In the footsteps of ernst mach—a historical review of shock wave research at the ernst-mach-institut. *Shock waves*, 2(2):65–79, 1992.
- [27] B Riemann. *Über die Fortpflanzung ebener Luftwellen von endlicher Schwingungsweite*. Verlag der Dieterichschen Buchhandlung, 1860.
- [28] WJ Macquorn Rankine. On the thermodynamic theory of waves of finite longitudinal disturbance. *Philosophical Transactions of the Royal Society of London*, pages 277–288, 1870.
- [29] PH Hugoniot. *Mémoire sur la propagation du mouvement dans un fluide indéfini: Sur la propagation du mouvement dans les corps et spécialement dans les gaz parfaits*. Impr. nationale, 1950.
- [30] E Mach and P Salcher. Photographische fixirung der durch projectile in der luft eingeleiteten vorgänge. *Annalen der Physik*, 268(10):277–291, 1887.
- [31] P Vieille. Sur les discontinuités produites par la détente brusque de gaz comprimés. *Comptes Rendus*, 129:1228–1230, 1899.
- [32] JD Anderson. *Modern compressible flow: with historical perspective*, volume 12. McGraw-Hill New York, 2003.
- [33] YB Zel'dovich and YP Raizer. *Physics of shock waves and high-temperature hydrodynamic phenomena*. Courier Corporation, 2002.
- [34] A Roshko. On flow duration in low-pressure shock tubes. *The Physics of Fluids*, 3(6):835–842, 1960.
- [35] H Mirels. Test time in low-pressure shock tubes. *The physics of Fluids*, 6(9):1201–1214, 1963.
- [36] H Mirels. Correlation formulas for laminar shock tube boundary layer. *Physics of Fluids (1958-1988)*, 9(7):1265–1272, 1966.
- [37] W Garen, R Synofzik, and A Frohn. Shock tube for generating weak shock waves. *AIAA Journal*, 12(8):1132–1134, 1974.
- [38] D Zeitoun and M Imbert. Interaction between the unsteady boundary layer and inviscid hot flow in a shock tube. *AIAA Journal*, 17(8):821–827, 1979.
- [39] W Garen, T Buss, S Foschepoth, M Becker, S Koch, and E Novoselova. A novel mini-shock tube for generating shock waves at micro scales in turbulent and laminar gas flows. In *Proceedings of 25th International Symposium on Shock Waves*, pages 746–750, 2005.

- [40] W Garen, B Meyerer, S Udagawa, and K Maeno. Shock waves in mini-tubes: influence of the scaling parameter s . *Shock Waves*, pages 1473–1478, 2009.
- [41] D Ngomo, A Chaudhuri, A Chinnayya, and A Hadjadj. Numerical study of shock propagation and attenuation in narrow tubes including friction and heat losses. *Computers & Fluids*, 39(9):1711–1721, 2010.
- [42] D Mee. *Lecture notes in Hypersonics - from Shock Waves to Scramjets*. University of Queensland, 2016.
- [43] PA Tipler and G Mosca. Physik für wissenschaftler und ingenieure, 6. *Auflage*, Heidelberg, 2009.
- [44] M Juniper. *Lecture notes of fluid mechanics*. University of Cambridge, 2017.
- [45] George Keith Batchelor. *An introduction to fluid dynamics*. Cambridge university press, 2000.
- [46] R Rangel. Engineering mae 130a. introduction to fluid mechanics. *open course*, University of California, Irvine, 2014.
- [47] Mohamed Gad-el Hak. Flow physics in mems. *Mécanique & industries*, 2(4): 313–341, 2001.
- [48] Martin Knudsen. Die gesetze der molekularströmung und der inneren reibungsströmung der gase durch röhren. *Annalen der Physik*, 333(1):75–130, 1909.
- [49] HJ Eichler and J Eichler. *Laser: Bauformen, Strahlführung, Anwendungen*. Springer-Verlag, 2006.
- [50] E Hecht. *Optik*, 4., überarbeitete auflage, 2005.
- [51] S Martin. *Zerstörmechanismen in optischen Materialien bei Anregung mit ultrakurzen Laserpulsen*. PhD thesis, Freie Universität Berlin, 2005.
- [52] G Smeets. Laser interferometer for transient phase objects. In *Proc. of the eighth International Shock Tube Symposium*, 1971.
- [53] Y Kai, W Garen, and U Teubner. Generation and propagation of shock waves in sub-millimeter capillaries. *Proc. ISSW30 Tel Aviv*, 2015.
- [54] S Udagawa, K Maeno, I Golubeva, and W Garen. Interferometric signal measurement of shock waves and contact surfaces in small scale shock tube. pages 1419–1424, 2009.

- [55] S Udagawa, W Garen, B Meyerer, and K Maeno. Interferometric detection of dispersed shock waves in small scale diaphragm-less shock tube of 1mm diameter. In *16th Australasian Fluid Mechanics Conference (AFMC)*, pages 207–210. School of Engineering, The University of Queensland, 2007.
- [56] H Oertel. *Optische Strömungsmeßtechnik*. G. Braun Karlsruhe, 1989.
- [57] Philip E Ciddor. Refractive index of air: new equations for the visible and near infrared. *Applied optics*, 35(9):1566–1573, 1996.
- [58] Charles R Mansfield and Edson R Peck. Dispersion of helium. *JOSA*, 59(2):199–204, 1969.
- [59] Y Kai, W Garen, T Schlegel, and U Teubner. A novel shock tube with a laser–plasma driver. *Laser and Particle Beams*, 35(4):610–618, 2017.
- [60] A Caruso and R Gratton. Interaction of short laser pulses with solid materials. *Plasma Physics*, 11(10):839, 1969.
- [61] U Teubner, C Wülker, W Theobald, and E Förster. X-ray spectra from high-intensity subpicosecond laser produced plasmas. *Physics of Plasmas*, 2(3):972–981, 1995.
- [62] ED Palik. *Handbook of optical constants of solids*, volume 3. Academic press, 1998.
- [63] D Meschede. *Gerthsen Physik*. Springer-Verlag, 2015.
- [64] R Ramis, K Eidmann, J Meyer-ter Vehn, and S Hüller. Multi-fs—a computer code for laser–plasma interaction in the femtosecond regime. *Computer Physics Communications*, 183(3):637–655, 2012.
- [65] S Faik, MM Basko, A Tauschwitz, I Iosilevskiy, and JA Maruhn. Dynamics of volumetrically heated matter passing through the liquid–vapor metastable states. *High Energy Density Physics*, 8(4):349–359, 2012.
- [66] AJ Kemp and J Meyer-ter Vehn. An equation of state code for hot dense matter, based on the qeos description. *Nuclear Instruments and Methods in Physics Research Section A: Accelerators, Spectrometers, Detectors and Associated Equipment*, 415(3):674–676, 1998.
- [67] DA Young and EM Corey. A new global equation of state model for hot, dense matter. *Journal of applied physics*, 78(6):3748–3755, 1995.

- [68] SP Lyon and JD Johnson. Los alamos national laboratory report no. la-ur-3407. Technical report, Los Alamos National Laboratory, 1992.
- [69] T4 GROUP et al. Sesame report on the los alamos equationof-state library. Technical report, Report No. LALP-83-4. Los Alamos, NM: Los Alamos National Laboratory, 1983.
- [70] K Eidmann. Radiation transport and atomic physics modeling in high-energy-density laser-produced plasmas. *Laser and particle beams*, 12(02):223–244, 1994.
- [71] P Cornelis T De Boer. Curvature of shock fronts in shock tubes. *The Physics of Fluids*, 6(7):962–971, 1963.
- [72] LI Sedov. *Similarity and dimensional methods in mechanics*. CRC press, 1993.
- [73] www.engineeringtoolbox.com. online data bank. 2016.
- [74] H Schlichting and K Gersten. *Boundary-layer theory*. Springer Science & Business Media, 2003.
- [75] Y Burtschell, M Cardoso, and DE Zeitoun. Numerical analysis of reducing driver gas contamination in impulse shock tunnels. *AIAA journal*, 39(12):2357–2365, 2001.
- [76] GG Chernyi. The problem of a point explosion. In *Dokl. Akad. Nauk SSSR*, volume 112, pages 213–216, 1957.
- [77] Yun Kai, Walter Garen, and Ulrich Teubner. Experimental investigations on microshock waves and contact surfaces. *Physical review letters*, 120(6):064501, 2018.
- [78] WJ Hooker. Testing time and contact-zone phenomena in shock-tube flows. *The Physics of Fluids*, 4(12):1451–1463, 1961.
- [79] E Hering, R Martin, and M Stohrer. *Physik fuer Ingenieure*. Springer-Verlag, 2007.
- [80] HANS Hornung, B Sturtevant, J Belanger, S Sanderson, M Brouillette, and M Jenkins. Performance data of the new free-piston shock tunnel t5 at galcit. In *Shock Waves*, pages 603–610. Springer, 1992.
- [81] WH Beck, G Eitelberg, TJ McIntyre, JP Baird, J Lacey, and H Simon. The high enthalpy shock tunnel in göttingen (heg). In *Shock Waves*, pages 677–682. Springer, 1992.
- [82] PA Thompson. *Compressible-fluid dynamic*. McGraw-Hill, 1971.

- [83] Richard P Feynman. There's plenty of room at the bottom. *Miniaturization*, pages 282–296, 1959.
- [84] Y Kai, B Meyerer, W Garen, and U Teubner. Experimental investigation of laser generated shock waves and the onset of evaporation in a mini-shock glass tube filled with water. *Proc. ISIS20 Riga*, 2014.
- [85] GA Askar'yan, AM Prokhorov, GF Chanturiya, and GP Shipulo. The effects of a laser beam in a liquid. *Sov. Phys. JETP*, 17(6):1463–1465, 1963.
- [86] W Lauterborn. High-speed photography of laser-induced breakdown in liquids. *Applied Physics Letters*, 21(1):27–29, 1972.
- [87] W Lauterborn. *Kavitation durch laserlicht*. PhD thesis, 1974.
- [88] VS Teslenko. Investigation of photoacoustic and photohydrodynamic parameters of laser breakdown in liquids. *Soviet Journal of Quantum Electronics*, 7(8):981, 1977.
- [89] A Vogel, W Hentschel, J Holzfuss, and W Lauterborn. Cavitation bubble dynamics and acoustic transient generation in ocular surgery with pulsed neodymium: Yag lasers. *Ophthalmology*, 93(10):1259–1269, 1986.
- [90] W Garen, F Hegedűs, S Koch, B Meyerer, W Neu, and U Teubner. Experimental investigation of laser-induced cavitation bubbles dynamics. *GALA 2013 conference proceeding*, (67), 2013.
- [91] W Garen, F Hegedűs, Y Kai, S Koch, B Meyerer, W Neu, and U Teubner. Shock wave emission during the collapse of cavitation bubbles. *Shock Waves*, pages 1–10, 2016.